DISSERTATIONES
CHIMICAE
UNIVERSITATIS
TARTUENSIS
221

JONAS MART LINGE

Electrochemical reduction of oxygen on silver-based catalysts

DISSERTATIONES CHIMICAE UNIVERSITATIS TARTUENSIS
221

DISSERTATIONES CHIMICAE UNIVERSITATIS TARTUENSIS
221

JONAS MART LINGE

Electrochemical reduction of oxygen on silver-based catalysts

UNIVERSITY OF TARTU
Press
1632

Institute of Chemistry, Faculty of Science and Technology, University of Tartu, Estonia

The dissertation is accepted for the commencement of the degree of *Doctor Philosophiae* in Chemistry on June 22, 2023 by the Council of Institute of Chemistry, Faculty of Science and Technology, University of Tartu.

Supervisors: Prof. Kaido Tammeveski
Institute of Chemistry, University of Tartu, Estonia

PhD Heiki Erikson
Institute of Chemistry, University of Tartu, Estonia

Opponent: PhD Nejc Hodnik
Department of Materials Chemistry,
National Institute of Chemistry, Ljubljana, Slovenia

Commencement: August 25th, 2023 at 12.15 Ravila 14A–1020, Tartu (Chemicum) and Microsoft Teams (*online*)

This work has been partially supported by ASTRA project PER ASPERA Graduate School of Functional Materials and Technologies receiving funding from the European Regional Development Fund under project in University of Tartu, Estonia

ISSN 1406-0299 (print)
ISBN 978-9916-27-280-0 (print)
ISSN 2806-2159 (pdf)
ISBN 978-9916-27-281-7 (pdf)

University of Tartu Press
www.tyk.ee

TABLE OF CONTENTS

1. LIST OF ORIGINAL PUBLICATIONS

I **J.M. Linge**, H. Erikson, J. Kozlova, J. Aruväli, V. Sammelselg, K. Tammeveski, Oxygen reduction on electrodeposited silver catalysts in alkaline solution, *Journal of Solid State Electrochemistry* 22 (2018) 81–89.

II **J.M. Linge**, H. Erikson, J. Kozlova, V. Sammelselg, K. Tammeveski, Oxygen reduction reaction on electrochemically deposited silver nanoparticles from non-aqueous solution, *Journal of Electroanalytical Chemistry* 810 (2018) 129–134.

III **J.M. Linge**, H. Erikson, M. Merisalu, V. Sammelselg, K. Tammeveski, Oxygen reduction on silver catalysts electrodeposited on various nanocarbon supports, *SN Applied Sciences* 3(2) (2021) 263.

IV **J.M. Linge**, H. Erikson, M. Merisalu, L. Matisen, M. Käärik, J. Leis, V. Sammelselg, J. Aruväli, T. Kaljuvee, K. Tammeveski, Oxygen reduction on silver nanoparticles supported on carbide-derived carbons, *Journal of the Electrochemical Society* 165 (2018) F1199-F1205.

V **J.M. Linge**, H. Erikson, A. Sarapuu, M. Merisalu, M. Rähn, L. Matisen, V. Sammelselg, K. Tammeveski, Electroreduction of oxygen on nitrogen-doped graphene oxide supported silver nanoparticles, *Journal of Electroanalytical Chemistry* 794 (2017) 197–203.

VI **J.M. Linge**, H. Erikson, M. Mooste, H.-M. Piirsoo, T. Kaljuvee, A. Kikas, J. Aruväli, V. Kisand, A. Tamm, A.M. Kannan, K. Tammeveski, Ag nanoparticles on mesoporous carbon support as cathode catalyst for anion exchange membrane fuel cell, *International Journal of Hydrogen Energy* 48 (2023) 11058–11070.

VII **J.M. Linge**, H. Erikson, P. Ritslaid, A. Kikas, V. Kisand, J. Aruväli, J. Kozlova, A. Tamm, A. Sarapuu, K. Tammeveski, Ag sputter-deposited on MnO_2-carbon nanotube nanocomposites as electrocatalysts for oxygen reduction reaction in alkaline media, *Catalysts* 13 (2023) 976.

VIII **J.M. Linge**, H. Erikson, A. Kasikov, M. Rähn, V. Sammelselg, K. Tammeveski, Oxygen reduction reaction on thin-film Ag electrodes in alkaline solution, *Electrochimica Acta* 325 (2019) 134922.

IX **J.M. Linge**, D. Kozhemyakin, H. Erikson, S. Vlassov, N. Kongi, K. Tammeveski, Silver nanowire-based catalysts for oxygen reduction reaction in alkaline solution, *ChemCatChem* 13 (2021) 4364–4371.

X **J.M. Linge**, V. Briega-Martos, A. Huzler, B. Fritsch H. Erikson, K. Tammeveski, S. Cherevko, On the stability of carbon supported Ag electrocatalysts for alkaline oxygen reduction and evolution reactions, (manuscript in preparation)

Author's contributions:

Paper I: The author was responsible for material preparation, electrochemical testing and data analysis. The author is responsible for the interpretations of electrochemical results and writing the manuscript.

Paper II: The author was responsible for material preparation, electrochemical testing and data analysis. The author is responsible for the interpretations of electrochemical results and writing the manuscript.

Paper III: The author was responsible for material preparation, electrochemical testing and data analysis. The author is responsible for the interpretations of electrochemical results and writing the manuscript.

Paper IV: The author was responsible for material preparation, electrochemical testing and data analysis. The author is responsible for the interpretations of electrochemical results and writing the manuscript.

Paper V: The author was responsible for material preparation, electrochemical testing and data analysis. The author is responsible for the interpretations of electrochemical results and writing the manuscript.

Paper VI: The author was responsible for material preparation, electrochemical testing and data analysis. The author is responsible for the interpretations of electrochemical results and writing the manuscript.

Paper VII: The author was responsible for material preparation, electrochemical testing and data analysis. The author is responsible for the interpretations of electrochemical results and writing the manuscript.

Paper VIII: The author was responsible for electrochemical testing of the material and data analysis. The author is responsible for the interpretations of electrochemical results and writing the manuscript.

Paper IX: The author was responsible for big part of the electrochemical testing of the material and data analysis. The author is responsible for the interpretations of electrochemical results and writing the manuscript.

Paper X: The author was responsible for electrochemical testing of the material and data analysis. The author is responsible for the interpretations of electrochemical results and writing the manuscript.

2. ABBREVIATIONS AND SYMBOLS

A_r	electroactive surface area
ads	adsorbed
AEM	anion exchange membrane
AEMFC	anion exchange membrane fuel cell
AgNPs	silver nanoparticles
AgNWs	silver nanowires
AST	accelerated stability test
BET	Brunauer-Emmett-Teller theory
$C_{O_2}^b$	oxygen concentration in bulk solution
CDC	carbide-derived carbon
CNT	carbon nanotubes
CV	cyclic voltammetry
d	diametre
D_{O_2}	oxygen diffusion coefficient
E	potential
$E_{1/2}$	half-wave potential
E^0	standard electrode potential
ECS	engineered catalyst support
EDS	energy dispersive X-ray spectroscopy
F	Faraday constant
FC	fuel cell
fcc	face-centered cubic
GC	glassy carbon
GDL	gas-diffusion layer
GO	graphene oxide
Gr	graphene
HAADF	high-angle annular dark field
HMT-PMBI	hexamethyl-p-terphenyl-poly(benzimidazolium)
HR-STEM	high-resolution scanning transmission electron microscopy
I	current
I_d	disc current
I_r	ring current
I_k	kinetic current
ICP-MS	inductively coupled plasma mass spectrometry
IL-TEM	identical-location transmission electron microscopy
j	current density
j_d	diffusion-limited current density
j_k	kinetic-limited current density
k	electrochemical rate constant
K-L	Koutecky-Levich
n	number of electrons transferred
N	collection efficiency of the ring electrode

NG	N-doped graphene
NGO	N-doped graphene oxide
NrGO	N-doped reduced graphene oxide
MA	mass activity
MC	mesoporous carbon
MEA	membrane-electrode assembly
MWCNT	multiwalled carbon nanotube
ORR	oxygen reduction reaction
Pb_{upd}	lead underpotential deposition
P_{max}	peak power density
PSD	pore size distribution
PVP	polyvinylpyrrolidone
RDE	rotating disc electrode
RH	relative humidity
RHE	reversible hydrogen electrode
RRDE	rotating ring-disc electrode
rGO	reduced graphene oxide
SA	specific activity
SCE	saturated calomel electrode
SEM	scanning electron microscopy
SFC	scanning flow cell
SHE	standard hydrogen electrode
SSA	specific surface area
STEM	scanning transmission electron microscopy
TEM	transmission electron microscopy
TGA	thermogravimetric analysis
UPD	underpotential deposition
v	potential scan rate
VC	Vulcan XC-72R carbon
XRF	X-ray fluorescence
XPS	X-ray photoelectron spectroscopy
XRD	X-ray diffraction
v	kinematic viscosity of the solution
ω	rotation rate of the electrode

3. INTRODUCTION

Numerous applications such as fuel cells, metal-air batteries, and hydrogen peroxide production benefit from the oxygen reduction reaction (ORR) studies. Oxygen reduction proceeds via either direct 4-electron or 2-electron pathway, and the formed hydrogen peroxide can be further reduced or disproportionate [1]. Former is preferred for the fuel cells (FCs) and metal-air batteries and latter for hydrogen peroxide electrosynthesis. To overcome high overpotentials of the ORR, highly active Pt and Pd electrocatalysts are used [2, 3]. However, these platinum group metals are expensive, so cheaper alternatives are highly topical [4, 5]. One option is to use silver as it has shown electrocatalytic activity for ORR that in alkaline media approaches that of platinum [1, 4, 5].

This work compares Ag catalysts which were prepared using different deposition methods on various support materials. To understand the impact these methods and materials had on the size of Ag nanoparticles (AgNPs), their dispersion, catalysts' overall activity, and stability for the ORR in alkaline conditions, the rotating disc electrode (RDE) method was used. The end goal was to prepare suitable cathode catalysts for anion exchange membrane fuel cells (AEMFC).

In the first two parts of the thesis, Ag was electrodeposited onto clean glassy carbon (GC) electrode by varying the time the electrode was kept under the deposition potential. In the first part, the aqueous $AgNO_3$ and KNO_3 solution was used [I]. In the second part, the non-aqueous acetonitrile solution of $AgClO_4$ and $LiClO_4$ was employed [II]. In the third part of the thesis, AgNPs were deposited onto four different high surface area carbon supports keeping deposition time and potential constant but varying the upper potential limits [III]. This was done to limit the growth of AgNPs. First three parts were conducted to develop tuneable electrochemical deposition method to produce small and evenly distributed AgNPs for the ORR [I-III]. In the fourth part of the thesis, AgNPs were chemically deposited on two differently pre-treated commercial carbide-derived carbons using $NaBH_4$ as the reducing agent. As these carbon materials have high porosity, the effect of porosity on the AgNP size and electrocatalytic activity was studied. The prepared catalysts were tested for ORR and hydrogen peroxide reduction reaction to determine these catalysts viability as the cathodic catalysts for AEMFCs [IV]. In the fifth part of the thesis, AgNPs were deposited onto nitrogen-doped graphene oxide using three different reducing agents ($NaBH_4$, glycerol and ascorbic acid). The purpose of the work was to evaluate if different reducing agents and nitrogen-doped carbon support play a significant role in the prepared catalysts [V]. In the sixth part of the thesis, six Ag-based catalysts were synthesised, four of which were prepared onto commercial mesoporous nitrogen-doped carbon substrates. For comparison, the other two were prepared onto the conventional Vulcan XC-72R carbon support. The reducing agents applied were $NaBH_4$ and hydrazine hydrate. To evaluate the effects of mesoporous catalyst supports, these materials

were synthesised and tested for their electrocatalytic activity towards the ORR in half-cell configuration, as well as anion exchange membrane fuel cell [VI]. In the seventh part of the thesis, Ag layers with three different nominal thicknesses of 5, 10, and 20 nm were sputter-deposited onto two synthesised MnO_2_MWCNT substrates. This was done to prepare more stable and active Ag-based composite catalysts for the ORR [VII]. In the eighth part of the thesis, thin Ag films with five thicknesses were deposited onto clean GC electrodes. The nominal thicknesses were 0.5, 1, 2, 5 and 10 nm. The prepared electrodes were tested for the ORR and for the hydrogen peroxide reduction [VIII]. In the ninth part of the thesis, commercial Ag nanowires with three different diameters (35, 90 and 120 nm) were purchased and electrochemically tested for the ORR [IX]. In the tenth part of the thesis, the catalyst materials prepared in part [VI] were tested for stability studying Ag dissolution [X]. This was done to further investigate stability and catalyst degradation regarding the AEMFC application.

4. LITERATURE OVERVIEW

4.1 The oxygen reduction reaction

In the field of AEMFC and metal-air batteries the efficiency of oxygen reduction reaction is highly important and thus has been studied extensively. The oxygen is reduced to hydroxide ions on the cathode side of an AEMFC stack and is limited by sluggish first electron transfer to oxygen molecule on platinum group metal catalysts. The ORR may follow multiple pathways and two main pathways are direct four-electron pathway and 2+2 electron pathway [6–8]. The direct four electron pathway is preferred as it does not produce hydrogen peroxide or keeps it minimal. The hydrogen peroxide if produced may diffuse into solution and at high enough concentrations can start corroding cathodic catalysts and reacting with ion exchange membranes of the fuel cells.

The relevant ORR pathways in alkaline environment are [9]:

Direct four electron pathway:

$$O_{2,\,ads} + 2H_2O + 4e^- \rightarrow 4OH^- \qquad E^0 = 0.401\ V \qquad (1)$$

and 2+2 electron pathway:

$$O_{2,\,ads} + H_2O + 2e^- \rightarrow HO_2^- + OH^- \qquad E^0 = -0.065\ V \qquad (2)$$

$$HO_2^-{}_{,\,ads} + H_2O + 2e^- \rightarrow 3OH^- \qquad E^0 = 0.867\ V \qquad (3)$$

E^0 is standard potential vs. SHE.

The ORR mechanisms have been thoroughly studied on Pt electrodes [10, 11]. In alkaline media a mixture of 4 and 2+2 electron pathways are most likely because of weaker O_2 adsorption and adsorbed product species, for example, OH_{ads} desorption, which enables OH_2^- production [12, 13]. The limiting factor in low temperature fuel cell technology development is the sluggish kinetics of the ORR, high price of the typically used catalysts such as Pt, low long-term stability, and poor resistance to poisoning [14].

Chatenet and co-workers tested bulk Pt and Ag as well as catalysts prepared by depositing Pt and Ag nanoparticles onto carbon support, and found that in both cases Pt and Ag catalysts catalyse the ORR to form water and that the catalysts demonstrated first order kinetics in relation to oxygen concentration in the solution [15]. Density functional calculations and Monte Carlo simulation show that the adsorption of intermediates is the main factor that determines the ORR activity on Ag [16, 17]. More specifically, strongly adsorbed OH^- ions and weak O_2 adsorption decreases the electrocatalytic ORR activity of Ag. Furthermore, on Pt structures, functional calculations have been used to analyse the energetics of oxygen molecule dissociation reactions [10]. These calculations have implied that during the first step, oxygen adsorbs more favourably to the defect-rich sites: steps, kinks, and corners[10]. Furthermore,

chemisorbed oxygen molecules tend to diffuse onto flat facets nearby, on which weakly bound OH species form and are thus easily released [10]. During the O_2 reduction, the oxygen molecule, before its O-O bond is broken, adsorbs to the surface of the catalysts. The catalyst then participates in O_2 activation during which oxygen-containing adsorbates (O_{ads}) form on the catalyst surface [18]. The energy of the O-O bond has been determined to be 498 kJ mol^{-1}, and catalysts help to break this bond, thus catalyse the ORR at a sufficient rate [19]. It follows that high ORR activity depends on the strength of O_2 chemisorption to a catalyst surface and weaker adsorption of the adsorbed product species to the catalyst surface [18, 20].

4.2 Oxygen reduction reaction on bulk Ag electrodes

It has been demonstrated that the ORR in alkaline media proceeds via a 4-electron pathway on Pt as well as on Ag [15]. Although Pt is more active when it comes to the ORR performance, the cost favours Ag [21]. On single crystal Ag(hkl) the ORR tends to proceed via 2+2 electron pathway [22]. The ORR on Ag is highly structure sensitive as electrocatalytic activity is the highest on Ag(110) and lowest on Ag(100), while Ag(111) shows intermittent activity [22]. At the same time, activation energy is highest for Ag(100), intermediate for Ag(111), and lowest for Ag(110) [22]. It stems from OH^- ions blocking the active centres for O_2 molecules on Ag(110) to a higher degree in comparison to Ag(111) [22]. Additionally, the adsorption of OH^- ions depends on potentials [22]. It has been demonstrated that on Ag(111) in 0.1 M KOH the hydrogen peroxide yield falls below 2.5%, while in acidic 0.1 M $HClO_4$ solution OH_2^- yield depends on potential region [12]. Furthermore, during the ORR process at first hydrogen peroxide starts to form. The ORR then reaches regions where reduction via a mixture of 2 and 4 electron pathways is more prevalent. Finally, the ORR at the highest overpotentials starts to follow the complete 4-electron pathway [12]. Importantly, the adsorption of spectator species play an important role in determining whether the ORR follows 2- or 4-electron pathway [12]. Comparing electrocatalytic activities of bulk Ag and nanostructured silver, O_2 molecules are reduced to OH^- ions on both surfaces; however, the ORR on bulk Ag yields higher amounts of hydrogen peroxide [13]. This difference stems from more defective surface of Ag bulk and the electroactive sites being blocked for two-site O_2 molecule adsorption by still adsorbed OH species leading to hydrogen peroxide formation [13].

Exceptional electrocatalytic activity can be ascribed to high-Miller-index differently stepped Ag surfaces that Ag nanomaterials abundantly possess and density functional theory calculations has been used to model the ORR on these surfaces [23]**.** High-Miller-index Ag surfaces have been studied due to their higher electrocatalytic activity as they possess different layer separation and higher amount of available bonding sites than lower-Miller-index Ag surfaces [24]. However, high-Miller index catalysts are short lived as most this type of

catalysts have increased surface energies which eventually lead to their reorganisation to thermodynamically more stable configurations [25].

4.3 Oxygen reduction reaction on nanostructured Ag electrodes

Silver is a promising alternative to replace Pt catalysts as cathode materials, yet only if it is used in a dispersed form [26]. The behaviour of different Ag nanostructures' electrocatalytic activity has been thoroughly studied [27–31]. For example, on Ag nanodecahedra predominantly with Ag(111) single crystal facet the ORR proceeds via a direct 4-electron pathway, while on nanocubes with (100) facet, it follows a 2+2 electron pathway [27]. The differences in the ORR activity come from weaker OH^- adsorption to the Ag(111) facet, which in turn provides higher number of electroactive centres in comparison with nanocubes with Ag(100) facets [27]. Similarly, on electrodeposited Ag nanosheets with mainly Ag(111) facets the ORR follows a 4-electron pathway [28]. Nonetheless, on triangular Ag nanoparticles with predominant Ag(111) the ORR may follow a mix of 2 and 4-electron pathways [29]. If Ag is electrodeposited using surfactants (e.g. PVP), the crystalline growth in the direction of (111) is inhibited, and only Ag(111) is allowed to form [28]. Therefore, the ORR on Ag nanosheet arrays proceeds to water formation. Similar behaviour has been observed with Ag nanoplatelets prepared using sodium citrate as the capping agent [30]. At Ag terraces and edge sites, the ORR follows different reaction pathways; at the former, it follows a 4-electron pathway, and the latter, a 2-electron pathway [31]. It has been shown that 100 nm Ag nanoplatelets had the electron transfer number (*n)* value of 3.27, while 135 nm nanoplatelets had *n* value of 3.16 [29]. The ORR electrocatalytic activities depend on Ag nanoparticle size [32]. For example, smaller e.g., 4.1 nm particles favour two-electron pathway while larger ones e.g., 174 nm follow a 4-electron pathway [29, 33–35]. In case of Ag nanocubes, particles size increase from 12 nm to 38 nm resulted in decrease in specific activity [34]. In addition, triangular 99 nm Ag particles were reported to be more active than 136 nm counterparts [29]. Similarly, Lu and co-workers found that 0.7 nm Ag nanoclusters showed higher electrocatalytic activity than 3.3 nm nanoparticles, as mass activity (MA) was higher for 0.7 nm Ag nanoclusters. In addition, the ORR in both cases was suggested to follow 2+2 electron pathway (because of capping agents used) [35]. Wang and co-workers reported that Ag particles with the size of 3–5 nm show higher activity than slightly larger 6–8 nm and 12–15 nm AgNPs [36]. In addition, it was observed that the MA of Ag grows if Ag nanoparticles size and Ag nanowire diameter decreases [37]. However, some contradicting results have been obtained [33, 37], indicating that smaller Ag particles have facets and corners which catalyse 2-electron reduction, while larger ones catalyse predominantly 4-electron reduction [33, 38]. Ag nanowires (AgNWs), however, have a unique structure with one dimension in nanoscale and peculiar physicochemical properties, that provide higher aspect ratio

compared to silver nanoparticles [37]. Similarly, AgNWs have high surface area, which is useful in fuel cells [26]. In addition, it has better mass-transfer of oxygen molecules to the catalyst surface, and greater long-term potential cycling stability [37]. AgNWs with 25, 40, 50, and 60 nm diameters were studied and showed increase in the specific activity and mass activity in the decreasing order of diameter of the AgNWs [37]. On small Ag nanoparticles the ORR kinetics are influenced by size effects [39]. Ohyama and co-workers claim that Ag nanoparticles of 10 nm in size do not influence Ag specific activity and that Ag nanoparticles smaller than 3 nm already show quantum dot and size effects as they have large number of unsaturated Ag atoms [39].

Bidault and Kucernak have tested fuel cell system that consists of only Ag metal, where porous silver was used as membrane, catalyst support and charge collector [40, 41]. Ag catalysts produced by plasma-jet method with a 16–17 nm diameter were electrochemically highly active and stable [42]. In addition, Ag nanofibers due to their porous structure possess better mass transfer and have shown one of the highest electrocatalytic activities so far, as the ORR onset potential value was 1.041 V vs. RHE, half-wave potential of 0.848 V, and peak potential of 0.864 V vs. RHE [43]. This is also attributed to the effects of microstructure's large curvature, which helps accumulating more electrons, and additionally, the exposed Ag(110) facets play an important role in the enhanced ORR electrocatalytic activity. Yang and co-workers used γ-radiation to prepare AgNPs by varying ionomer concentration as a capping agent [44]. When the ionomer concentration was 320 ppm the prepared Ag catalyst showed the highest mass (24 A g_{Ag}^{-1}) and specific activities (137 μA cm_{Ag}^{-2}, at 0.75 V vs. RHE) [44].

4.4 Oxygen reduction reaction on carbon-supported Ag catalysts

Ag-based catalysts have been prepared on various carbon substrates that have different effects on Ag catalysts' electrocatalytic activity. The catalysts prepared onto carbon nanotubes can surpass bulk polycrystalline Ag materials in electrocatalytic activity [45]. However, carbon supports generally catalyse the ORR via a 2-electron pathway [46, 47]. For example, graphene itself is not very active [48], but the efficiency of carbon substrate graphene can be further increased by adding Vulcan XC-72R carbon powder, which increases the porosity of the substrate [49]. In addition, the activity of carbon supports such as graphene can also be increased by N-doping [50, 51]. For example, Cao and co-workers studied Ag-based catalysts prepared onto N-doped hollow carbon tubes and found that these catalysts showed high electrocatalytic activity during the ORR due to high porosity and synergistic effect between Ag nanoparticles and surface N-species [52]. Pyridinic and graphitic N adsorb O_2 more strongly than Ag nanoparticles; and during the synthesis of N-doped graphene AgNW composite catalysts, AgNWs addition creates channels within graphene sheets that increase oxygen diffusion [53]. Moreover, bonding interactions between the

Ag nanoparticles and N-species are shown to further improve Ag-based catalysts ORR activity. These bonding effects have been corroborated by the XPS and surface enhanced Raman spectroscopies [54]. For intermittent summary, several factors increase the ORR activity on N-doped carbon (graphene): size of Ag nanoparticles, contact between the Ag nanoparticles and the surface N-species, high mobility of charged species on nitrogen-doped graphene and the higher amount of pyridinic nitrogen [55]. The ORR on carbon supported Ag catalysts may follow 2 and 4 electron pathways simultaneously [31, 33, 56, 57]. For example, silver has been deposited onto graphene and resulting catalysts have shown to catalyse the ORR via 4-electron pathway [57, 58]. Vega-Cartagena and co-workers, in their recent work, electrochemically prepared Ag catalysts on Vulcan XC-72R carbon support using ring-disc slurry electrodeposition technique by varying deposition potentials from 0.0 V to 0.4 V vs. RHE [59]. Material prepared using 0.1 V vs. RHE possessed AgNPs that were 7.5 nm in size and yielded the highest electroactivity in terms of mass activity (4,765 mA mg^{-1}) and the *n* value was 3.5 [59]; the higher activity was reasoned to come from higher amount of AgO_2 formed through AgNPs combining with O_2 on AgNPs surface [59, 60].

The Ag loading on carbon support plays an important role influencing the ORR mechanism and Ag catalysts electrocatalytic activity. When the distance between the particles is large enough, the intermediate hydrogen peroxide has less nearby active centres to be further reduced. In other words, to have an effective Ag catalyst, the interparticle distance should be less than 30 times that of particle radius [61, 62]. Thusly, Ag loadings from 20 wt% to 60 wt% are suitable as they have sufficient amount of Ag nanoparticles that catalyse a 4-electron O_2-reduction, while at 10 wt% and lower loadings the Ag interparticle distance is higher and some of the ORR proceeds on carbon support via 2-electron pathway [31, 63, 64]. Guo and co-workers found that peroxide yield on 10 wt% Ag/C catalyst increased by 10% while on Ag catalysts with Ag loading of 20 wt% and up ring currents of the rotating ring-disc electrode (RRDE) showed negligible hydrogen peroxide yield [63]. This is supported by Neumann and co-workers, who discovered that the increase of the Ag interparticle distance decreases the water yield [62]. It has been suggested that 20 wt% Ag loading is the most optimal. Ag/C with 20 wt% loading has shown higher current densities and mass activities [65] and excellent durability towards methanol poisoning as compared to the Pt/C catalyst. High loadings of Ag may hinder the efficiency of the ORR. Namely, 40 and 60 wt% Ag catalysts show the *n* values close to 4; however, if Ag loading is increased to 80 wt%, the *n* value starts to fall [66]. Ag-based catalyst prepared by magnetron sputtering of 15 nm nominal Ag layer onto MWCNTs showed higher electrocatalytic activity in comparison to bulk Ag and unmodified MWCNTs [45].

In addition, Ag is a good catalyst for peroxide reduction [67] and studying hydrogen peroxide reduction is highly important when exploring the ORR kinetics as it is an inevitable side product for ORR and Ag has been employed as peroxide sensor material [68, 69].

4.5 Oxygen reduction on Ag catalysts on nanocomposite supports

Another approach in producing electrocatalytically more active and stable Ag-based catalysts is to use transition metal oxides. Typically, used metal oxides for this are Mn_xO_y-s [70–74]. The benefits of manganese oxides are numerous: their low cost, high abundance, and promising electrocatalytic activity. Moreover, MnO_2 has a d-band electronic structure that is similar to that of platinum [70, 71]. According to electron paramagnetic resonance measurements the addition of Ag to α-MnO_2 decreases oxides electrical resistance [70]. In turn, manganese oxides addition to Ag causes ligand effects between the metals, where transition metal oxide affects the metals' electronic structure and d-band centre [70, 72]. In addition, Ag and manganese oxides compensate each other's shortcomings to catalyse indirect 4-electron O_2 reduction. For example, oxygen adsorption to Ag is weak and disproportionation of OH_2^- ion is fast. In contrast, manganese oxide adsorbs oxygen strongly, and OH_2^- disproportionation is slow [72, 73]. Ag addition to manganese oxide increases current densities in CV-s and LSV-s and decreases the charge transfer resistance [71]. Sun and co-workers report that pure MnO_2 tends to catalyse the ORR via a 2-electron pathway, and with Ag added the resulting catalyst reduces adsorbed O_2 molecules via a 4-electron pathway [72]. Moreover, Mn_3O_4 proximity to Ag particles can result in Ag_2O formation that in turn provides increased numbers of electrochemically active sites on the composite catalyst, and further increases Ag catalysts activity during the ORR [63, 75]. Stability of the Ag-manganese oxide composites may originate from negligible hydrogen peroxide formation. Mn_3O_4 on carbon substrates tends to increase O_2 molecule side-on adsorption; furthermore, Mn_3O_4 and Ag proximity results in hydrogen peroxide, which has formed on manganese oxide, to disproportionate quickly on Ag surface (the ensemble effect) [72, 74, 75]. Another aspect concerning this type of composites electrocatalytic activity and stability is oxygen vacancies that Mn_3O_4 close to Ag particles tends to create by affecting Ag particles surface states [76]. The oxygen vacancies help to better facilitate O_2 reduction, attract electrons to the reaction centres and act as the additional ORR active sites [76].

5. EXPERIMENTAL

5.1 Electrode preparation

Before catalyst coating, the glassy carbon disks (GC, d = 5 mm, GC-20SS, Tokai Carbon; Japan) were first polished on 1200 and 4000 grit emery papers and then on alumina slurries (1 and 0.3 μm, Buehler), followed by cleaning with 2-propanol and Milli-Q water in an ultrasonic bath for 5 min in each.

GC disks with drop-cast Ag catalysts (Ag loading: 0.06 mg cm^{-2} unless otherwise stated), saturated calomel electrode (SCE) and Pt wire were the working, reference and counter electrodes, respectively. For comparison, polycrystalline bulk Ag disc (d = 5 mm, 99.95%, Alfa Aesar) embedded into Teflon holder and 20 wt% commercial Pt/C (E-TEK) catalyst were used.

5.1.1 Electrodeposition of AgNPs from aqueous media

The electrochemical deposition of silver was carried out from Ar-saturated (99.999%, AGA) 1 mM $AgNO_3$ (99%, Sigma-Aldrich) aqueous solution containing 0.1 M KNO_3 (99%, Lachema) as supporting electrolyte [I]. The electrodeposition was conducted at a constant potential of -0.5 V vs. SCE at different durations (from 0.1 s to 300 s). These electrodes are designated as Agx, where the x marks the electrodeposition time in seconds.

5.1.2 Electrodeposition of AgNPs from non-aqueous media

The electrochemical deposition of silver was carried out from Ar-saturated (99.999%, AGA) 0.1 mM $AgClO_4$ (97%, water-free, Sigma-Aldrich) solution in acetonitrile containing 0.1 M $LiClO_4$ (99.8%, water-free, Sigma-Aldrich) [II]. The deposition was performed at a constant potential of -0.5 V vs. SCE for up to 300 s. The electrodeposited Ag electrodes are labelled as Ag_x, where x marks the deposition time in seconds.

5.1.3 Electrodeposition of AgNPs onto different carbon supports

Graphene oxide (GO) was prepared using a modified Hummers method [III] [50, 77]. Briefly, a known amount of graphite was added into a glass flask, to which concentrated H_2SO_4 (97%, Honeywell) was added, and the mixture was sonicated for 1 h. Then the temperature of the mixture was raised to 35 °C and held for 18 h. In the following step, the mixture was cooled down in an ice bath and deionised water was added to it. Afterwards, hydrogen peroxide was added followed by washing the suspension with hydrochloric acid. The resulting mixture was rinsed with copious amount of Milli-Q water (Millipore, Inc.) and dried at 75 °C.

As a next step the obtained GO was doped with nitrogen using dicyandiamide (DCDA, Aldrich) as described previously [50]. Briefly, after GO was mixed with polyvinylpyrrolidone (PVP, Thermoscientific) in the mixture of

deionised water and ethanol, DCDA was added. The mixture was first sonicated for 2 h and subsequently dried at 75 ºC and then pyrolysed at 800 ºC for 2 h in a constant flow of nitrogen gas. After that, the furnace was allowed to cool down and nitrogen-doped graphene (NGO) was collected.

Before the electrodeposition, 20 µl of suspensions (1 mg of carbon material in 1 ml ethanol) of NGO, graphene (Gr, Strem Chemicals), Vulcan carbon XC-72R (C, Cabot Corp.), and multi-walled carbon nanotubes (MWCNT, diameter 30±15 nm, length 5–20 µm, purity >95%, NanoLab Inc., USA) were drop-casted onto GC electrodes. MWCNTs were acid-treated before use according to a procedure reported previously [78]. Electrodeposition of Ag was carried out in aqueous 0.1 M KNO_3 solution containing 0.01 mM $AgNO_3$ by cycling between the deposition potential of -0.6 V and different upper potential (0.3 and 0.4 V) for 100 cycles with scan rate of 100 mV s^{-1}. The resulting materials were designated according to the upper potential value. For example, for NGO-supported Ag catalysts when it was 0.3 V the catalyst was named Ag/NGO1 and when the upper potential was 0.4 V then Ag/NGO2. Other Ag-based electrocatalysts were named in the same way.

5.1.4 Preparation of Ag/CDC catalysts

The carbide-derived carbon (CDC) samples CDC1 and CDC2 were purchased from Skeleton Technologies OÜ (Estonia). Both CDC samples were synthesised from titanium carbide powder (H.C. Starck, Ø<4µm) via high-temperature chlorination [IV]. The CDC1 material was, prior to the purchase, additionally physically activated with H_2O vapour at 900 °C. The detailed descriptions of the synthesis and physical activation processes can be found elsewhere [79]. After the preparation of the CDCs and before the synthesis of Ag nanoparticles to a CDC support, the CDCs were ball-milled in ethanol environment for three cycles of 30 min. at 800 rpm to decrease the CDC grain size. Ag/C catalysts of 40 wt% were prepared by utilizing a method in which sodium borohydride was used as the reducing agent [80]. First, Vulcan carbon XC-72R, CDC1 and CDC2 were dispersed in water. Then a known amount of sodium citrate was added. After that $AgNO_3$ was added to achieve 40 wt% Ag/C and finally silver nanoparticles were synthesised using $NaBH_4$ (99%, Aldrich). These catalysts are denoted as Ag/C, Ag/CDC1 and Ag/CDC2, respectively. After the synthesis, the reaction mixtures containing Ag/C and Ag/CDC catalysts were vacuum-filtered and dried at 70 °C overnight.

5.1.5 Preparation of Ag/NGO catalysts

The synthesis of the nitrogen-doped graphene oxide support is described in section 5.1.3. The silver nanoparticles were synthesised using three different methods, and for all methods the nominal Ag content was fixed at 40 wt% [V]. First, citrate stabilised AgNPs were prepared by reducing $AgNO_3$ with $NaBH_4$ in an aqueous solution in the presence of NGO and sodium citrate [80]. This

catalyst is designated as Ag/NGO3. For the preparation of the second catalyst (Ag/NGO4) an aqueous solution of glycerol and sodium hydroxide was added to the suspension of NGO containing $AgNO_3$ [81]. The third catalyst (Ag/NGO5) was prepared using ascorbic acid as a reducing agent [82]. In this synthesis as with previous suspension of NGO and $AgNO_3$ was made and the Ag^+ ions were reduced by slowly adding ascorbic acid to the mixture under constant stirring. After the synthesis of Ag/NGO catalysts, the suspensions were filtered and dried at 75 ºC.

5.1.6 Preparation of Ag catalysts on mesoporous ECS

Ag-based catalyst materials were synthesised from silver nitrate using two simple citrate methods, as described in the literature [80, 83] with sodium borohydride ($NaBH_4$, 99%, Aldrich) and hydrazine hydrate ($H_4N_2 \cdot xH_2O$, 64%, Acros Organics) as reducing agents [VI]. Ag was deposited onto three different carbon supports such as (i) nitrogen-doped mesoporous carbon ECS004201 and (ii) ECS004601 (Pajarito Powder, LLC) and Vulcan carbon XC-72R (Cabot Corp.). In case of $NaBH_4$, 60 mg of the carbon supports were dispersed in 200 ml Milli-Q water in an ultrasonic bath for two hours. Later 62.9 mg (40 mg Ag) of silver nitrate ($AgNO_3$, ≥ 99%, Sigma-Aldrich) was added, and the suspension was stirred for 30 min on a magnetic stirrer. Then 348.6 mg of sodium citrate tribasic dihydrate (Fluka, puriss p.a. ≥ 99%) was added to the synthesis solution, and 5 min later, 313.8 mg of $NaBH_4$ was quickly dissolved in a 10 ml vial in ice-cold Milli-Q water and added to the reaction mixture, the vial was washed twice with the same ice-cold Milli-Q water, and Ag nanoparticles were synthesized. After the addition of $AgNO_3$, the synthesis beaker was set onto a magnet stirrer and constantly stirred at ~700 rpm. After the addition of the reducing agent, the synthesis solution was stirred overnight. To break down the excess citrate, KOH was added; after 2 h the stirring was stopped, and the catalyst material was left to precipitate overnight. The catalyst materials were vacuum-filtered and dried at 60 °C overnight. The prepared catalysts are named as Ag/4201_BH4, Ag/4601_BH4 and Ag/VC_BH4. No. 4201 represents ECS004201 carbon support; no. 4601 represents ECS004601; VC represents Vulcan carbon substrate, and BH4 represents reducing agent $NaBH_4$.

When the reducing agent was hydrazine hydrate, the same carbon materials were dispersed in 200 ml Milli-Q water for 2 h, 71.3 mg of $AgNO_3$ was added, the suspension was stirred on a magnetic stirrer for 0.5 h, then 24.7 mg of sodium citrate was added, and the solution was stirred at 700 rpm for 5 min. Before adding the reducing agent, the catalyst suspension was heated to 50 °C, and then 91 ml of hydrazine hydrate solution was added (91 ml of Milli-Q water + 170 µl of 64% hydrazine hydrate). The reaction temperature was 50 °C, and the mixture was stirred at 700 rpm for 2 h, after which the heating was switched off, and the synthesis solution was left to cool overnight. All consecutive steps were the same as when using the $NaBH_4$. The Ag-catalyst materials synthesised

are denoted analogously as in previous paragraph, but HH, which represents reducing agent hydrazine hydrate, was used instead of BH4 at the end.

5.1.7 Sputter-deposition of Ag onto MnO_2-MWCNT composites

Acid treatment of commercial MWCNTs (Nanocyl) was carried out according to a previously reported protocol [78]. MnO_2_MWCNT1 substrate was synthesised using previously published method [84] by adding 25 mg of acid-treated MWCNT to 20 ml of deionised (Milli-Q, Millipore, Inc.) water and sonicated for 30 min [VII]. 228.4 mg of $MnSO_4 \times H_2O$ (Sigma-Aldrich, ≥ 98%) was added to the suspension and sonicated further for 30 min. A fresh $KMnO_4$ (Thermo Scientific, ACS reagent) solution was prepared by dissolving 704.8 mg of $KMnO_4$ in 30 ml of deionised water. Under vigorous stirring, MWCNT suspension and $KMnO_4$ solution were heated up to 80 °C and $KMnO_4$ solution was quickly added to the suspension. The synthesis suspension was kept under vigorous stirring for 1h until the purple colour disappeared. It was then washed, filtered with ethanol and deionised water and dried overnight at 60 °C.

MnO_2_MWCNT2 was synthesised in one pot method where 10 mg of untreated MWCNTs were added to 10 ml of deionised water, to which 100 mg of $KMnO_4$ was added and dissolved [85]. The synthesis mixture was stirred at room temperature for 6 h. Next, 50 µl of concentrated H_2SO_4 (Honeywell, 97% puriss, p.a.) was added, and the synthesis mixture was stirred at room temperature for 1h. The solution was then heated to 80 °C and stirred for an additional 60 min. The synthesis mixture was then removed from the heat source, poured into a 1 l flask containing 0.5 l of deionised water and filled up to the 1 l mark. The suspension was filtered, washed with ethanol and a copious amount of deionised water and dried overnight at 60 °C.

50 µl of ink was drop-casted onto a freshly polished GC electrode to have a loading of 0.25 mg cm^{-2}, and the electrode was dried under N_2 gas flow [84, 86]. Ag was sputter-deposited onto the substrates with nominal thicknesses of 5, 10, and 20 nm. Magnetron sputtering was carried out, as reported earlier [45, 87, 88], and in this study using a Ag target in the Ar atmosphere. The deposition chamber pressure was 3×10^{-3} mbar, the DC power of 2 W, and the distance between target and substrate was 6 cm. Si plates were used as additional substrates to determine the deposited Ag loading by X-ray fluorescence (XRF).

5.1.8 Preparation of thin-film Ag electrodes

Ag was deposited onto GC electrodes using Vacuum Service OY evaporation device in which the base pressure was below 1×10^{-6} Torr [VIII]. The deposition rate was held constant at around 0.2 nm s^{-1} for thinner and up to 1 nm s^{-1} for thicker coatings. The nominal thickness of Ag films was varied from 0.5 to 10 nm.

5.1.9 Silver nanowire-based catalysts

Prior to the use, commercially available suspensions of silver nanowires with diameters of 35, 90 and 120 nm (Blue Nano, USA) were purified by first keeping the nanowire material in 1 M KOH solution for 1 h, then washed by multiple consecutive rinsing and centrifugation with Milli-Q® water [IX]. Final suspensions (1 mg ml^{-1}) were prepared using 2-propanol (Merck). 30 µl of resulting ink was drop-casted onto freshly polished and washed GC electrodes.

5.1.10 The dissolution stability of Ag nanoparticles

The synthesis of tested materials Ag/MC (Ag/4201_HH) and Ag/VC (Ag/VC_HH) is described in section 5.1.6.

On-line electrochemical dissolution measurements

An inductively coupled plasma mass spectrometer (ICP-MS, Perkin Elmer, Nexion 350X) together with a three-electrode scanning flow cell (SFC) were used for the on-line electrochemical dissolution measurements employing a custom-made Labview software [X]. The potentiostat used for both SFC-ICP-MS and RDE measurements was a Gamry Reference 600. The electrode rotation rate was controlled with a MSR rotator (Pine Research). In SFC experiments the working electrode was a 5×5 cm glassy carbon plate covered with catalyst spots. For that, 0.2 µl of catalyst ink with concentration of 1 mg ml^{-1} in mixture of 2-propanol (20%) and Milli-Q water (80%) was drop casted to achieve (catalyst) spots with a radius ranging from 600 to 750 µm. Before each measurement, the GC plate was polished with alumina slurry with a grain size of 0.3 µm. The counter electrode was a GC rod with a diameter of 5 mm (HTW Sigradur G). The reference electrode was Ag/AgCl/3 M KCl electrode (Metrohm), and it is situated in the outlet channel of the SFC system to avoid contamination with chloride ions. The experiments were carried out in 0.05 M KOH solution (pH ≈ 12.7) prepared from KOH pellets (Sigma-Aldrich, p.a.). The electrolyte solution was purged with Ar gas. The average flow rate from SFC to ICP-MS is 3.5 µl s^{-1}. The time delay of electrolyte flow from the SFC to ICP-MS was accounted for and adjusted for a direct correlation between the potential and dissolution data.

Before the measurements, the ICP-MS was calibrated using 0.5, 1, and 5 ppb solutions of Ag standard. Before the electrolyte entered the ICP-MS it was mixed 1:1 with a 1% HNO_3 solution with 10-ppb internal standard (Rh) solution.

Electrochemical protocols

Ag dissolution was measured using both SFC and RDE methods. For SFC-ICP-MS measurements, in the case of *Protocol 1*, the lower potential limit 0.3 V vs. reversible hydrogen electrode (RHE) stayed the same, the upper potential limit was varied from 0.9 V to 1.8 V vs. RHE by increments of 0.1 V, and the potential scan rate was 10 mV s^{-1}. In *Protocol 2*, the lower potential limit was

0.3 V vs. RHE, the upper potential limit was 1.8 V vs. RHE, and two CVs were measured at a potential scan rate of 2 mV s^{-1} for better separation between anodic and cathodic dissolution peaks. The cyclic voltammetry response for these protocols was also recorded in the RDE configuration for obtaining smoother voltammetric profiles.

5.2 The physical characterisation of Ag-based catalysts

The surface morphology of the catalyst materials was characterised using scanning electron microscopy (SEM, Helios Nanolab 600, FEI) equipped with an energy dispersive X-ray spectrometer (EDS) analyser INCA Energy 350 (Oxford Instruments) and operated at 10 kV, and scanning transmission electron microscopy (STEM, Titan 200, FEI), equipped with energy dispersive X-ray spectrometer Super-X^{TM} system, operated at 200 kV. The X-ray photoelectron spectroscopy (XPS) analysis of catalyst samples was carried out using SCIENTA SES-100 instrument with Mg Kα X-ray source (incident energy of 1253.6 eV). The X-ray diffraction (XRD) analysis was carried out with the catalyst powders using Bruker D8 Advance diffractometer with Ni filtered Cu Kα radiation and analysed using software Topas 6 (Bruker, Germany). The Ag loading on the carbon supports was estimated by thermogravimetric analysis (TGA) in a Setaram Labsys Evo 1600 thermoanalyser in O_2 + Ar gas mixture (21:79 ratio).

The N_2 adsorption measurements for CDC samples were done at the boiling temperature of nitrogen (77K) using the NOVA touch LX2 (Quantachrome Instruments). Total pore volume (V_{tot}) was derived at P/P_0 of 0.97 and the calculation of the specific surface area (S_{BET}) was done corresponding to the Brunauer-Emmett-Teller (BET) theory [89]. The volume of micropores (V_{μ}) and the pore size distribution (PSD) were calculated from N_2 adsorption isotherms by using a quenched solid density functional theory equilibria model for slit-shape pores.

5.3 The electrochemical characterisation of Ag-based catalysts

The ORR current for the Ag-based catalyst materials was measured using an Autolab potentiostat/galvanostat PGSTAT30 (Metrohm Autolab B.V., The Netherlands) controlled by General Purpose Electrochemical System (GPES) or Nova software. The RDE measurements were carried out employing an EDI101 rotator and CTV101 speed control unit (Radiometer, Copenhagen). For the RRDE testing an AFMSRX rotator and MSRX speed control unit (Pine Research Instrumentation, Grove City, PA, USA) with Pine Instrument's fixed tip glassy carbon disk (0.164 cm^2) and Pt ring electrode was employed. The collection efficiency (N) of the RRDE tip was 0.25. The electrode rotation rate was varied from 360 to 4600 rpm. The electrodes were coated with 30 µL (50 µL in the seventh part of the work [VII] and 20 µl in the third part [III]) of Ag

catalyst ink suspension (1 mg mL^{-1}), which was prepared by weighing 2 mg of catalyst added to Milli-Q water (1.6 mL), 2-propanol or ethanol (0.4 mL) and 2 µL of Nafion dispersion (5 wt% in lower aliphatic alcohols, Sigma-Aldrich). Commercial 20 wt% Pt/C catalyst (E-TEK) was prepared by depositing the Pt/C suspension onto the GC electrode by drop-casting 10 µL of Pt/C ink at a Pt loading of 0.01 mg cm^{-2}. A potential scan rate of 10 mV s^{-1} was employed for oxygen reduction and peroxide reduction measurements. The background currents were measured and subtracted from the oxygen reduction current. From the ORR polarization curves recorded on all silver catalysts only anodic scans were used for further analysis. The oxygen reduction studies were carried out in O_2-saturated (99.999%, AGA) 0.1 M KOH (puriss p.a., Sigma-Aldrich) solution. Before the ORR studies, the electrodes were pre-conditioned by cycling in a potential range from -1.2 to 0 V vs. SCE in Ar-saturated 0.1 M KOH solution for 10 potential cycles with scan rate of 100 mV s^{-1}. Pre-conditioning is necessary as it affects the Ag-based catalyst material electrocatalytic activity towards ORR [38]. In this potential range, the silver catalyst surface is not yet oxidised and the rearrangement of AgNPs on all the carbon supports is avoided. The peroxide reduction experiments were conducted in Ar-saturated 0.1 M KOH solution containing 1 mM HO_2^-. In order to determine the electroactive surface area of silver, either Pb underpotential deposition experiments were conducted in Ar-saturated 0.1 M KOH containing 0.5 mM $Pb(NO_3)_2$ (≥99%, Sigma-Aldrich) or calculated from cathodic Ag reduction peaks of the obtained voltammograms after CV measurements where electrodes were cycled in potential range of -1.2 V and 0.4 V vs. SCE at 50 mV s^{-1} potential scan rate. After the electrochemical testing Ag was electro-chemically dissolved in Ar-saturated 0.1 M $NaClO_4$, (Merck) solution at scan rate of 50 mV s^{-1} and the mass of silver was calculated from the charge of the obtained stripping peak of the voltammogram.

All prepared electrodes were subjected to electrochemical testing in an O_2-saturated 0.1 M KOH solution in which RDE polarisation curves were measured at different electrode rotation rates. The obtained ORR polarisation data were analysed using the Koutecky-Levich (K-L) equation (Eq. 4).

$$\frac{1}{j} = \frac{1}{j_k} + \frac{1}{j_d} = -\frac{1}{nFkC_{O_2}^b} - \frac{1}{0.62nFD_{O_2}^{2/3}\nu^{-1/6}C_{O_2}^b\omega^{1/2}} \quad (4)$$

where j is the measured current density, j_k and j_d are the kinetic and diffusion-limited current densities, respectively, n is the number of electrons transferred per O_2 molecule, k is the rate constant for O_2 reduction, F is the Faraday constant (96,485 C mol^{-1}), ω is the rotation rate (rad s^{-1}), $C_{O_2}^b$ is the concentration of oxygen in the bulk (1.2×10^{-6} mol cm^{-3}) [90], D_{O_2} is the diffusion coefficient of oxygen (1.9×10^{-5} cm^2 s^{-1}) [90] and ν is the kinematic viscosity of the solution (0.01 cm^2 s^{-1}) [91].

To compare the intrinsic electrocatalytic activity of Ag-based catalysts, specific activities (SA) were calculated using (Eq. 5):

$$SA = I_k / A_r \quad (5)$$

where I_k is the kinetic current at a given potential and A_r is the electroactive surface area of silver. A_r was determined either from lead underpotential deposition (Pb_{upd}) or from Ag oxide reduction peak (obtained from cyclic voltammetry measurements).

The mass activities (MA) for ORR were calculated using the following equation (Eq. 6):

$$MA = I_k/m \quad (6)$$

where m is the mass of Ag on the electrode surface calculated either from the Ag dissolution experiments, or from the XRF data, or mass of the whole catalyst.

The amount of dissolved Ag was calculated by charge integration under the CV peaks from Ag stripping data using equation (Eq. 7):

$$m = \frac{M(Ag)*Q}{n*F} \quad (7)$$

where M is the atomic mass of Ag (107.87 u), Q is the charge, n is the number of electrons involved (n = 1), and F is the Faraday constant.

Data obtained from the RRDE measurements was used to determine the peroxide yield (Φ), which was calculated using the following equation (Eq. 8):

$$\Phi = \frac{200*\frac{I_R}{N}}{I_D+\frac{I_R}{N}} \quad (8)$$

where I_D and I_R are disk and ring currents, respectively, and N is the collection efficiency (0.25). In addition, the number of electrons transferred per O_2 molecule (n) was also calculated using equation (Eq. 9):

$$n = \frac{4*I_D}{I_D+\frac{I_R}{N}} \quad (9)$$

The AEMFC performance for the Ag-based cathode catalysts (Ag/4601_BH4, and Ag/4201_HH materials) was evaluated with the membrane-electrode assemblies (MEA) that have an active area of 5 cm^2 and are fabricated using Sigracet 39BB gas diffusion layer (GDL), the AEM Aemion+ (AF2-HLE8-10-X, 10 μm), and Pt-Ru/C (Alfa Aesar) as the anode catalyst. MEAs with the commercial Pt/C (20% Pt) cathode catalyst was also evaluated for comparison. The catalyst inks were prepared and drop-casted onto GDLs. The loading of the

cathode catalysts was 2 mg cm^{-2} and the anode catalyst 0.8 $mg_{Pt\text{-}Ru}$ cm^{-2} [92]. Catalyst-coated GDLs and membrane were immersed in 3 M KOH solution for 1 and 3 days, respectively. The solution was changed once a day. The MEA was assembled in a single cell fuel cell using silicone gaskets with a torque of 9 N m. The potentiostatic polarization experiments were conducted in Greenlight Fuel Cell Test Station (G40 Fuel Cell System, Hydrogenics, Canada) using H_2 and O_2 gases (65% RH) with 1.0 NLPM flow rate at 65 °C with 200 kPa backpressure.

6. RESULTS AND DISCUSSION

6.1 O_2 reduction on electrodeposited Ag catalysts in alkaline media

In the first part of the work, Ag nanoparticles were synthesised onto clean GC electrodes using simple electrodeposition method in aqueous environment, where the GC electrodes were kept at Ag deposition potential -0.5 V vs. SCE at different durations [I]. The deposition times were 0.1, 10, 60, 180 and 300 s. The goal of this work was to improve and tune the electrodeposition method to achieve smaller Ag nanoparticles. The coatings were tested for the ORR in 0.1 M KOH solution using the RDE method. The measured GC electrodes with the deposited Ag particles were denoted as Ag0.1, Ag10, Ag60, Ag180 and Ag300.

6.1.1 SEM and XRD studies of the electrodeposited AgNPs

Figure 1 presents the SEM images of all the electrodeposited Ag catalysts. Initially bigger agglomerates of large particles (up to 200 nm) form; also, some smaller particles (ca 15 nm) can be observed. Same results were obtained with all parallel measurements. After 0.1 s of deposition a majority of the GC surface is still uncovered and clean. After 10 s of deposition (Figure 1c) the number of smaller particles is growing, and the number density of big agglomerates stayed the same. In addition, the particle size remained similar to the AgNPs deposited for 0.1 s. With further increase of the deposition time (60 s), the number of smaller particles increased and so did their size being about 23 nm. As expected, after the increasing of the deposition time to 180 s, the particles grew to about 30 nm and at 300 s the particles were about 45 nm in size. In addition, a number of Ag particles below 10 nm were still visible, showing that the electrodeposition occurs at random locations. The observation that big agglomerates form during the first 0.1 s suggests that initially there is no gradient of Ag^+ cations and the amount of silver ions near the surface is high enough, which enables the formation of agglomerates. After a gradient for Ag^+ ions formed, further deposition took place on the whole substrate. The particles deposited in this study are considerably smaller than those reported in the literature [93, 94] showing that careful selection of electrodeposition parameters is crucial for the preparation of AgNPs with the desired size and number density on the GC surface. These observations suggest that as the silver surface area increases with increasing the electrodeposition time, the overall electrocatalytic activity towards the ORR should also increase.

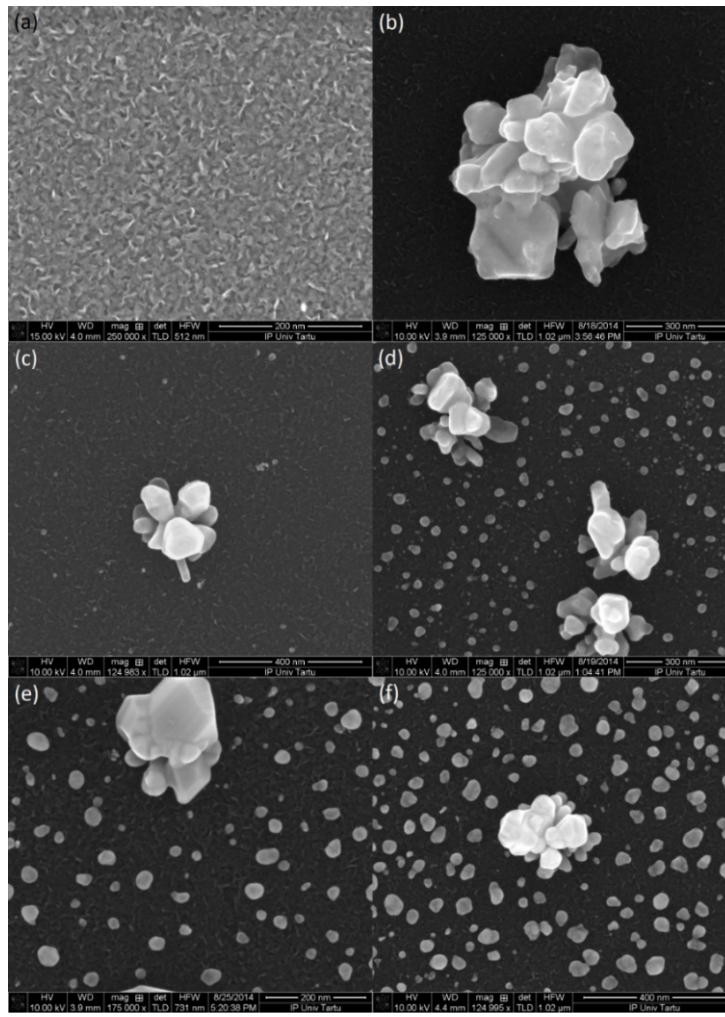

Figure 1. SEM micrographs of (a) bare GC, (b) Ag0.1, (c) Ag10, (d) Ag60, (e) Ag180 and (f) Ag300 samples.

To obtain some additional information about the structure of the Ag coating, the XRD analysis was carried out with Ag300 (Figure 2). It can be observed from the diffraction pattern that Ag(111) reflection has highest contribution of silver crystal facets at 2θ = 38°. The XRD peak of Ag(200) is located at 44° and Ag(220), Ag(311) and Ag(222) have been also identified. In addition to Ag, broad XRD peaks originating from the GC substrate are present. The reflection of graphitic carbon (002) is centred at ca. 26° and the (101) peak at ca. 43°. After further inspection of the spectra, it was determined that the crystallites are not isometric. For further analysis, the Scherrer equation was employed, and the average size of the Ag crystallites were calculated to be 159-395 nm. These values coincide with the big agglomerates/particles observed on the SEM

images. Apparently, smaller Ag particles observed under the SEM have smaller contribution to the XRD signal, whereas a slight effect may also originate from the differences in the preparation of the sample.

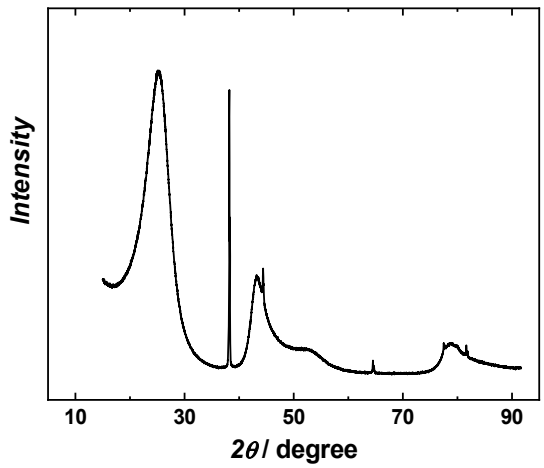

Figure 2. XRD pattern for Ag300.

6.1.2 ORR studies on the electrodeposited AgNPs

A comparison of the RDE polarisation curves for the ORR on electrochemically deposited silver catalysts in O_2-saturated 0.1 M KOH solution is presented in Figure 3a. All the Ag/GC electrodes have significantly higher ORR activity than the clean GC disk as the ORR onset and half-wave potentials shift to more positive values with increased electrodeposition time. In addition, these electrodes have a current minimum at about -0.9 V vs. SCE, which decreases with increasing of the electrodeposition time. It could be related to a change in the reaction mechanism and a shortage of Ag on the surface of the GC at the initial stage of deposition causing the observed current minimum to be more prominent. Similar current minimum has been noticed in several studies, and Yang and co-workers have observed this using Ag nanoclusters comprising of 2 to 5 Ag atoms [60]. Despite the current minimum appearance, it was found that the peroxide yield remained below 15%. Using carbon nanotube-supported Ag catalyst this minimum was suppressed [45] and we may assume that by increasing the amount of Ag this feature would fade. This feature could be related to some specific crystallographic orientation as Blizanac and co-workers observed this minimum only for Ag(111) and that the peroxide yield increased at the location of this minimum [22].

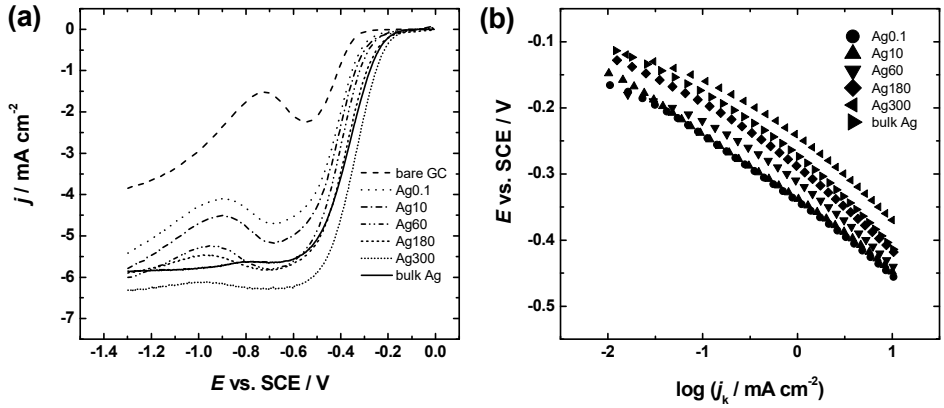

Figure 3. (a) Comparison of the RDE polarisation curves for the ORR on the electrodeposited AgNPs. (b) Tafel plots for the ORR derived from (a). Test solution: O_2-saturated 0.1 M KOH. ω = 1900 rpm, v = 10 mV s^{-1}.

For further analysis of the RDE data on O_2 reduction the Tafel plots were constructed (Figure 3b) and the corresponding slope values were determined. The Tafel slope values for all the prepared AgNP covered GC electrodes were similar being in the range between -70 and -80 mV. These Tafel slope values are consistent with those previously reported for magnetron sputtered Ag nanoparticles on MWCNTs [45] and more recently on AgNPs prepared by pulse charge deposition [42]. In addition, constantly changing Tafel slope values have been reported for Ag, meaning that at low current densities a slope value of -80 mV rises to -130 mV when scanning to high current densities [22]. Blizanac and co-workers explained the change in the Tafel slope by potential dependent surface coverage of OH_{ads} and change of the Frumkin parameter [22]. In addition, the Tafel slope values of -90 mV for bulk Ag and -120 mV for AgNPs have been reported [95, 96]. Innocenti and co-workers observed a change in the Tafel behaviour for small quantities of Ag as compared to higher amounts of metal [97]. For lower amount of Ag, the Tafel slope had a constantly changing value, but starting from Ag loading of 14.2 µg cm^{-2} the material exhibited clearly linear Tafel ranges. On the other hand Novikova and co-workers who studied the ORR on small deposited Ag quantities reported linear Tafel plots with the slope value between -112 and -138 mV, which corresponds to slow transfer of the first electron to the adsorbed O_2 molecule in the charge transfer stage [31].

After the ORR measurements the electrodes were transferred to Ar-saturated 0.1 M KOH solution containing Pb^{2+} cations in order to give an estimation of the electroactive surface area (A_r) of silver [98]. In their study, Kirowa-Eisner and co-workers found that the charge for the monolayer of Pb_{upd} on Ag corresponds to 0.26 mC cm^{-2}. As expected from the SEM measurements the A_r value increased with increasing the deposition time, being lowest for Ag0.1

(A_r = 0.015 cm^2) and highest for Ag300 (A_r = 0.278 cm^2). The specific activity for O_2 reduction was calculated at -0.25 V vs. SCE using equation (Eq. 5), where A_r was obtained from the Pb_{upd} data. It was revealed that the SA value did not depend on the deposition time. It was 0.81, 0.79, 0.82, 0.83 and 0.79 mA cm^{-2} for Ag0.1, Ag10, Ag60, Ag180 and Ag300, respectively. This suggests that there is no clear particle size effect in the size range from 15 to 45 nm. Interestingly, it has been demonstrated that the particle size effect is present for Ag particles in 100 nm scale in which smaller particles have higher activity [29]. Wang and co-workers have reported that the ORR activity increases with decreasing the Ag particle size from 12-15 nm to 3-5 nm, which was suggested as the optimum AgNP size for ORR [36]. The ORR activity has been shown to increase further when particle size decreased from 3.3 to 0.7 nm [35], which might originate from the fraction of unsaturated silver atoms and the quantum size effect [39]. The results obtained in this study are in agreement with those reported by Ohyama and co-workers, which showed that the Ag particle size above 10 nm have negligible effect on the SA value [39]. However, it needs to be noted that Campbell and Compton have studied Pb_{upd} extensively from sodium potassium tartrate solution and they concluded that UPD is observed for Ag particles larger than 50 nm but it is absent for smaller AgNPs [99].

After the electrochemical measurements, the electrodes were transferred to Ar-saturated 0.1 M $NaClO_4$ solution in which silver was electrochemically stripped from the surface of the GC electrode. The mass of Ag was calculated from the stripping charge using Eq. 7. It was found that the mass of silver grows almost linearly with the deposition time and only the initial growth is rapid as the amount of Ag^+ cations near the GC surface is higher at the first stage of the deposition. Within few seconds a gradient of Ag^+ cations is formed and the growth of silver mass starts to increase linearly as metal cations are transferred to the GC electrode. Based on the SEM micrographs the initially formed Ag particles are somewhat bigger, which might indeed be due to the high initial concentration of Ag^+ cations adjacent to the GC electrode surface and the particles formed in the next stage of deposition are smaller because of the cation concentration gradient. The mass-activities for O_2 reduction were calculated at -0.25 V vs. SCE using the dissolved Ag mass (Eq. 7) and kinetic current values at the given potential (see the experimental section Eq. 6). As with the specific activities, the MA values did not essentially depend on the mass of the electrodeposited Ag and were in the range of 50-58 A g^{-1}.

Additionally, to analyse the ORR kinetics on the prepared Ag catalysts, the ORR polarisation curves were recorded at various electrode rotation rates and the obtained data were treated by the K-L equation (Eq. 4). Figure 4a shows a typical set of the RDE polarisation curves of Ag180 and the respective K-L plots are presented in Figure 4b. The *n* value was slightly lower than four for most of the electrodeposited Ag catalysts, and for Ag300 and bulk Ag the *n* value was close to 4. These *n* values suggest that some peroxide is formed on all Ag/GC electrodes and the ORR proceeds at least partially via series 2+2

electron pathway. It has been demonstrated that the residues from the synthesis of Ag nanoparticles may reduce the electron transfer number [100]. Lu and co-workers found that polyvinylpyrrolidone protected Ag nanorods catalyse incomplete two-electron reduction of O_2, while unprotected Ag nanorods catalyse the four-electron oxygen reaction to form water. Also, silver decorated MWCNTs, without any further additives, catalyse the ORR to form water [45]. Another explanation could be related to the crystallographic orientation of the electrodes, as it has been suggested that Ag(111) catalyses the direct four-electron reduction of oxygen [27]. As the XRD measurements showed that the Ag particles deposited onto GC have preferential Ag(111) orientation and as even the Ag/GC electrodes prepared using smaller deposition time have *n* value close to 3.5 then we may assume that indeed the ORR on Ag(111) proceeds via direct $4e^-$ pathway. However this is in contradiction with the findings reported by Blizanac and co-workers who determined that the Ag(110) plane is the most active single crystal facet of Ag for the ORR [22].

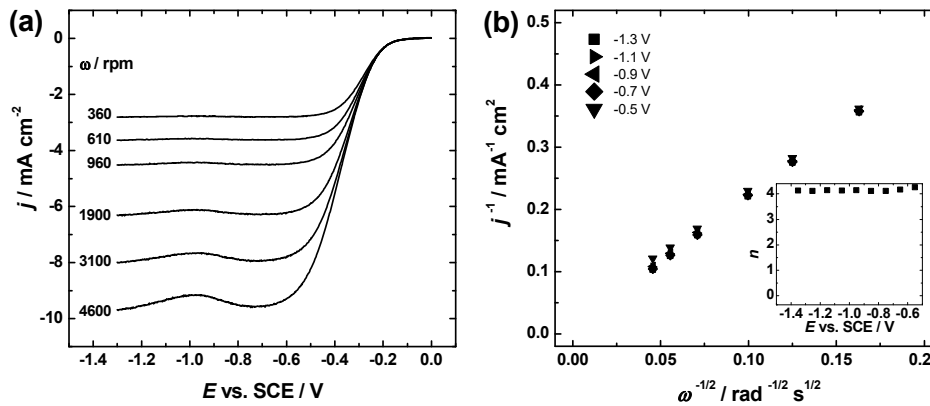

Figure 4. (a) RDE polarisation curves of Ag180 for ORR at different electrode rotation rates. (b) Koutecky-Levich plots at various potentials; inset shows the dependence of *n* on potential. Test solution: O_2-saturated 0.1 M KOH. v = 10 mV s^{-1}.

6.1.3 H_2O_2 reduction studies on electrodeposited Ag NPs

It was of considerable interest to study the electroreduction of HO_2^- on silver coatings in order to evaluate the electrocatalytic properties of the Ag-based catalysts towards this important electrochemical reaction. Ag180 was selected for the HO_2^- electroreduction studies. Figure 5a presents the RDE polarisation curves for peroxide reduction on Ag180 in Ar-saturated 0.1 M KOH containing 1 mM HO_2^-. The current minimum at -0.9 V is evident as could be observed also for the ORR (see Figure 3a). The RDE data was analysed using the K-L equation (Eq. 4, Figure 5b) and 1.36×10^{-5} cm^2 s^{-1} as diffusion coefficient for HO_2^- [101]. The number of electrons transferred per HO_2^- anion was found to

be close to two. Neumann and co-workers observed that with increasing the AgNP concentration on the substrate the peroxide reduction increases as a result of peroxide diffusion over the Ag nanoparticle array instead of over individual Ag particles [62].

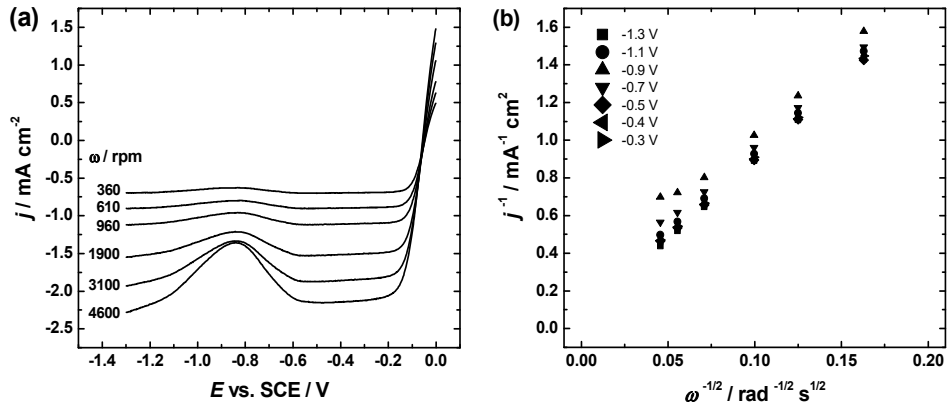

Figure 5. (a) RDE polarisation curves of Ag180 for the HO_2^- reduction at different electrode rotation rates. (b) Koutecky-Levich plots at various potentials; inset shows the dependence of n vs. E. Test solution: Ar-saturated 0.1 M KOH containing 1 mM HO_2^-. v = 10 mV s^{-1}.

As no surfactants or additives were used in this study to prepare AgNPs, it could be concluded that the n value lower than four is caused by the insufficient amount of silver catalyst on the substrate surface. With carbon-supported AgNPs, it has been suggested that 10 wt% Ag is not sufficient to catalyse the complete 4-electron reduction of oxygen [61, 63, 64].

The results presented in this part of the thesis suggest that electrodeposition is a viable method to prepare AgNPs with tuneable size for the ORR and the peroxide reduction reaction in alkaline media.

6.2 ORR on electrodeposited AgNPs from non-aqueous media

In the second part of the work, Ag nanoparticles were synthesised onto clean GC electrodes using similar electrodeposition method as in the previous part but in non-aqueous environment [II]. The GC electrodes were similarly kept at the Ag deposition potential of -0.5 V vs. SCE for 0.1, 10, 60, 180 and 300 s. The purpose of this work was to evaluate whether the change of aqueous environment to a non-aqueous (acetonitrile) improves the electrodeposition method to achieve smaller AgNPs than in the previous part of the work. The catalysts were

tested for the ORR in 0.1 M KOH solution using the RDE method. The measured GC electrodes with the five Ag particle deposition times were labelled as $Ag_{0.1}$, Ag_{10}, Ag_{60}, Ag_{180} and Ag_{300}.

6.2.1 SEM studies of the electrodeposited AgNPs

Figure 6 displays SEM images of AgNPs deposited onto the GC surface for 10, 60, 180 and 300 s. After 0.1 s, the surface is almost completely empty and only some Ag particles are observed. The size of the particles and the number density grow with increasing the deposition time. After 10 s the Ag particles are approximately 45 nm in diameter, after 60 s the particles have grown to about 55 nm, 180 s yields 75 nm particles and after 300 s they are about 90 nm. In addition, smaller particles can be observed from the SEM images revealing that there are sufficient amount of surface sites for the deposition of Ag. Shorter deposition times mostly yield individual particles and when the deposition time is increased, the particles start to merge as their size and the surface coverage increase.

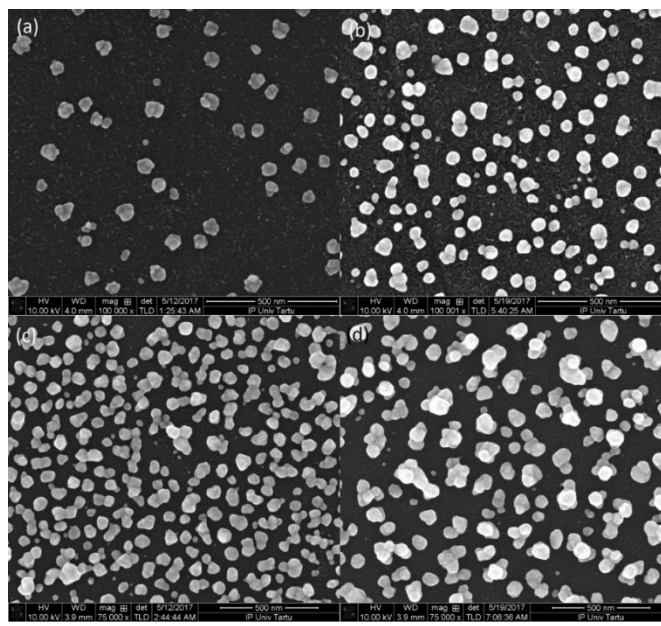

Figure 6. SEM images of (a) Ag_{10}, (b) Ag_{60}, (c) Ag_{180} and (d) Ag_{300} samples.

6.2.2. CV experiments on the electrodeposited AgNPs

For electrochemical characterisation, the electrodeposited Ag electrodes were subjected to potential cycling in the potential range between -1.2 and 0.4 V vs. SCE. A comparison of CV results is presented in Figure 7, and it can be ob-

served that there are no characteristic peaks in the potential window from -1.2 to -0.1 V. The oxidation of silver surface starts at about 0.1 V and two characteristic peaks are observed. A small peak at 0.16 V corresponds to both dissolution of Ag and the formation of a monolayer of Ag_2O. However the origin of this peak has been considered to be complex as there have been several propositions for the origin of this peak [102]. The large peak at 0.32 V consists of two peaks, which have been associated with the formation of bulk phases AgOH and Ag_2O [63, 102, 103]. The reduction of Ag oxides takes place at the cathodic scan at about 0.05 V. In the literature, the oxide reduction peak has been used to calculate the electroactive surface area of Ag [66, 103]. However, as Ag_2O and AgOH form closely during the silver oxidation then this approach may not be reliable.

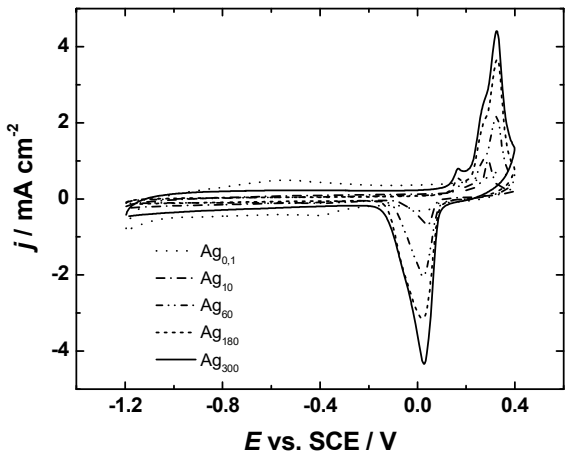

Figure 7. Cyclic voltammograms of the electrodeposited Ag coatings in Ar-saturated 0.1 M KOH. $v = 50$ mV s^{-1}.

6.2.3 ORR studies on the electrodeposited AgNPs

Figure 8a displays a set of RDE polarisation curves of the ORR on electrodeposited Ag_{180}. The polarisation curves have a minimum at about -0.9 V. When comparing the Ag-coated electrodes (Figure 9a) then it is obvious that the minimum decreases with increasing the deposition time. This minimum may originate from the change in reaction mechanism or could be related to specific crystallographic orientation as discussed above (see sub-section 6.1.2) [I] based on the findings in Ref. [22].

The RDE data was analysed using the K-L equation (Eq. 4). The value of n was 4 in the whole potential range studied with Ag_{180}, Ag_{300} and bulk Ag. For Ag_{60} the n value was somewhat lower than 4 while for $Ag_{0.1}$, Ag_{10} it was between 2.5 and 3.5. As expected, from the RDE polarisation curves the lowest electron transfer number was in the potential range in which the minimum in polari-

sation curve is observed. It has been reported in several publications that the amount of Ag is crucial for the ORR activity [62-64]. For example, Guo and co-workers determined that the silver content has to be above 20% in Ag/C catalyst to catalyse $4e^-$ reaction pathway [63]. Neumann and co-workers described that the surface coverage with Ag particles is important for complete reduction of oxygen [62]. They proposed that when peroxide is formed on the disk surface it diffuses away from the surface if the distance of Ag particles is more than 30 times the nanoparticle radius. If the number density of particles is increased, then the peroxide escape is lower and the formed H_2O_2 is further reduced on the neighbouring Ag particles. Similar conclusion can be made from the work in which 174 nm and 4.1 nm Ag nanoparticles were studied, as the ORR on bigger particles proceeded via 4-electron pathway and on smaller particles via both 4-electron and 2-electron pathway simultaneously [33]. Singh and Buttry compared the ORR on AgNPs to that on polycrystalline silver [13]. The K-L analysis revealed that in certain conditions the AgNPs have higher *n* value than that of polycrystalline Ag. They attributed the higher fraction of two-electron pathway on bulk Ag to the fact that its surface had more defects, which prevents the two-site adsorption of O_2 molecule, as this is required for direct 4-electron pathway. The K-L equation (Eq. 4) only gives an overall electron transfer number, and it is impossible to differentiate between the two-step two-electron reaction pathway and the direct 4-electron pathway. It has been demonstrated that the ORR on silver low-index single crystal facets is structure sensitive and it has been suggested that the ORR proceeds via series pathway on these surfaces [22]. However, Wang and co-workers studied the ORR on shape-controlled Ag particles (nanodecahedra and nanocubes) [27]. They proposed that the ORR on nanodecahedra, enclosed with Ag(111) crystal facet, proceeds via a direct 4-electron pathway and via series pathway on Ag nanocubes, enclosed with Ag(100) facets.

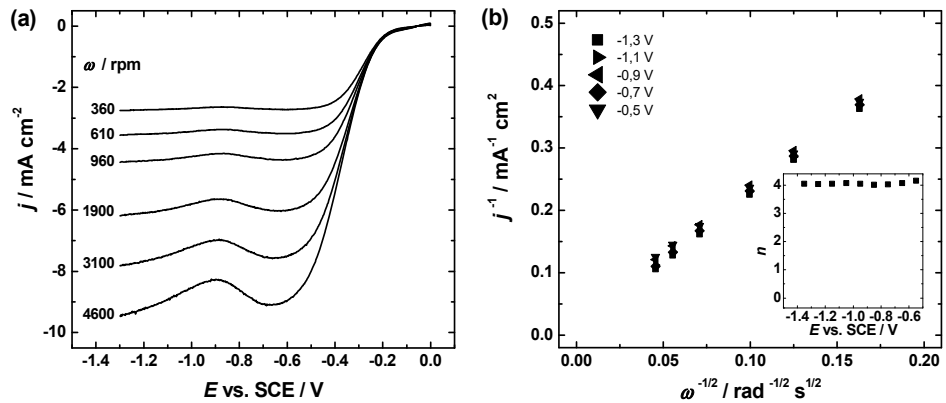

Figure 8. (a) A set of RDE polarisation curves for ORR on Ag_{180} in O_2-saturated 0.1 M KOH. v = 10 mV s^{-1}. (b) K-L plots derived from (a) and inset shows the potential dependence of *n*.

The use of electrochemical deposition of Ag is a good choice, as in wet chemical synthesis stabilizers must be used. The nanoparticles have to be cleaned from the synthesis residues as they may affect the reaction pathway by increasing the contribution of two-electron pathway [100]. In more detail, Lu and co-workers synthesised Ag nanorods in the presence of PVP and tested their electrocatalytic activity before and after the removal of the PVP. It was observed that removing of the PVP from the surface of silver increased the ORR current densities as well as the number of electrons transferred per O_2 molecule.

From the comparison plots (Figure 9), the Ag_{180} and Ag_{300} electrodes are more active than bulk Ag electrode. As simple comparison of the ORR polarisation curves is not suitable, then the SA values were calculated. The SA for O_2 reduction was calculated using the kinetic current at -0.25 V vs. SCE in equation (Eq. 5), where A_r was obtained from Pb_{upd} measurements [98]. The calculated SA values are given in Table 1. Pb_{upd} method has been utilised for the determination of surface area of Ag-based catalysts in previous works [45, 95, 96], however it was found not to be suitable for Ag particles with certain characteristics [99]. Namely, it has been demonstrated that the underpotential deposition of lead does not take place on Ag particles smaller than ca. 50 nm. As we have also smaller than 50 nm Ag particles present on the GC electrode surface, then the calculated SA values give only an estimation. According to this estimation, the SA value does not depend on the deposition time. However, when the A_r is calculated by charge integration under the CV peaks (Figure 7) then the SA value decreases with increasing the deposition time. However, the value of 420 μC cm^{-2} used in this work and in previous studies [66, 103] corresponds to a monolayer of Ag oxides on the surface, but in the case of bulk silver electrode, layers of oxides and hydroxides can be formed, which makes the estimation of A_r less reliable [102]. Even though the surface areas calculated from the oxide peak might be overestimating, they at least take into account the small particles and thus we conclude that the SA value decreases with increasing the Ag deposition time. Similarly, the specific activity for O_2 reduction has been shown to decrease with increasing Ag nanocubes size from 12 to 38 nm [34].

After the oxygen reduction studies, the initially deposited Ag coating was electrochemically stripped from the GC electrode and from the stripping peak the mass of Ag was determined using equation Eq. 7. As expected, the mass of Ag on the electrode increased with increasing the deposition time. The MA values (Eq. 6) for O_2 reduction were calculated at -0.25 V vs. SCE using the dissolved Ag mass and kinetic current values at the given potential. The mass activities were 60-75 A g^{-1} and no tendency on the deposition time was observed.

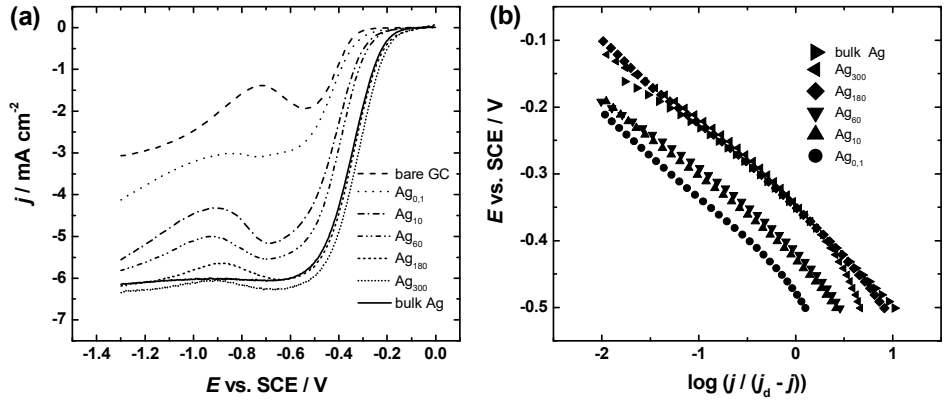

Figure 9. (a) Comparison of the ORR polarisation curves in O_2-saturated 0.1 M KOH at 1900 rpm. v = 10 mV s^{-1}. (b) Mass-transfer corrected Tafel plots for O_2 reduction derived from (a).

The particle size effect of Ag catalysts has been discussed in several studies [29, 35, 36, 39]. Wang and co-workers reported that Ag particles of 3-5 nm in size have the best performance in zinc-air batteries [36]. Lee and co-workers compared 98.7 and 136.1 nm triangular nanoplatelets with preferential (111) crystal facet and concluded that the smaller particles exhibit higher electrocatalytic activity towards the ORR [29]. Lu and Chen compared the ORR activities of 0.7 and 3.3 nm AgNPs and found that 0.7 nm nanoclusters showed better electrocatalytic activity than 3.3 nm particles [35]. Ohyama and co-workers investigated the ORR on Ag particles with different morphologies and crystallite sizes [39]. The highest n value was obtained for particles with smallest crystallite size, while the specific activity was higher for 62 and 113 nm crystallites. The difference in activity was explained by differences in the surface defects, as the material with higher proportion of defects (subsurface oxygen species and Ag_2CO_3) had lower electron transfer number. Despite having lower n value the specific activity was higher on particles with defective surface as they suggested that the higher affinity with oxygen enables to conduct the charge transfer with lower activation energy [39].

For further ORR kinetics analysis, the Tafel plots (Figure 9b) were constructed and the Tafel slope values were determined. The slope values were around -80 to -90 mV, and similar Tafel slope values have been reported earlier [42, 45]. Tafel slope values from -112 to -138 mV have been reported for small quantities of Ag catalyst [31]. Even the Tafel slope value as high as -157 mV has been reported for carbon-supported AgNPs [65]. Furthermore, constantly changing Tafel slope values have been reported and change in the slope values has been attributed to the potential dependent surface coverage of OH_{ad} and Frumkin parameter [22]. Chao and co-workers reported two Tafel slope values for Ag nanocubes, -60 mV at low current densities and about -120 mV at higher current densities, which was suggested to originate from the changes in the

adsorption conditions of oxygen intermediates [34]. In addition, a change in the Tafel slope value has been attributed to the difference in Ag loading on the electrode, as small quantities of Ag yield constantly changing slope value and when critical Ag loading has been obtained the slope becomes linear [97]. In those studies, the rate-determining step has been reported to be the transfer of the first electron to O_2 molecule.

Table 1. Kinetic parameters for oxygen reduction on electrodeposited Ag in 0.1 M KOH. ω = 1900 rpm. MA and SA values are calculated at -0.25 V vs. SCE.

Catalyst	Tafel slope (mV)	$E_{1/2}$ vs. SCE (V)	SA[a] (mA cm^{-2})	SA[b] (mA cm^{-2})	MA (A g^{-1})
$Ag_{0.1}$	-82	-0.43	0.93	0.16	62
Ag_{10}	-80	-0.41	0.82	0.14	75
Ag_{60}	-79	-0.39	0.94	0.10	71
Ag_{180}	-84	-0.34	0.83	0.09	67
Ag_{300}	-88	-0.32	0.79	0.09	66

[a] A_r determined from Pb_{upd}.
[b] A_r determined from Ag oxide reduction.

6.3 ORR on Ag catalysts electrodeposited on nanocarbon supports

In the third part of the work, Ag nanoparticles were electrodeposited onto four different (NGO, Gr, MWCNT and Vulcan carbon) high surface area carbon supports [III]. Compared to previous parts, the deposition potential (-0.6 vs. SCE) and the deposition time were kept constant, whereby upper potential limits (0.3 and 0.4 V) were varied. The purpose of this work was to study the effects of the different electrodeposition parameters on the ORR electrocatalytical activity on various nanocarbon supports. It included studying the effects that support materials and upper potential limit had on AgNPs size and distribution on different carbon supports. The measured catalysts were denoted as Ag/NGO1, Ag/Gr1, Ag/ MWCNT1, and Ag/C1 when the upper potential limit was 0.3 V and Ag/NGO2, Ag/Gr2, Ag/MWCNT2, and Ag/C2 when the upper potential limit was 0.4 V.

6.3.1 SEM studies of electrodeposited AgNPs on carbon supports

Figures 10 and 11 show SEM micrographs of Ag/NGO, Ag/MWCNT, Ag/Gr, and Ag/C catalyst materials where Ag was electrodeposited using two different upper potential limits of 0.3 and 0.4 V, respectively. The largest Ag particles are mostly agglomerates that are in the sub-micrometre size range. On all these SEM images, Ag particles are quasi-spherical. The average particle size of the Ag-based catalyst materials varies depending on the deposition procedure used

and the size distribution is wide. The Ag particles are randomly distributed on the carbon support. In previous works (see sub-sections 6.1.1 and 6.2.1), where AgNPs were electrodeposited onto bare GC disks using different deposition times yielded smaller nanoparticles than in this part [I, II]. During the electrodeposition the upper potential limit was varied. Using a more positive potential smaller AgNPs were deposited and their number density on the substrate surface was also lower. In addition to controlling the deposition potential and the time (or the number of potential cycles and the scan rate), the carbon support plays a great role in determining the AgNPs size and their distribution [104–106]. From Figure 10 on the MWCNT surface, the AgNPs are the smallest and the distribution of Ag particles is the widest if the more negative upper potential limit (0.3 V vs. SCE) was applied.

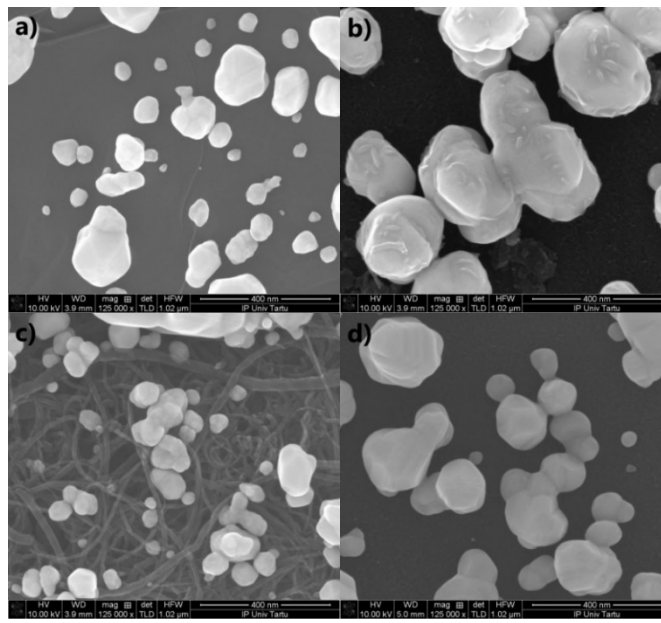

Figure 10. SEM images of (a) Ag/NGO1, (b) Ag/Gr1, (c) Ag/MWCNT1 and (d) Ag/C1 samples. The upper potential limit of 0.3 V vs. SCE was applied. Scale bar: 400 nm.

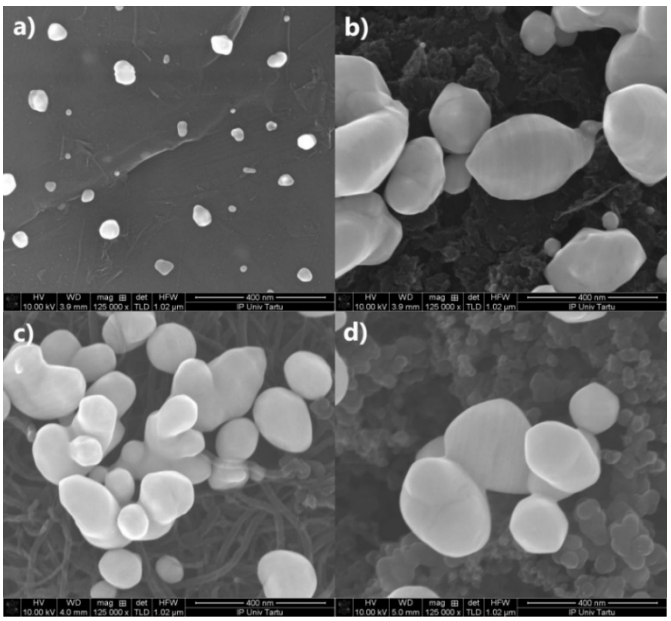

Figure 11. SEM images of (a) Ag/NGO2, (b) Ag/Gr2, (c) Ag/MWCNT2 and (d) Ag/C2 samples. The upper potential limit of 0.4 V vs. SCE was applied. Scale bar: 400 nm.

6.3.2 ORR studies on electrodeposited AgNPs on carbon supports

According to Figures 12a and 13a, all prepared Ag-based catalysts provide only single-wave polarisation curves with more positive onset and half-wave potentials than bulk polycrystalline silver electrode. From all the Ag-based catalyst materials studied, Ag/NGO1 possessed the highest electrocatalytic activity (see Table 2). It is evident that a more positive upper potential limit leads to lower $E_{1/2}$ values. In a control experiment, it was found that by selecting the upper potential limit of 0.5 V, the Ag nanoparticles started to dissolve and therefore less amount of silver is present on the carbon supports. The dissolution of Ag occurs when the upper potential limit is close to the silver redox potential ($Ag^{+}+e^{-}\leftrightarrow Ag^{0}$) of 0.7996 V vs. SHE [107].

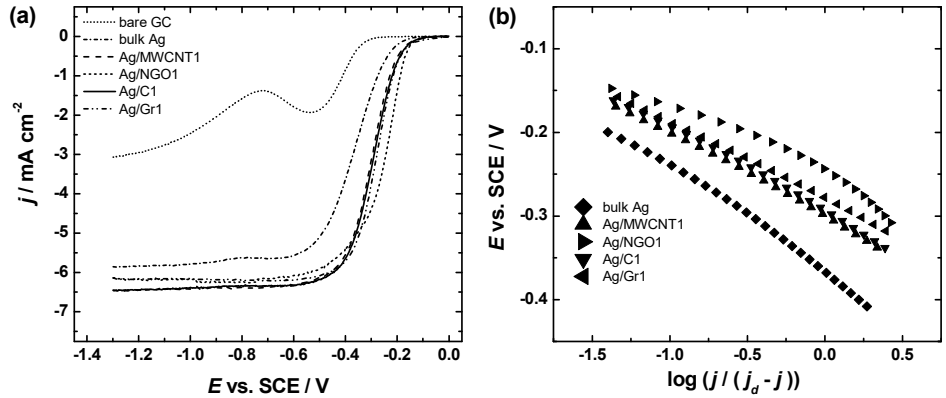

Figure 12. (a) Comparison of RDE polarization curves for oxygen reduction on Ag-based catalysts in O_2-saturated 0.1 M KOH solution, v = 10 mV s^{-1}, ω = 1900 rpm. The catalysts are prepared using different nanocarbon supports and the upper potential of 0.3 V. (b) Mass-transfer corrected Tafel plots for O_2 reduction on Ag-based catalysts. Data derived from (a).

For further analysis of the RDE results, the Tafel plots for ORR were constructed (Figures 12b and 13b). Tafel plots of polycrystalline silver, Ag/NGO1, and Ag/MWCNT1 electrodes are almost parallel. The Tafel slope values at low overpotentials are -92, -60, -95, and -93 mV for Ag/Gr1, Ag/NGO1, Ag/MWCNT1 and Ag/C1 catalysts, respectively. For Ag/Gr2, Ag/NGO2, Ag/MWCNT2, and Ag/C2 materials the slope values are -96, -59, -93, and -92 mV, respectively. The Tafel slope values determined in the present work are similar to those obtained for Ag-based catalysts in earlier publications (see sub-sections 6.1.2 and 6.2.3) [I, II] [42, 45]. Blizanac and co-workers reported Tafel plots for the ORR on Ag(hkl), where a change in slope values between -60 and -120 mV was observed. At lower current densities the Tafel slope was close to -80 mV and at higher current densities around -120 mV [22]. In addition, in a work where the ORR was investigated on Ag nanocubes, the Tafel slope values were -60 and -120 mV at low and high overpotentials, respectively. This change in slope values was explained to come from the changes in the adsorption properties of the oxygen intermediates [34]. Changes in the Tafel slope values can also originate from the differences in the Ag loadings on the electrodes, where small Ag loading gives changing slope values, and when critical Ag loading is reached the slope becomes linear [108]. In addition, Tafel slopes might be affected by incorrect solution resistance correction [96]. As the Tafel slopes determined in this work are close to the values reported in the literature, it can be concluded that the rate-determining step for the ORR is the slow transfer of the first electron to the adsorbed O_2 molecule [42, 45, 109-111].

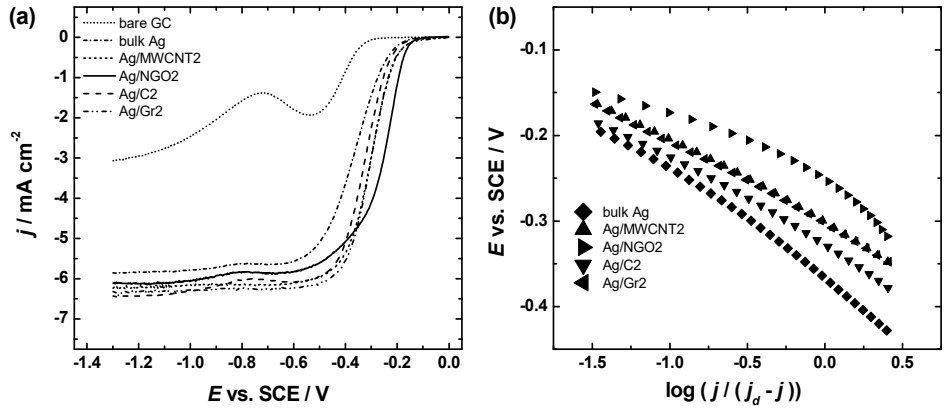

Figure 13. (a) Comparison of RDE polarization curves for oxygen reduction on Ag-based catalysts in O_2-saturated 0.1 M KOH solution, v = 10 mV s^{-1}, ω = 1900 rpm. The catalysts are prepared using different nanocarbon supports and the upper potential of 0.4 V. (b) Mass-transfer corrected Tafel plots for O_2 reduction on Ag-based catalysts. Data derived from (a).

The RDE data was analysed using the K-L equation (Eq. 4). The value of *n* was approximately four for all Ag-based catalysts in this study. From this result, it can be concluded that the ORR proceeds via a 4-electron transfer pathway, thus hydrogen peroxide formation is either almost completely avoided, or the formed hydrogen peroxide is immediately further reduced. However, the K-L analysis does not allow differentiating between the direct 4-electron and $2e^- + 2e^-$ pathways, because it yields an overall *n* value. Guo and co-workers and Fazil and co-workers have reported the *n* values close to four for 40 wt% Ag/CNT catalyst [63, 81]. For Ag nanowires [37], through plasma jet treatment prepared AgNPs [42], and Ag nanocubes [112] the *n* values close to 4 have been reported. Silver catalysts deposited onto carbon paper have shown similar *n* values [113]. In previous parts of the thesis, where AgNPs were electrodeposited onto bare GC substrate, and the deposition time was varied, the values of *n* grew with deposition time because of the higher mass of silver on the electrode surface (see sub-sections 6.1.2 and 6.2.3) [I, II]. Ag catalysts prepared through hetero-polytungstate-assisted fabrication and deposition of AgNPs on reduced graphene oxide (rGO) substrates gave *n* values close to four as well [111].

To compare the intrinsic electrocatalytic activity of Ag-based catalysts, MA values for the ORR were calculated using Eq. 6. The mass-activities for O_2 reduction were calculated at -0.2 V vs. SCE using the dissolved Ag mass (Eq. 7) and kinetic current values at the given potential. From *Table 2 the* highest MA values were obtained for Ag/NGO catalysts. Ag/C1 possessed the lowest MA value (9 A g^{-1}), which was closely followed by Ag/C2 and Ag/MWCNT1 catalyst materials (for both MA = 10 A g^{-1}). This is likely related to large Ag particle sizes of these electrocatalysts, and in Figures 10 and 11, the Ag/NGO catalysts had overall the smallest particles with the most uniform distribution.

The higher MA of Ag/NGO catalysts may also be related to the synergistic effect between NGO and Ag-particles as some nitrogen groups make it easier for oxygen to adsorb, thus making the ORR more efficient [52]. Similar MA values have been reported, where the mass of Ag on the electrode surface was calculated from the Ag dissolution experiments [39].

Table 2. Kinetic parameters for oxygen reduction on electrodeposited Ag in 0.1 M KOH. ω = 1900 rpm. Mass of silver was obtained from Ag stripping data.

Catalyst	m (μg)	$E_{1/2}$ (V vs. SCE)	MA at -0.2 V vs. SCE (A g^{-1})
Ag/Gr1	10.92	-0.299	49
Ag/Gr2	7.06	-0.309	68
Ag/NGO1	7.46	-0.261	48
Ag/NGO2	3.35	-0.264	94
Ag/MWCNT1	12.96	-0.309	10
Ag/MWCNT2	3.43	-0.317	38
Ag/C1	16.42	-0.312	9
Ag/C2	8.53	-0.329	10

Durability of Ag-based catalysts is of utmost importance for their application as cathodes in AEMFCs. Figure 14 shows a comparison of the ORR polarization curves recorded during the stability test. From Figure 12 Ag/NGO1 has the most positive half-wave and onset potentials for the ORR, thus the stability test was conducted with the Ag/NGO1 catalyst and, for comparison, and Ag/C1 catalyst was used. For stability experiments, 1000 potential cycles between -1.3 and 0 V vs. SCE at a scan rate of 10 mV s^{-1} were carried out in O_2-saturated 0.1 M KOH solution. The $E_{1/2}$ value for Ag/NGO1 shifted negative only by 20 mV and for Ag/C1 only 22 mV and the diffusion-limited current density for both catalysts stayed almost unchanged, which shows high stability of the prepared catalysts.

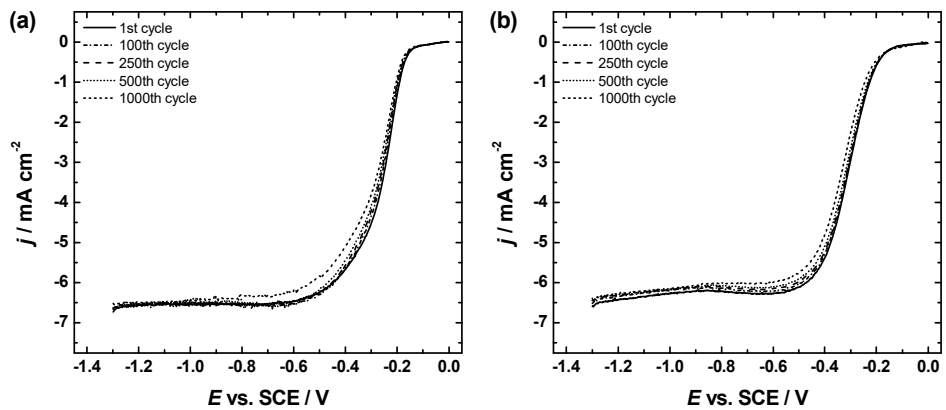

Figure 14. RDE polarization curves for oxygen reduction on (a) Ag/NGO1 and (b) Ag/C1 catalysts in O_2-saturated 0.1 M KOH during stability tests. ω = 1900 rpm, v = 10 mV s^{-1}.

6.3.3 H_2O_2 reduction on electrodeposited Ag on carbon supports

As Ag-based electrocatalysts can also be used as hydrogen peroxide detectors [114], then the hydrogen peroxide reduction measurements were carried out. The RDE polarisation data for peroxide reduction were further analysed using the K-L equation (Eq. 4), where the diffusion coefficient for HO_2^- anions is 1.36×10^{-5} cm^2 s^{-1} [62]. The *n* value is two for all measured Ag/NGO, Ag/C, Ag/Gr, and Ag/MWCNT catalysts. This shows that the electroreduction of hydrogen peroxide is efficient on all the Ag-based catalysts studied. It can be then reasoned that the Ag-catalyst materials prepared in this work catalyse the ORR through a 4-electron pathway, however it does not allow one to conclude that the ORR proceeds only via a direct $4e^-$ pathway. The assumption that the electroreduction of oxygen on the studied Ag-based catalysts proceeds simultaneously via 4-electron and 2+2 electron pathways is more realistic. A similar conclusion has been made in the previous part of the thesis (see sub-section 6.1.3) [I].

6.4 ORR on AgNPs supported on carbide-derived carbons

In the fourth part of the work AgNPs with a loading of 40 wt% were deposited onto two different carbide-derived carbon supports CDC1 and CDC2 [IV]. These CDC materials were purchased from Skeleton Technologies OÜ (Estonia). Both CDC samples were synthesised from titanium carbide powder (H.C. Starck, Ø<4μm) *via* high-temperature chlorination. For the CDC1 the additional physical activation with H_2O vapour at 900 °C was carried out [79]. Conventional Vulcan carbon was used for comparison. The purpose of this work was to evaluate the effect that microporous-mesoporous CDC supports have on AgNP size and Ag catalyst overall activity compared to conventional Vulcan carbon support. The reducing agent was $NaBH_4$ and based on the substrate used, the catalysts were named as Ag/CDC1, Ag/CDC2 and Ag/C.

6.4.1 Physical characterisation of the Ag/CDC materials

The N_2 adsorption analysis shows that both CDC materials, CDC1 and CDC2, are microporous, however, the CDC1 has significantly higher specific surface area (S_{BET} is 1997 m^2 g^{-1} and 1473 m^2 g^{-1}, respectively) and wider PSD due the physical post-activation. In Figure 15, both TiC-derived CDC materials have a dominating peak at ~0.85 nm in a microporous region of the PSD. In the case of CDC1, a second peak is also observed as a weak shoulder at ~1.5 nm. The total pore volume of CDC1 and CDC2 is 1.06 cm^3 g^{-1} and 0.75 cm^3 g^{-1}, respectively, from which approximately 80% derives from the micropores. The volume of pores smaller than 2 nm is 0.81 cm^3 g^{-1} and 0.60 cm^3 g^{-1} for CDC1 and CDC2, respectively.

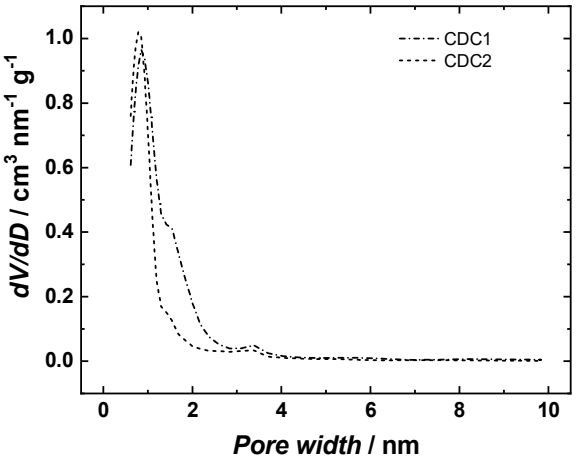

Figure 15. Pore size distribution of initial CDC materials.

Figure 16 shows SEM images of Ag/CDC catalysts. Both CDC materials are similar and have granular structure. Those grains are in general smaller than 1 μm. On these CDC materials the quasi-spherical AgNPs can be observed. $NaBH_4$ as the reducing agent yielded the average AgNP size of about 15 nm for both Ag/CDC catalysts and silver is uniformly distributed over the whole carbon support. It was rationalised by faster nucleation caused by a stronger reducing agent [115]. It has been also suggested that the presence of carbon support during the AgNPs synthesis influences the Ag particle size and their distribution [116, 117].

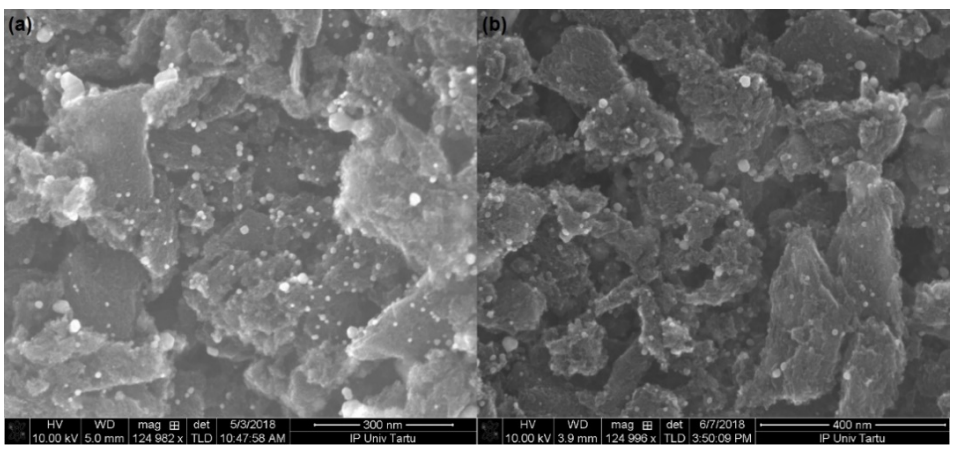

Figure 16. SEM micrographs of (a) Ag/CDC1 and (b) Ag/CDC2 samples.

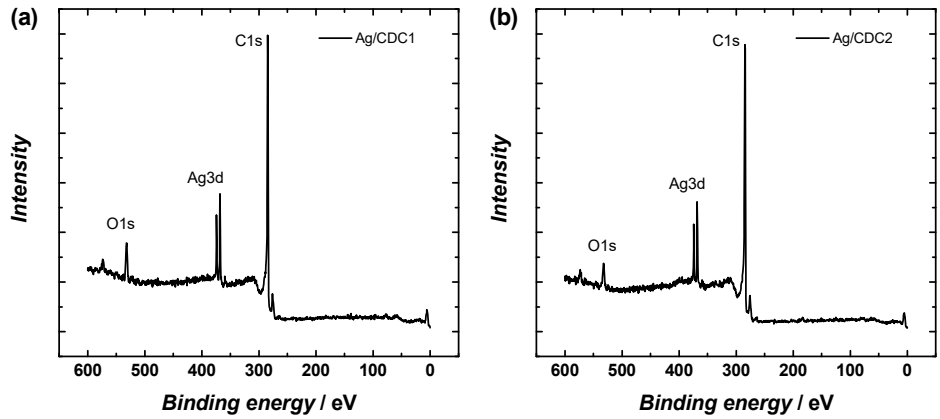

Figure 17. XPS survey spectra of (a) Ag/CDC1 and (b) Ag/CDC2.

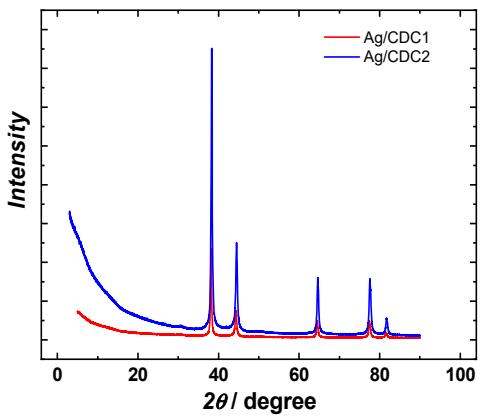

Figure 18. XRD patterns of Ag/CDC1 and Ag/CDC2 materials.

The EDS measurements of Ag/CDC catalysts showed no presence of Ti in the samples. In addition, the XPS analysis was carried out and the survey spectra are presented in Figure 17. Prominent C1s XPS peak is at 284.5 eV, Ag3d doublet is at 368 and 374 eV and O1s peak is at 532 eV. However, no Ti2p XPS signal at about 454 eV was detected, which confirms that all TiC has reacted during the preparation of the CDC materials. The XRD analysis showed only traces of the TiC for Ag/CDC samples (Figure 18). The peaks match with the standard (PDF 00.004.0783 Ag Silver-3C, syn). The lattice parameters were calculated for silver to be 4.0853 ± 0.0004 Å and 4.0856 ± 0.0009 Å for Ag/CDC1 and Ag/CDC2, respectively. The average crystallite size was 31.1 ± 0.1 nm for Ag/CDC1 and 33.6 ± 0.2 nm for Ag/CDC2. Figure 19 presents the results of the thermogravimetric analysis. Ag/CDC catalysts demonstrated different behaviour during the TGA experiments. The thermogravimetric

analysis showed that Ag/CDC1 retained 50% of initial mass and Ag/CDC2 had a metal loading of 30 wt%.

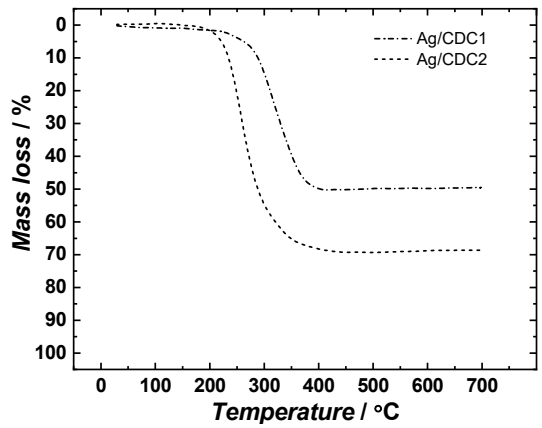

Figure 19. Thermogravimetric analysis of Ag/CDC samples.

6.4.2 ORR studies on the Ag/CDC materials

In Figure 20a, a comparison of RDE polarisation curves is presented. It can be observed that Ag-based catalysts prepared on the CDC supports show higher ORR activity than on Vulcan carbon in terms of more positive onset and half-wave potentials (see Table 3). Similarly, Ag/CDC materials $E_{1/2}$ values surpass that of bare CDC ones. The current minimum at diffusion-limited current plateaus originates partially from CDC materials themselves, as they are present on the ORR polarisation curves of both bare CDC and Ag/CDC materials. Although, the decrease in reduction current at about -0.7 to -1.0 V could partially come from Ag as it has been observed in previous parts of the thesis (see sub-sections 6.1.2 and 6.2.3) [I, II]. AgNPs supported on Vulcan carbon show a single minimum at about -0.8 V. This minimum on the polarisation curve of nanostructured Ag catalyst can be related to the specific crystallographic orientation of AgNPs that has different ORR performance [22]. The unmodified CDCs electrocatalytic activity surpasses that of bare GC electrode and Vulcan XC-72R carbon due to their higher specific surface area. Comparing carbon-supported Ag catalysts with bulk Ag electrode, it was observed that all three nanostructured Ag catalysts showed more positive onset and half-wave potentials.

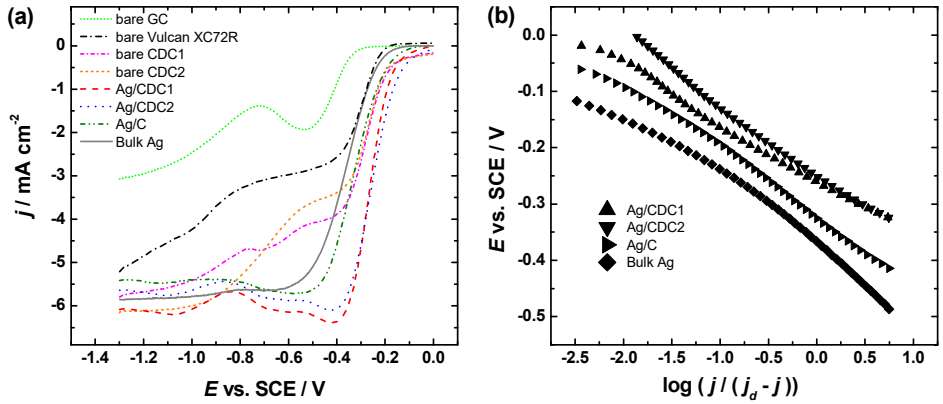

Figure 20. (a) Comparison of the ORR polarisation curves in O_2-saturated 0.1 M KOH at1900 rpm. v = 10 mV s^{-1}. (b) Mass-transfer corrected Tafel plots for ORR derived from (a).

To compare the catalysts, the mass activities for O_2 reduction (Table 3) were calculated using Eq. 6. The mass-activities were calculated at -0.2 V vs. SCE using the Ag loading from TGA results and kinetic current values at the given potential. The MA of Ag/C was the smallest 19 A g^{-1}. The mass activities of Ag/CDC1 and Ag/CDC2 were 47 and 57 A g^{-1}, respectively. The MAs were more than two times higher for Ag catalysts prepared on the CDC supports than on the Vulcan carbon. This agrees well with the previous findings in which Pt supported on the CDC had the same ORR activity with lower Pt loading than that on Vulcan carbon [118]. The same conclusion is then valid for different metal nanoparticles supported on the CDCs. As the difference in the ORR electrocatalytic activity between the two tested CDC materials was small, one would consider that the porosity of these two CDCs is sufficient for efficient O_2 diffusion. In addition, small variations in the particle size between the samples seem to influence the calculated mass activities. The ORR kinetics on the Ag-based catalysts was further analysed by constructing the Tafel plots (see Figure 20b) from which the slope values were determined (see Table 3). While Tafel slope value for bulk silver electrode was -80 mV, for nanostructured Ag/C, Ag/CDC1 and Ag/CDC2 catalysts the Tafel slope values were -101, -100 and -121 mV, respectively. A similar Tafel slope value as for bulk Ag has been previously reported for nanostructured Ag/MWCNT catalyst [45]. The change in the Tafel slope value has been attributed to the change in oxygen coverage, parallel reaction paths with different potential dependencies, change in the electrode surface that changes the reaction mechanism and also to the reaction steps that have different potential dependence [38]. The Tafel slope values in this study are in the same range as reported in the literature, thus we may conclude that the rate-determining step for the electroreduction of oxygen on Ag/CDC catalysts is the slow transfer of the first electron to the O_2 molecule.

Table 3. Kinetic parameters of the ORR on Ag-based catalysts in 0.1 M KOH. ω = 1900 rpm.

Catalyst	$E_{1/2}$ vs. SCE (V)	Tafel slope (mV)	MA at -0.2 V (A g^{-1})
Ag/CDC1	-0.29 ± 0.01	-100 ± 4	47 ± 3
Ag/CDC2	-0.30 ± 0.02	-121 ± 7	57 ± 2
Ag/C	-0.35 ± 0.02	-101 ± 12	19 ± 2
Bulk Ag	-0.37	-80	-

The RDE data on O_2 reduction were analysed using the K-L equation (Eq. 4) [119]. The *n* value was close to four, which suggests that the ORR followed a 4-electron pathway and almost no hydrogen peroxide formed. Bare CDC materials at low overpotentials follow a 2-electron pathway and at high overpotentials a 4-electron pathway, while the ORR on Ag/CDC materials proceeds predominantly via direct 4-electron pathway. Similar *n* values have been reported for various Ag catalysts like nanowires [37], nanocubes [112] and nanoparticles prepared by plasma jet treatment [42]. The *n* value close to 4 has also been reported for 40 wt% Ag/CNT catalyst [63, 81]. Ag catalyst where silver was electrodeposited onto carbon paper has also shown *n* values close to 4 [113]. When silver was electrodeposited onto the GC substrate, the *n* value depended on the deposition time. Longer deposition time yielded higher Ag mass on electrode, which in turn resulted in a higher *n* value (see sub-sections 6.1.2 and 6.2.3) [I, II]. The reports in which 10 wt% Ag/C was used where the *n* values were lower than four [29, 33, 35, 37, 39, 56, 63, 64, 120] suggest that the ORR proceeds partially on carbon support and the reaction proceeds via series $2e^- + 2e^-$ pathway. The series O_2 reduction pathway has been rationalized by Compton and co-workers [62]. They commented that with increasing the interparticle distance the generated peroxide amount increases. Thus, it is expected that the ORR on 40 wt% Ag/CDC catalysts proceeds at least partially via peroxide intermediate.

Stability tests were carried out with Ag/CDC2, and Ag/C catalysts and both tested materials proved to be stable by applying 1000 potential cycles during the ORR measurements (Figure 21). The diffusion-limited current density remained essentially the same, but the $E_{1/2}$ potential shifted only 20 mV for Ag/CDC2, while it shifted 30 mV for Ag/C catalyst. This demonstrates that Ag/CDC catalysts have superior mass-activity and better stability compared to Vulcan carbon supported AgNPs.

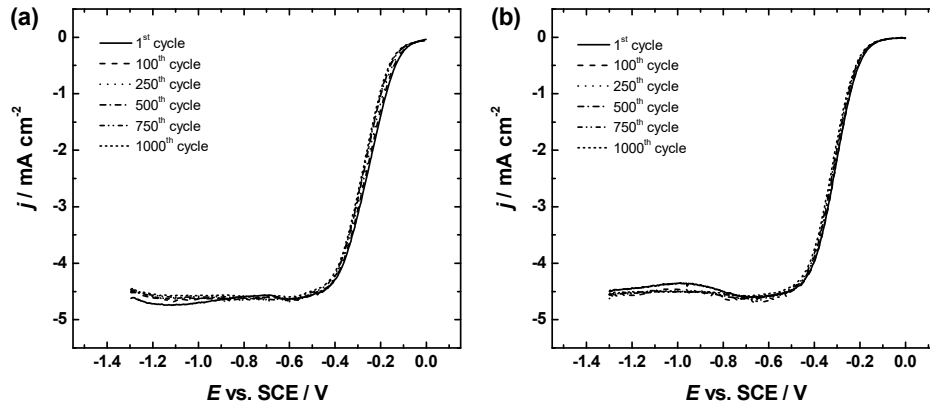

Figure 21. The ORR polarization curves on (a) Ag/CDC2 and (b) Ag/C catalysts during stability tests. ω = 960 rpm, v = 10 mV s^{-1}.

6.4.3 H_2O_2 reduction reaction on the Ag/CDC materials

It was of great interest to study these Ag/CDC catalysts for the hydrogen peroxide reduction. As with the O_2 reduction studies, the polarisation curves of the hydrogen peroxide reduction reaction also show a small current minimum at -0.8 V. This minimum originates from silver and CDC supports. The RDE polarisation data was analysed using the K-L equation (Eq. 4) in which 1.36×10^{-5} cm^2 s^{-1} was employed as the diffusion coefficient for HO_2^- anions [62]. The results of the K-L analysis give the value of n = 2 for both Ag/CDCs, showing that Ag/CDCs are efficient catalysts for peroxide electroreduction. This confirms that Ag/CDC1 catalyses the ORR through a 4-electron pathway. Both Ag/CDC2 and Ag/C catalysts yield similar results to that obtained for Ag/CDC1. However, this observation does not allow one to conclude whether the ORR proceeds via direct $4e^-$ pathway and thus it is more realistic to assume that the ORR may occur through parallel 4-electron and 2+2 electron pathways. A similar conclusion was made for AgNPs electrodeposited onto the GC substrate in the first part of this thesis (see sub-section 6.1.3) [I].

6.4.4 CV studies on the Ag/CDC materials

After oxygen reduction studies the Ag catalysts were further electrochemically tested using cycling voltammetry in the potential range from -1.2 to 0.4 V vs. SCE. In Figure 22 a comparison of the CV results is shown. In the potential region between -1.2 and 0 V no characteristic peaks can be observed. At about 0.1 V the oxidation of silver begins and for both Ag/CDC and Ag/C catalysts a characteristic anodic peak is observed. At 0.32 V a large oxidation peak consisting of two peaks can be seen. These CV peaks can be related to the formation of AgOH and Ag_2O phases [63, 102, 103]. The reduction of Ag surface oxides for Ag/CDC catalysts proceeds at cathodic scan at around 0.05 V, yet for Ag/C catalyst the reduction of Ag oxides starts a bit earlier at

about 0.02 V. According to the literature, the oxide reduction peak could be used to calculate the A_r of silver [66, 103]. As both Ag_2O and AgOH are formed during the oxidation of silver, for the A_r determination the reliability of this method might not be sufficient. In addition, Wiberg and co-workers advised that the oxide can be formed irreversibly. Instead of that, the Pb_{upd} method was suggested to be used for the determination of the A_r of Ag-based catalysts [95]. However, the use of Pb_{upd} as well as Cd_{upd} methods has been found not suitable for Ag particles under 50 nm [99]. In addition, the carbon support itself may affect the access of metal (Pb or Cd) ions to the silver particles thus complicating the determination of the true surface area. However, as the Ag/CDC and Ag/C catalysts are prepared by the same method, and based on the silver oxide reduction peaks, the Ag/CDC materials have a similar surface area, and thus the ORR results can be compared directly.

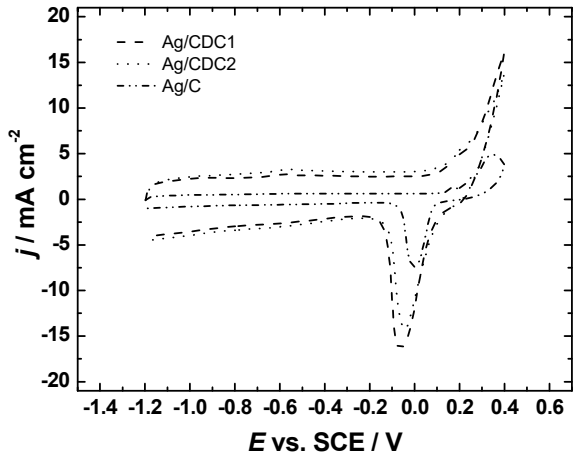

Figure 22. CVs of Ag-based catalysts in Ar-saturated 0.1 M KOH. $v = 50$ mV s^{-1}.

6.5 ORR on nitrogen-doped graphene oxide supported AgNPs

In the fifth part of the work AgNPs with a loading of 40 wt% were deposited onto nitrogen-doped graphene support [V]. The purpose of this work was to evaluate the effect nitrogen-doped graphene oxide (NGO) and synthesis methods have on the AgNPs size and distribution on the surface of the NGO, and improvement of Ag catalyst's overall electrocatalytic activity compared to the Ag free NGO. Three reducing agents $NaBH_4$, glycerol and ascorbic acid were used. The resulting catalysts were named as Ag/NGO3, Ag/NGO4 and Ag/NGO5, respectively.

6.5.1 SEM, TEM and XPS studies of the Ag/NGO materials

The electrocatalysts surface was initially characterised using scanning electron microscopy and representative SEM micrographs are presented in Figure 23. The surface morphology of the catalyst strongly depends on the preparation method. The Ag/NGO3 sample exhibited the best distribution of AgNPs, whereas Ag/NGO4 and Ag/NGO5 catalysts showed higher degree of agglomeration and in addition, ascorbic acid yielded the biggest Ag particles. The mean particle sizes were 7, 38 and 211 nm for Ag/NGO3, Ag/NGO4 and Ag/NGO5 catalysts, respectively. It should be noted that the particle size distribution is relatively wide for all Ag/NGO catalysts. The differences between the catalysts can be primarily attributed to the reduction strength of the reducing agent. $NaBH_4$ as the strongest reducing agent causes rapid nucleation of AgNPs and therefore yields the smallest nanoparticles, whereas the citrate aids the stabilisation of the nanoparticles [115]. Ascorbic acid is a weaker reducing agent [121] and produces larger nanoparticles that are more agglomerated. The reduction by glycerol also yields rather large, agglomerated AgNPs, but smaller than in Ag/NGO5, as glycerol also stabilises AgNPs and prevents their further ripening [115]. Guo and co-workers prepared AgNPs using $NaBH_4$ as a reducing agent and supported these particles on Vulcan XC-72R showing similar particle size and good AgNP distribution [63]. They proposed two steps that influence the particle size distribution: the first is the synthesis of the particles and the second is their anchoring to the carbon support. It was found that the size of AgNPs does not change significantly during the anchoring. Similarly, to the fourth part of this thesis, $AgNO_3$ was first added to the suspended NGO solution and then AgNPs were synthesised (see sub-section 5.1.4) [IV]. Thus, the presence of NGO may play a significant role in determining the size of Ag particles and influence AgNPs distribution on its surface.

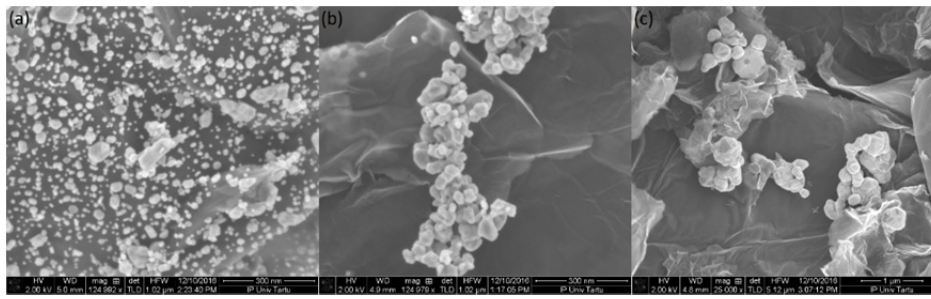

Figure 23. SEM images of (a) Ag/NGO3, (b) Ag/NGO4 and (c) Ag/NGO5 samples.

The structure and composition of sample Ag/NGO3 was further studied with STEM. The high-angle annular dark-field (HAADF-STEM) image in Figure 24a shows light AgNPs on the darker background of NGO. The energy dispersive X-ray spectroscopy mapping of Ag K_α and N K_α characteristic X-rays in Figure 24b and 24c, respectively, affirm the distribution of the AgNPs and show that the whole surface of graphene is uniformly doped with nitrogen. On the AgNPs the background X-ray intensity is somewhat higher than on GO.

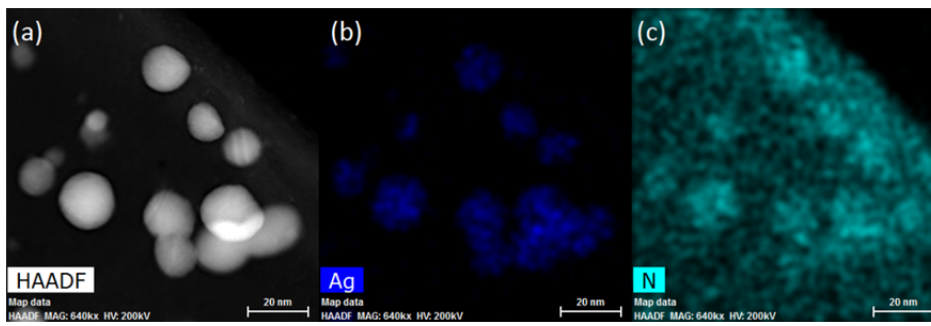

Figure 24. HAADF-TEM image and EDS mapping of silver and nitrogen of Ag/NG3 sample.

The surface elemental composition of all the prepared catalysts was characterised by XPS (Figure 25). As expected, the XPS peaks for C, N, Ag and O were all present. C1s is located at 284 eV, N1s at 400 eV, O1s at 531 eV and doublet of Ag3d at 368 and 374 eV. The nitrogen-to-carbon atomic ratio was about 0.07. The Ag-to-C ratio decreased in the order of Ag/NGO3 > Ag/NGO4 > Ag/NGO5 possibly because of the agglomeration of Ag. The high-resolution XPS spectra in the N1s region resemble those observed in previous works on N-doped carbon nanomaterials [50, 52, 53]. The highest XPS peak at 398 eV indicates that N is largely in pyridinic configuration, which has been suggested to be one of the most active centres for the ORR [122]. Zhou and co-workers have suggested based on the N1s XPS spectra that nitrogen is bound to silver as

they observed a shift in the binding energy, however they did not comment about the Ag3d peaks [54]. In a later study [52] and in this part of the thesis the location of Ag3d peaks suggest that silver is in metallic form (a zero-valent state).

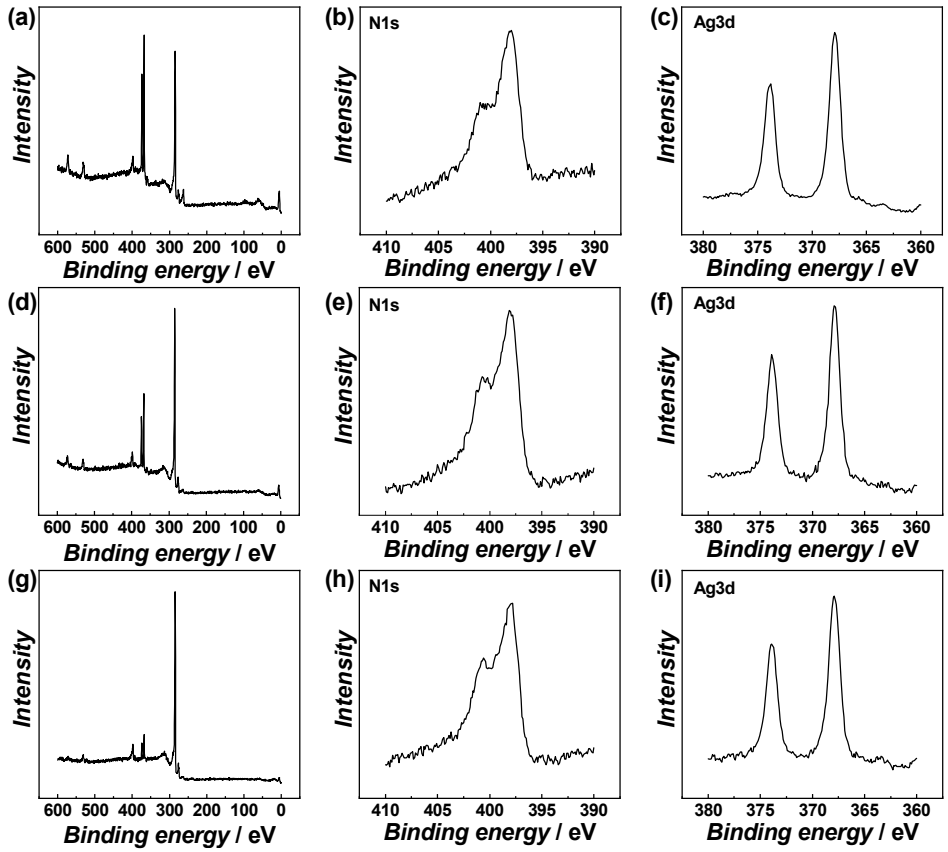

Figure 25. XPS survey spectra with detailed XPS spectra in the Ag3d and N1s regions (a-c) of the Ag/NGO3, (d-f) of the Ag/NGO4 and (g-i) of the Ag/NGO5 catalyst.

6.5.2 ORR studies on Ag/NGO catalysts

For all three Ag/NGO catalysts, clean NGO, and for bulk polycrystalline silver single-wave ORR polarisation curves were observed (Figure 26a). The highest ORR activity was obtained with the AgNPs prepared using glycerol as a reducing agent, whereas AgNPs prepared by sodium borohydride and ascorbic acid possess very similar activity. Bulk Ag electrode and metal-free nitrogen-doped graphene oxide showed similar ORR onset potential. Based on the RDE data (Figure 26a) the Tafel analysis was carried out (Figure 26b). It can be observed that the Tafel plots of Ag/NGO and bulk Ag electrode are almost parallel to each other, and the corresponding slope value is about -80 mV at low current densities, gradually increasing to about -170 mV at high current densities, while on N-doped graphene the Tafel slope is about -55 mV. Similar slope values for Ag catalysts have been obtained in several studies [15, 65, 123]. Wiberg and co-workers reported the slope value of -90 mV for poly-crystalline bulk silver and -120 mV for AgNPs with the particle size of 100 nm [95, 96]. The changing Tafel slope value has been explained by the change in the surface coverage of adsorbed species and strong lateral repulsion between adsorbed OH and reaction intermediates [22]. However, the slope value of -43 mV has been found for AgNPs supported on N-doped rGO, which is close to that of nitrogen doped reduced graphene, suggesting that the ORR in this particular case proceeds also on the substrate surface or it is due to the inter-actions between nitrogen and Ag particles [54]. Thus, it may be assumed that the ORR on Ag/NGO catalysts in this study proceeds mainly on silver nano-particles.

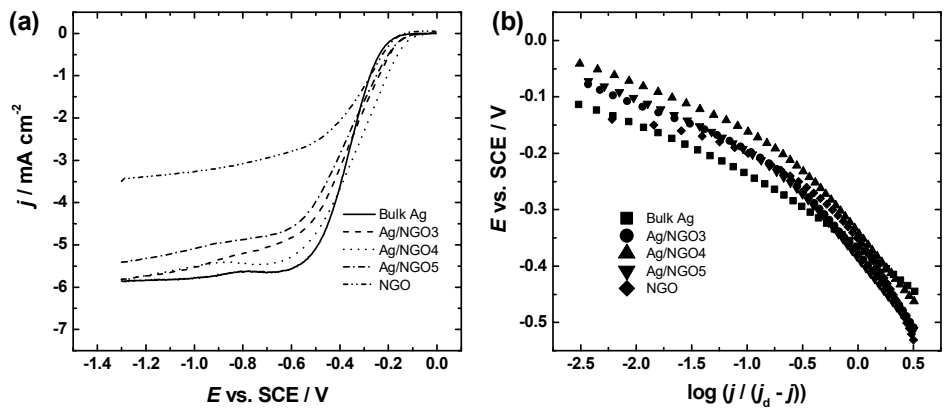

Figure 26. (a) Comparison of the RDE polarisation curves for ORR on Ag/NGO1, Ag/NGO2, Ag/NGO5, NGO and bulk Ag electrodes. (b) Tafel plots for ORR derived from (a). Test solution: O_2-saturated 0.1 M KOH. ω = 1900 rpm, v = 10 mV s^{-1}.

For further analysis, the RDE measurements at various electrode rotation rates were conducted and the RDE data on O_2 reduction was analysed by the K-L equation (Eq. 4). The value of *n* was calculated, which was close to four for all Ag/NGO catalysts and for bulk Ag in the whole range of potentials studied, showing that the ORR yields water as the final product. For the NGO material, the *n* value was about 3, which indicates that only a part of the hydrogen peroxide produced during the ORR process was further reduced. It is evident that AgNPs enhance the ORR kinetics at low overpotentials. The chemicals used in the synthesis of AgNPs may affect the ORR activity if these remain on the catalyst surface. For instance, Ag nanorods protected by PVP show lower current density and 2-electron ORR pathway, whereas Ag nanorods that do not have PVP on the surface catalyse a complete 4-electron reduction of O_2 [100]. The *n* values obtained in this work surpass that reported in the literature for Ag catalyst on N-doped graphene [110], which suggests that the ORR on Ag/NGO is not inhibited by the residues of the chemicals used in the synthesis of AgNPs. Low yield of peroxide has been reported several times, for instance on silver nanowires [37], Ag nanocubes [112] and very recently for AgNPs prepared by plasma jet treatment [42].

The mass-activities for O_2 reduction were calculated at -0.2 V vs. SCE using the mass of the catalyst on the electrode (Eq. 7) and kinetic current density values at the given potential (see Eq. 6). The MA values decreased in the following order: Ag/NGO4 (7.6 A g^{-1}) > Ag/NGO3 (4.1 A g^{-1}) > Ag/NGO5 (3.7 A g^{-1}) > NGO (2.2 A g^{-1}). This series demonstrates that silver enhances the mass activity of the catalyst. This may be related to the synergistic effect between nitrogen-doped graphene oxide and AgNPs, as it has been suggested that some nitrogen groups enhance the adsorption of oxygen so that it can be easily reduced [52]. It is rather interesting to note that Ag/NGO3, which has the best AgNP distribution, does not show the highest mass activity. There is a possibility that some citrate that was used in the nanoparticle synthesis is still capping AgNPs, however in this case the *n* value should be also affected.

The catalyst showing the best O_2 reduction activity (Ag/NGO4) was further tested using the RRDE system (Figure 27), to determine the peroxide yield (Φ), which was calculated using Eq. 8. The peroxide yield remained under 10% over the whole range of potentials studied. In addition, the number of electrons transferred per O_2 molecule was also calculated using Eq. 9. The *n* value coincided with the one calculated from the RDE data using the K-L equation (Eq. 4). These results suggest that Ag/NGO catalysts prepared in the fifth part of the thesis catalyse the ORR mainly via a 4-electron pathway.

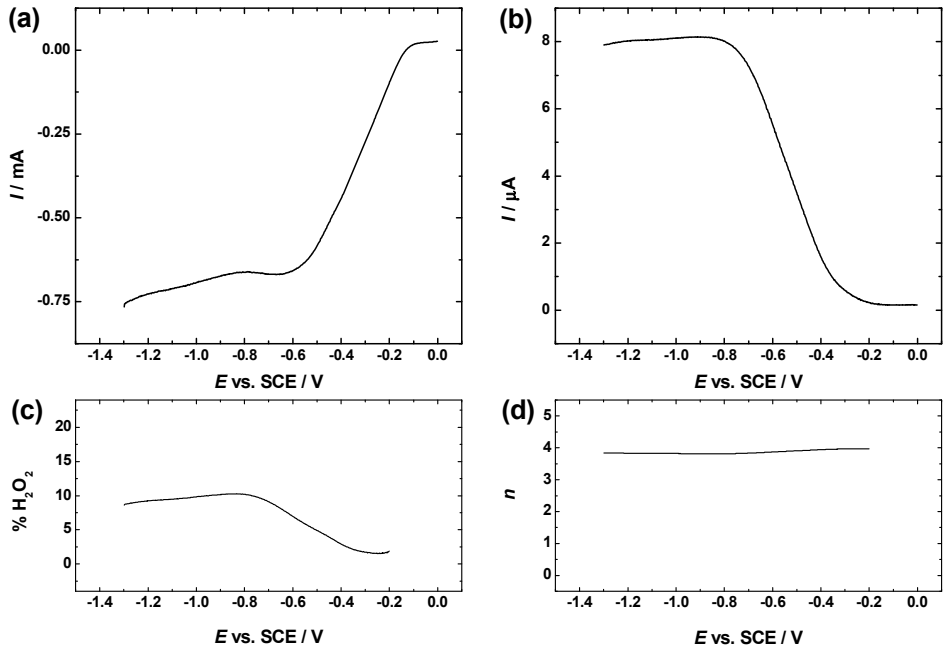

Figure 27. RRDE results for ORR on Ag/NGO4 in O_2-saturated 0.1 M KOH: (a) disk current, (b) ring current, (c) peroxide yield and (d) dependence of *n vs. E*. ω = 960 rpm, v = 10 mV s^{-1}.

Ag/NGO4 was further used to study the electroreduction of hydrogen peroxide. As expected, Ag/NGO4 catalysed the reduction of HO_2^- and according to the K-L analysis the *n* value was close to 2. This suggests that HO_2^- generated at NGO substrate during O_2 reduction is further reduced on AgNPs.

6.6 AgNPs on mesoporous ECS as cathode catalyst for AEMFC

In the sixth part of the work, AgNPs with a nominal loading of 40 wt% were deposited onto two nitrogen-containing mesoporous carbon supports using a citrate method [VI]. As provided by the producer the specific surface areas of the engineered catalyst supports (ECS) were 820 m^2 g^{-1} for ECS-004601 and 730 m^2 g^{-1} for ECS-004201. The ECS-004601 material possesses higher quantities of larger well-defined and uniform bimodal mesopores (15-50 nm) than ECS-004201 material (7-25 nm). Conventional Vulcan carbon (VC) support was used for comparison. The purpose of this work was to evaluate whether adding silver enhances the activity of two already active mesoporous and N-containing support materials for fuel cells and how do these supports affect AgNP size and distribution compared to the conventional VC support. Reducing

agents $NaBH_4$ and hydrazine hydrate were used for AgNPs synthesis. The resulting catalysts were named as Ag/4601_BH4, Ag/4201_BH4, Ag/C_ BH4, Ag/4601_HH, Ag/4201_HH and Ag/C_HH, respectively, where BH4 means $NaBH_4$ and HH means hydrazine hydrate. Two most active catalysts Ag/4201_HH and Ag/4601_BH4 were tested in AEMFC.

6.6.1 Physical characterisation of the Ag catalysts on ECS

As shown in Figure 28, the mesoporous carbon-supported Ag catalysts possess a similar sponge-like structure and homogenously distributed quasi-spherical AgNPs. The average Ag nanoparticle size was 31 nm for Ag/4201_HH and 26 nm for Ag/4201_BH4. For Ag/4601_HH and for Ag/4601_BH4 it was 29 nm and 22 nm, respectively. Lastly, for Ag/VC_HH it was 28 nm and for Ag/VC_ BH4 20 nm. These AgNP sizes are as expected when compared to synthesis procedures used in fourth and fifth part of this thesis (see sub-sections 5.1.4, 5.1.5, 6.4.1 and 6.5.1) [IV, V], where the $NaBH_4$ was used. Ag nanoparticles (~ 20 nm), obtained using hydrazine hydrate as a reducing agent, have also been reported, and faster nucleation was brought as the reason for it [83].

According to the EDS analysis, the Ag loading in the catalyst is around 37 wt% for Ag/4201_HH, 34 wt% for Ag/4201_BH4, 41 wt% for Ag/4601_HH, 39 wt% for Ag/4601_BH4 and 41 wt% for both Ag/VC_HH and Ag/VC_BH4. This confirms the planned 40 wt% Ag loading in the synthesized catalyst materials.

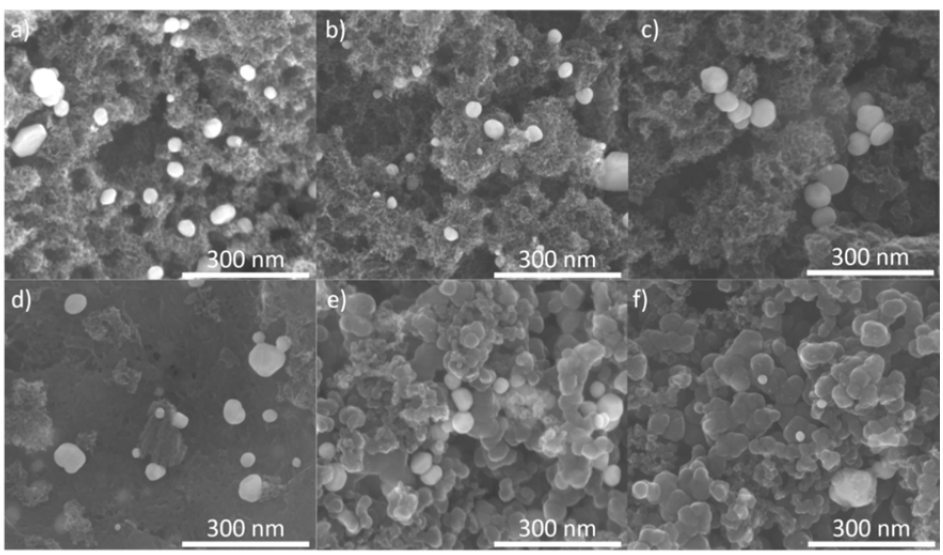

Figure 28. SEM micrographs of (a) Ag/4201_HH, (b) Ag/4201_BH4, (c) Ag/4601_HH, (d) Ag/4601_BH4, (e) Ag/VC_HH, and (f) Ag/VC_BH4 samples.

Figures 29a-d present XPS survey spectra for the Ag-based catalysts prepared using the ECS supports, where the insets show corresponding Ag3d and N1s spectra. The N1s XPS peak was expected, as these support materials are all nitrogen-doped. The C1s XPS peak is at 284 eV, doublet of Ag3d at 368 and 374 eV, N1s peak at 401 eV and O1s peak at 531 eV. The Ag-to-C atomic ratio for Ag/4201_HH was around 0.04, for Ag/4201_BH4 was around 0.06, for Ag/4601_HH was around 0.03 and around 0.04 for Ag/4601_BH4. The N-to-C atomic ratio for all catalysts was around 0.02. In all the samples, nitrogen is mainly in graphitic-N (blue line), pyridinic-N (red line), and pyrrolic-N (green line) configurations (see insets to Figure 29), which are confirmed by N1s peaks at ~402, ~398 and ~401 eV, respectively [124, 125]. Graphitic N species have been considered one of the more active N-species for the ORR in alkaline media [122, 126]. According to Zhou and Qiao, based on the high-resolution XPS spectra in the N1s region, Ag may be bound to N centres because a shift in the binding energy was observed [54].

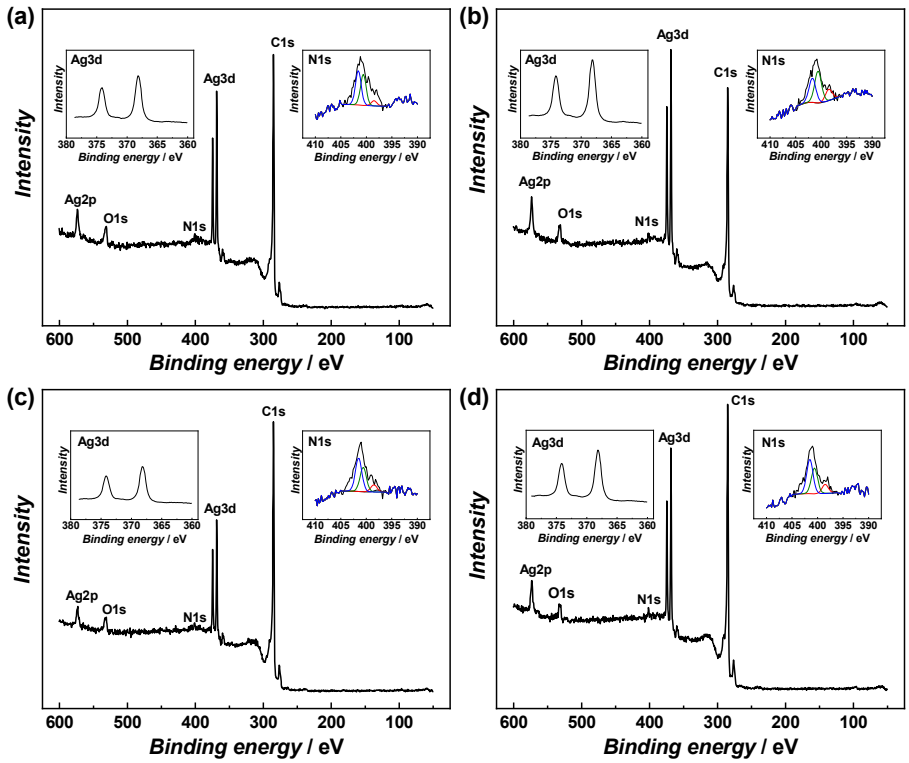

Figure 29. XPS survey spectra of (a) Ag/4201_HH, (b) Ag/4201_BH4, (c) Ag/4601_HH, and (d) Ag/4601_BH4 samples, insets show detailed XPS spectra in the Ag3d and N1s regions.

The XRD patterns for the Ag-based catalysts shown in Figure 30 match the Ag standard (PDF 01-089-3722 Ag Silver, syn). Ag crystallite sizes, estimated from the full width at half maximum of the XRD peaks using the Scherrer's equation ranged between 19 and 28 nm.

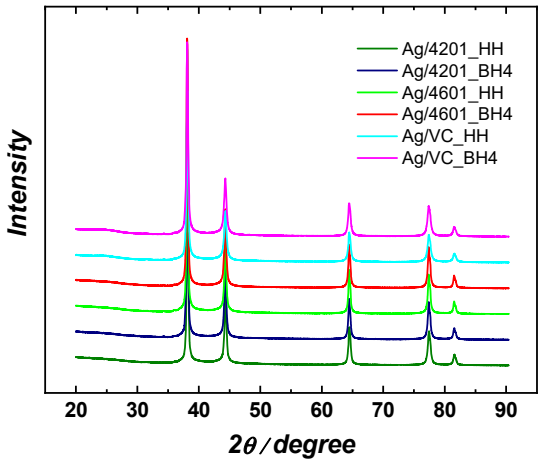

Figure 30. XRD patterns of Ag/4201_HH, Ag/4201_BH4, Ag/4601_HH, Ag/4601_BH4, Ag/VC_HH, and Ag/VC_BH4 samples.

According to the TGA results shown in Figure 31, the Ag loading in the synthesised catalyst materials was 39 wt% for Ag/4201_HH, 40 wt% for Ag/4201_BH4, 31 wt% for Ag/4601_HH and 39 wt% for Ag/4601_BH4, which confirms the synthesis of 40 wt% Ag-based catalysts.

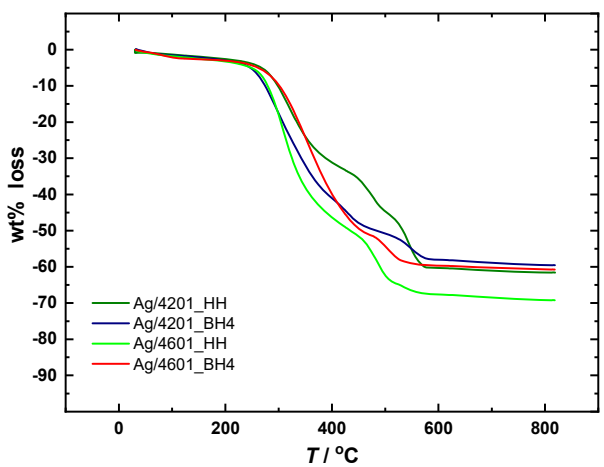

Figure 31. Thermogravimetric analysis of Ag-based catalysts.

6.6.2 ORR studies on the Ag catalysts prepared on ECS

Figure 32a demonstrates higher ORR performance of the Ag catalysts deposited on the ECS materials compared to that on Vulcan XC-72R support. Although, as shown in Table 4, the ECS supported Ag catalysts show more positive half-wave and onset potentials than the Vulcan supported catalysts, they are still less active compared to the commercial 20 wt% Pt/C. All the carbon-supported Ag electrocatalysts show higher $E_{1/2}$ values than a bulk Ag electrode.

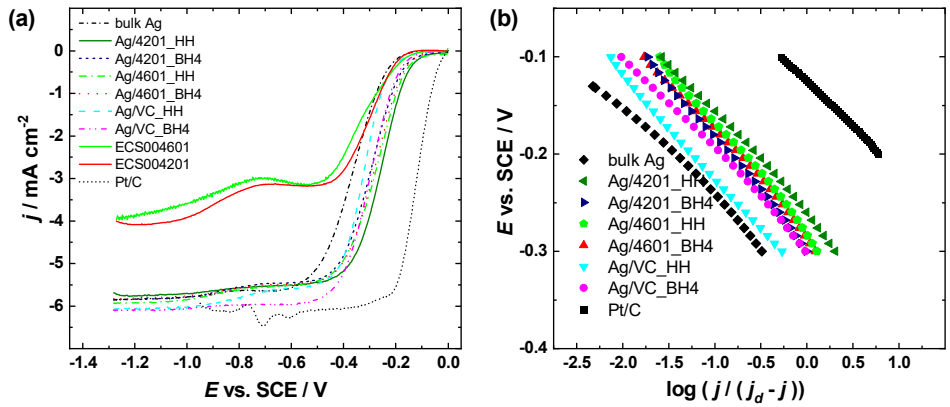

Figure 32. (a) Comparison of the ORR polarisation curves in O_2-saturated 0.1 M KOH at 1900 rpm. v = 10 mV s^{-1}. (b) Mass-transfer corrected Tafel plots for ORR (data derived from (a)).

Table 4. Kinetic parameters for ORR on Ag-based catalysts in 0.1 M KOH. ω = 1900 rpm.

Catalyst	$E_{1/2}$ vs. SCE (V)	Tafel slope (mV)	MA at -0.2 V (A g^{-1})	n
Ag/4201_HH	-0.29 ± 0.02	-97 ± 8	38 ± 5	3.9 ± 0.06
Ag/4201_BH4	-0.32 ± 0.01	-107 ± 7	28 ± 6	4.0 ± 0.03
Ag/4601_HH	-0.30 ± 0.02	-104 ± 10	28 ± 2	4.0 ± 0.05
Ag/4601_BH4	-0.30 ± 0.01	-97 ± 4	32 ± 0.1	3.9 ± 0.07
Ag/VC_HH	-0.33 ± 0.02	-99 ± 6	7 ± 0.3	4.0 ± 0.03
Ag/VC_BH4	-0.31 ± 0.01	-94 ± 21	10 ± 0.4	4.0 ± 0.06
Bulk Ag	-0.37	-80	n.a.	3.9 ± 0.09
Pt/C	-0.14	-67	83*	4.0 ± 0.03

*The calculated mass of the Pt from commercial 20 wt% was used to obtain the MA value.

The mass-activities for O_2 reduction (Eq. 6) were calculated at -0.2 V vs. SCE using the dissolved Ag mass (Eq. 7) and kinetic current values at the given potential. All the Ag catalysts supported on ECS materials possess similar mass activities (see Table 4). Ag/4201_HH had the highest MA of 38 A g^{-1}, closely followed by Ag/4601_BH4 with 32 A g^{-1}, Ag/4601_HH (28 A g^{-1}) and

Ag/4201_BH4 (28 A g^{-1}). The MA values for Ag/VC_BH4 and Ag/VC_HH catalysts were 10 and 7 A g^{-1}, respectively. It is worth noting that the MA values are nominally higher than that for the Ag-based catalysts with N-doped graphene substrate material, however, in that case, the MA values were normalised to the whole catalyst, not just the mass of Ag (see section 6.5.2) [V]. Since the mesoporous carbon substrate materials used in this work also contain multiple N species, the increase in the MA values might be due to the synergistic effect between the nitrogen atoms in the carbon structure and the Ag particles. Similar to those reported in the literature, the main N species in the Ag-based catalysts are the graphitic-N, pyridinic-N and pyrrolic-N, which are the more active ones because they facilitate O_2 adsorption to the surface of the Ag-containing catalyst, leading to more efficient O_2 reduction [52, 54, 110, 122, 126, 127]. Zhou and Qiao studied the Ag/rGO catalyst, where Ag was deposited onto rGO and Ag/N-rGO where Ag was deposited onto N-doped rGO and found that the Ag/N-rGO catalyst showed higher ORR activity due to the synergistic effects between the Ag and N species [54]. Ji and co-workers. studied silver nanowires (AgNWs) wrapped in the N-doped graphene (NG) and reported that due to the synergistic effect between the one-dimensional AgNWs and two-dimensional NG, the catalyst showed far better ORR activity than AgNWs and NG alone [127]. Lai and co-workers have suggested that the graphitic N species have a more significant effect on the current densities while the pyridinic N species increase the onset potential for the N-doped carbon support [126]. These observations support the fact that the nitrogen doping of the nanocarbon materials does influence the ORR performance. In addition, the mass activities are also influenced by the Ag particle sizes [35, 37]. Similar electrocatalytic ORR activity for all Ag catalysts supported on the ECS materials shows that the porosity of both used mesoporous carbon supports is sufficient for efficient oxygen diffusion.

Tafel slope values for various Ag-based catalysts calculated from Figure 32b using the RDE data are shown in Table 4. The slope values for carbon-supported Ag catalysts range between -94 and -107 mV and that of the bulk Ag electrode is -80 mV. These Tafel slope values are similar to those presented in the literature and previous parts of this PhD thesis (see sub-sections 6.1.2, 6.2.3, and 6.4.2) [I, II, IV] [45, 110]. As reported by Šepa and co-workers, the range of the Tafel slope could be attributed to potential dependence of the reaction steps and changes in the reaction mechanism caused by variation in the electrode surface structure and oxygen coverage [38]. It is believed that the AgNPs are the active sites based on the higher Tafel slope and more positive $E_{1/2}$ values (see Figures 32a and 32b), and the ORR rate is limited by a sluggish transfer of the first electron to the O_2 molecule [111].

The RDE data was further analysed using the K-L equation (Eq. 4). The *n* values determined using the K-L plots are about four for all the catalysts, suggesting that the ORR follows a four-electron pathway, with a minimum hydrogen peroxide formation. For comparison, the bare ECS materials had *n* value that was close to three, which shows that although the ECS supports could

be used as catalysts by themselves, the addition of AgNPs improves the activity of the catalyst [128]. The 4-electron ORR pathway has also been reported for other Ag catalysts [104, 105, 108, 129-132], for example, Ag nanocubes [112], AgNPs prepared by plasma jet treatment [42], and Ag nanowires [37]. Fazil, Chetty, and Guo and co-workers have reported *n* values close to 4 for 40 wt% Ag/CNT catalysts for the ORR [63, 81]. A four-electron ORR pathway has also been reported for Ag catalysts electrodeposited onto carbon paper [113]. The previous reports suggest that 10 wt% Ag/C catalysts are not suitable to catalyse the ORR via a four-electron pathway as their *n* values are lower than 4 [61, 63, 64]. The reaction could follow a series of 2+2 electron pathway rather than the direct four-electron pathway [1, 29, 33, 35, 37, 39, 56, 63, 64, 120]. Considering these explanations, it might mean that the ORR on 40 wt% Ag-based catalysts synthesised in this part of the thesis could still partially proceed through a series 2+2 electron pathway producing some intermediate hydrogen peroxide.

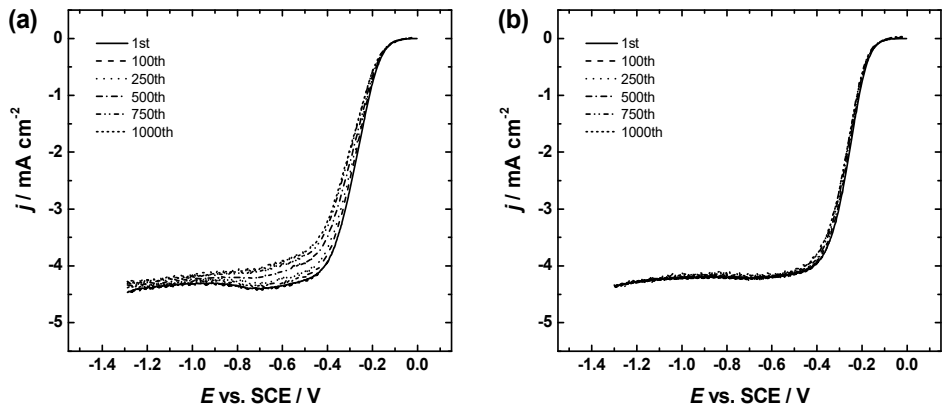

Figure 33. RDE polarisation curves for oxygen reduction on Ag/4601_BH4 and Ag/4201_HH catalysts in O_2-saturated 0.1 M KOH during the stability tests. ω = 960 rpm, v = 10 mV s^{-1}.

1000 potential cycles were applied to test the stability of Ag-based catalysts used in the fuel cell studies (see Figure 33). For Ag/4601_BH4 catalyst, the $E_{1/2}$ value shifted by 30 mV and for the Ag/4201_HH 36 mV. The change in the diffusion-limited current density was unsubstantial. Both of the catalysts tested here have similar drop in the half-wave potential as in a previous part of the thesis, where carbide-derived carbon-supported AgNPs were tested (see sub-section 6.4.2) [IV], and are comparable to unsupported AgNPs [42]. Recently, AgNPs were electrochemically deposited onto carbon powder and the resulting catalyst showed 20 mV drop in the $E_{1/2}$ value during the stability test [133]. It has been shown that in alkaline fuel cell the degradation rate is 20 μV h^{-1}; 5000 h stability test resulted in potential change of 100 mV from which 12–15% was suggested to be related to the cathode [134]. This was said to be sufficient for mobile applications, but not for stationary ones.

6.6.3 CV studies on the Ag catalysts prepared on ECS

The CV measurements were carried out between -1.2 and 0.4 V, after the ORR experiments, and the results are shown in Figure 34. No oxidation peaks can be observed in the potential region starting from -1.2 V and moving up to 0 V. From 0.1 V, the surface oxidation of Ag starts, and characteristic anodic peaks appear. At a potential of 0.35 V, two peaks, AgOH and Ag_2O and a third peak representing both, are formed and can be observed for all catalysts [63, 102, 103]. On the way back, in the cathodic direction, at -0.01 V one can observe the oxide reduction peaks for Ag/4601_BH4 and Ag/4601_HH catalysts, at -0.03 V for Ag/4201_BH4 and Ag/4201_HH and -0.05 V for Ag/VC_BH4 and Ag/VC_HH. Interestingly, the oxide reduction peak depends more on the catalyst support than on the synthesis method. When comparing the catalysts synthesised using $NaBH_4$ to hydrazine hydrate as the reducing agents, the synthesis procedure for all the catalysts was very similar, and the difference between the oxide reduction peaks was slight.

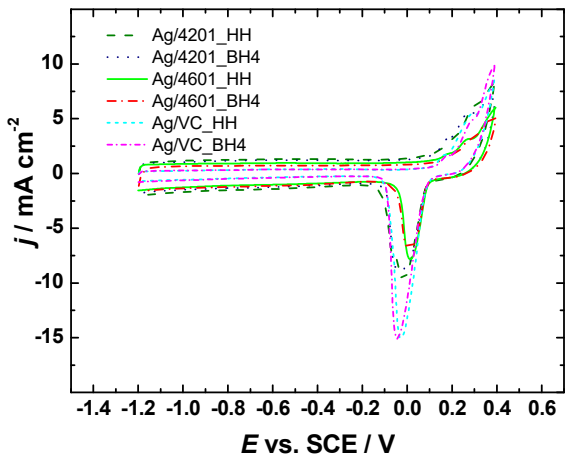

Figure 34. CVs of Ag-based catalysts in Ar-saturated 0.1 M KOH, $v = 50$ mV s^{-1}.

6.6.4 Ag stripping studies of Ag catalysts on ECS

To measure the amount of Ag present on the GC electrode, the Ag stripping experiment was conducted in 0.1 M $NaClO_4$ solution, and a comparison of the cyclic voltammograms is presented in Figure 35. A single Ag stripping peak is observed for all catalysts. The anodic stripping current starts to increase from ca. 0.3 V, and the peak values depend on the amount of Ag present on the GC electrode. Moving in the cathodic direction, one can observe a small shoulder between 0.3 and 0.2 V, representing a slight Ag re-deposition onto the GC electrode. The amount of dissolved Ag was calculated by charge integration under the CV peaks (in Figure 35) using Eq. 7. The calculated Ag masses on the

electrode were 8.82 (this equals to 29.4 wt% of Ag in catalyst), 8.61 (28.7 wt%), 9.39 (31.3 wt%), 7.27 (24.2 wt%), 9.95 (33.2 wt%) and 11.7 µg (39.0 wt%) for Ag/4201_HH, Ag/4201_BH4, Ag/4601_HH, Ag/4601_BH4, Ag/VC_HH and Ag/VC_BH4, respectively.

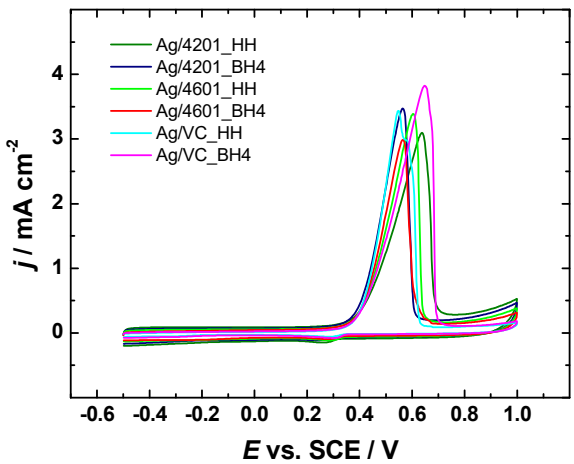

Figure 35. A comparison of dissolution of Ag-based catalysts in Ar-saturated 0.1 M $NaClO_4$ solution, v = 10 mV s^{-1}.

6.6.5 AEMFC studies of Ag on mesoporous carbons

The catalysts, Ag/4601_BH4 and Ag/4201_HH with the highest ORR activity (see Table 4) were evaluated as cathode materials in an AEMFC along with Pt-Ru/C anode catalyst using Aemion+ (10 µm) anion exchange membrane. Figure 36 shows the fuel cell performance for the Ag-based catalysts, with Pt/C cathode catalyst for comparison, using H_2 and O_2 gases at 65 °C and 65% RH conditions. Evidently, the P_{max} value is about 90% for the AEMFC with Ag/4601_BH4 (P_{max} = 310 mW cm^{-2}) compared to that of Pt/C cathode (P_{max} = 347 mW cm^{-2}) and the Ag/4201_HH showed the P_{max} value of 243 mW cm^{-2}. The slightly lower AEMFC performance for Ag-based catalysts compared to Pt/C could be attributed to the unoptimised thickness of the cathode catalyst layer and the issues associated with water management at high current densities [135]. In addition, the P_{max} value exhibited by Ag/4601_BH4 is similar to that reported in the literature for Ag/carbon black (Ag/CB, ~330 mW cm^{-2}) by Truong and co-workers [136]. The difference in P_{max} between the Ag-based catalysts could be due to the pore size distribution of the commercial mesoporous carbon support of the cathode catalyst, which can affect the overall catalyst morphology, including Ag particle sizes and their distribution. In addition, the suitability and successful integration of the ionomer and the AEM with the specific catalyst material is an important property that can significantly influence the AEMFC performance [137, 138]. Table 5 compares the fuel cell performance of various Ag-based catalysts from

the literature with the present study. It is worth noting that the AEMFC performance reported in the literature is significantly different due to variation in the operating conditions, GDLs, ionomers, AEMs, anode catalysts and so on [139–144].

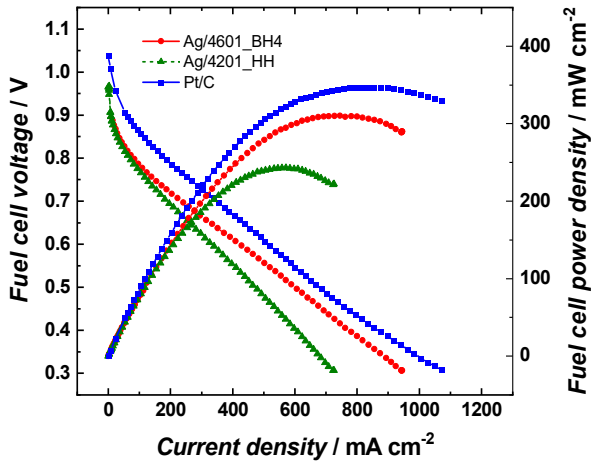

Figure 36. AEMFC performance with Ag/4601_BH4, Ag/4201_HH and Pt/C (0.4 mg_{Pt} cm^{-2}) cathode and Pt-Ru/C anode catalysts with Aemion+ anion exchange membrane at 65 °C using H_2 and O_2 gases at 200 kPa.

Table 5. Comparison of AEMFC performance using Ag-based cathode catalysts.

Cathode catalyst	Anode loading (mg cm^{-2})	Cathode Ag loading (mg cm^{-2})	Membrane	T (°C)	P_{max} (mW cm^{-2})	Ref.
Ag/4601_BH4	0.8 (Pt-Ru)	0.8 (40 wt%)	Aemion+ (10 μm)	65	310	This work
Ag/4201_HH	0.8 (Pt-Ru)	0.8 (40 wt%)	Aemion+ (10 μm)	65	243	This work
Ag/CB	0.8	0.6 (60 wt%)	AT-1	70	329.6	[136]
AgNWs	0.5 (Pt)	1.05	Tokuyama A901	60	164.4	[145]
VAgNs/SAgNs	1.25	1.2	FAA-3	60	115.6	[146]
Ag/C	0.2 (Pt)	1.0 (40 wt%)	Tokuyama A201	80	190	[147]
Ag/C	0.5	0.3 (60 wt%)	AHA-Neosepta	30	10	[66]
Ag/C	0.5 (Pt)	4 (Ag)	AAEM	50	90	[148]
Ag/CNT	0.5	0.2 (40 wt%)	FAA	r.t.	26.1	[81]
Ag/C	0.375	0.05 (10 wt%)	APSEBS	60	109	[120]
Ag_{NPs}@Fe_{NPs}-N-C	0.4 (Pt-Ru)	n.a.	PAP-TP-85	80	506	[149]

6.7 Ag/MnO_2_MWCNT composites as electrocatalysts for ORR

In the seventh part of the work, two different MnO_2_MWCNT support materials were prepared (MnO_2_MWCNT1 and MnO_2_MWCNT2), onto which Ag was deposited by magnetron sputtering [VII]. The nominal thickness of Ag layer was 5, 10 and 20 nm. The composite catalysts were named as Ag5/MnO_2_MWCNT, Ag10/MnO_2_MWCNT and Ag20/MnO_2_MWCNT, respectively. The aim of this work was to prepare active and stable Ag/MnO_2_MWCNT composite catalysts for the ORR. The obtained catalysts showed high mass activities, and Ag/MnO_2_MWCNT1 catalysts showed superior stability during the 1000 potential cycles of accelerated stability test (AST), where catalysts with Ag nominal thickness of 10 and 5 nm showed only 4 and 2 mV decrease in their half-wave potentials.

6.7.1 Physical characterisation of Ag/MnO_2_MWCNT composites

The surface morphology of MnO_2-coated MWCNTs and Ag/MnO_2_MWCNT catalysts with different Ag loading is shown in SEM images in Figure 37. In the case of MnO_2_MWCNT2 (Figure 37b), the MWCNTs seem to be covered with a more evenly distributed MnO_2 layer, while MnO_2 on MnO_2_MWCNT1 (Figure 37a) seems to be more in the form of particles. Thus, Ag/MnO_2_MWCNT2 catalysts might have fewer defects where AgNPs have a direct contact with MWCNTs, whereas Ag/MnO_2_MWCNT1 possibly have more defects and, therefore better contact of AgNPs with MWCNTs. Figures 37c-h show MnO_2_MWCNT materials covered with Ag layers of different nominal thicknesses. At the thinnest layer of 5 nm of Ag, the substrate is covered with small AgNPs around 10 nm in size and cover the substrates evenly. At thicker layers of 10 and 20 nm, Ag particles start to merge and form an even layer that covers the whole MnO_2_MWCNT surface of both MnO_2_MWCNT substrates. The average Ag particle size for Ag5/MnO_2_MWCNT1 was 10 nm and 13 nm for Ag5/MnO_2_MWCNT2, which showed slight effect of the substrate. At a nominal thickness of 10 and 20 nm, some sub-10 nm particles were still visible, but most of the Ag uniformly covered the electrode surface. Similar structures of metal layers have been observed previously when magnetron sputtering has been used to prepare Ag, Pt, Pd and Au coatings on MWCNT substrates [45, 87, 88, 150-154].

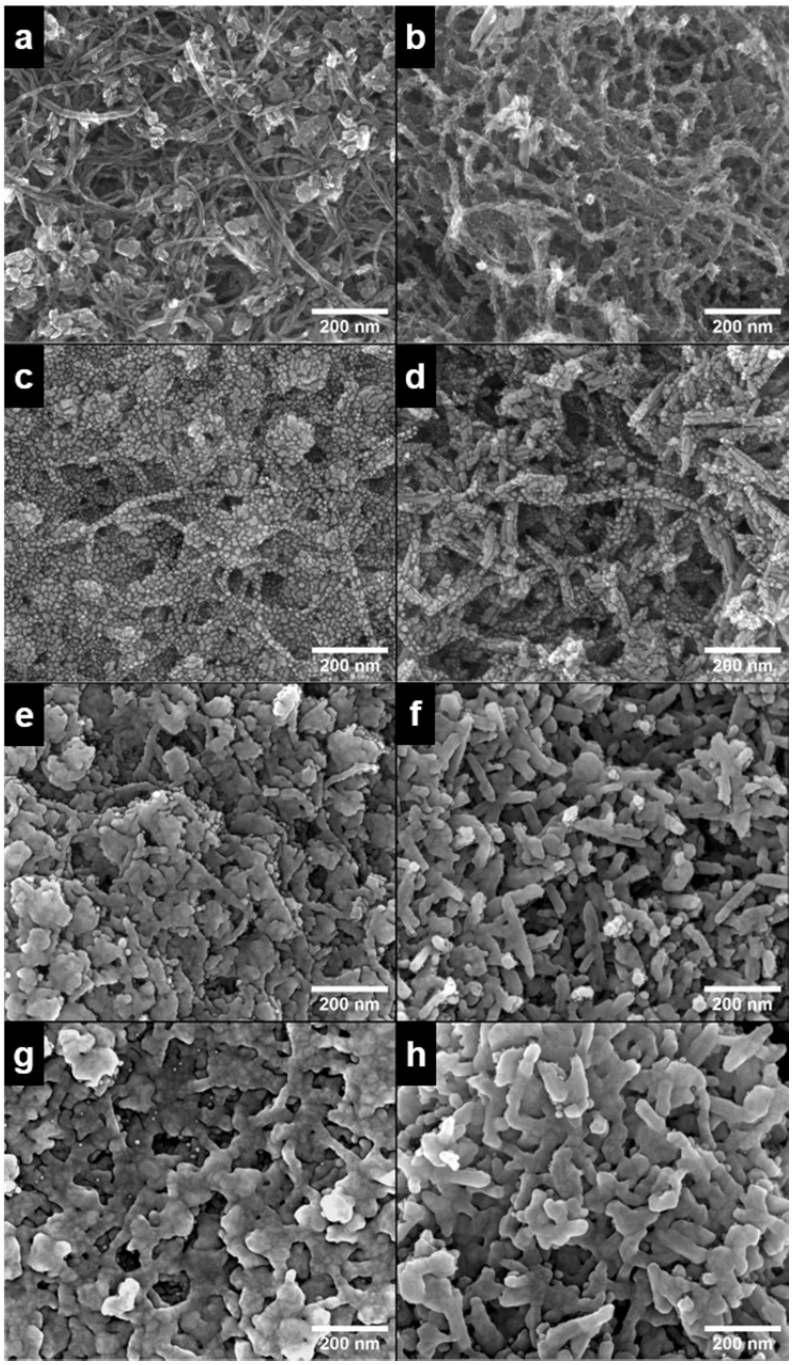

Figure 37. SEM images of (a) MnO_2_MWCNT1 and (b) MnO_2_MWCNT2 substrates; (c), (e) and (g) show Ag/MnO_2_MWCNT1 images of nominal Ag layer thickness of 5, 10, and 20 nm, respectively; (d), (f) and (h) show Ag/MnO_2_MWCNT2 images of nominal Ag layer thickness of 5, 10 and 20 nm, respectively.

The Ag, Mn, and C contents in Ag/MnO_2_MWCNT catalysts were determined by energy-dispersive X-ray spectroscopy (Table 6). As expected, the Ag loadings on MnO_2_MWCNT1 and MnO_2_MWCNT2 match. It is also evident that the Mn/C ratio is higher for Ag/MnO_2_MWCNT2 catalysts.

Table 6. Ag, Mn, and C content in Ag/MnO_2_MWCNT catalysts derived from the EDS analysis.

Catalyst	Ag /wt%	Mn /wt%	C / wt%
Ag20/MnO_2_MWCNT1	10 ± 1	38 ± 3	27 ± 4
Ag20/MnO_2_MWCNT2	10 ± 1	42 ± 12	16 ± 2
Ag10/MnO_2_MWCNT1	5 ± 1	34 ± 4	34 ± 4
Ag10/MnO_2_MWCNT2	6 ± 1	49 ± 6	11 ± 2
Ag5/MnO_2_MWCNT1	1.5 ± 0.1	37 ± 5	30 ± 4
Ag5/MnO_2_MWCNT2	1.5 ± 0.2	51 ± 4	11 ± 2

The Ag loading was determined using X-ray fluorescence on one additional sample (Si-plate) for each nominal Ag layer thickness. The following silver loadings were determined: 5.4 μg cm^{-2} for 5 nm, 10.7 μg cm^{-2} for 10 nm, and 22.9 μg cm^{-2} for 20 nm Ag layer. These values are in good agreement with the Ag loadings obtained from the EDS analysis, considering that the total catalyst loading was 250 μg cm^{-2} in all cases.

In Figure 38, the XPS results for the Ag10/MnO_2_MWCNT catalysts are shown. The XPS peaks for Ag, C, Mn, and O were observed. The Ag3d doublet is at 368 and 374 eV, the C1s peak at 284 eV, the Mn2p doublet is at 641 and 653 eV, and the O1s peak at 531 eV. The separation energy for Mn2p doublets' two peaks, 11.8 eV, matches the reported data [155-157]. Low Mn and carbon signals indicate that the substrate is almost completely covered with a Ag nanolayer.

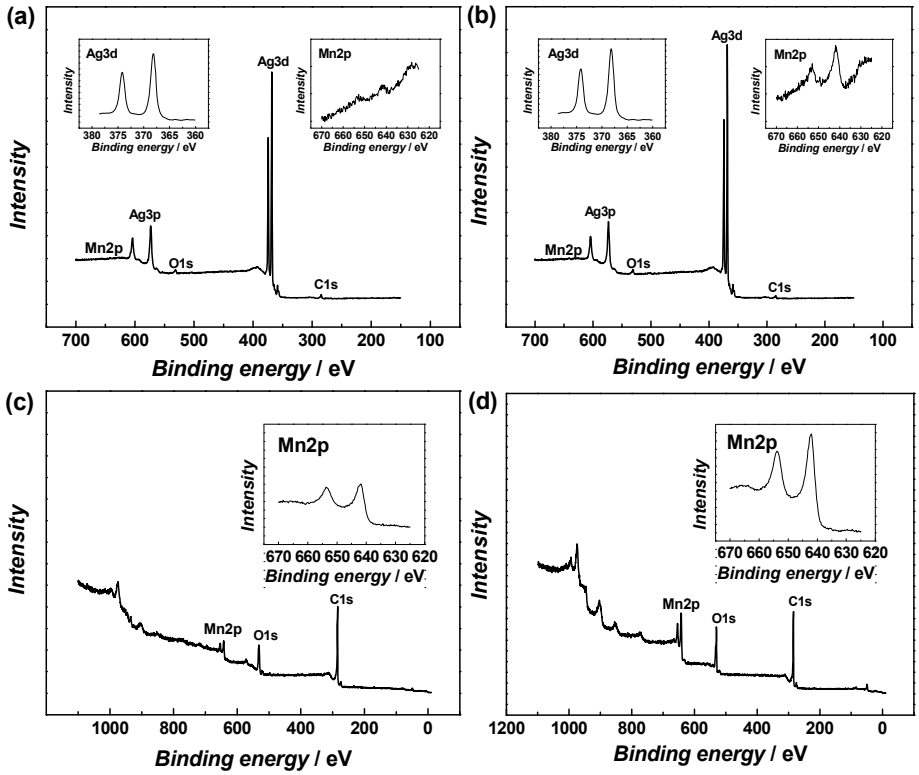

Figure 38. XPS survey spectra of (a) Ag10/MnO_2_MWCNT1 and (b) Ag10/MnO_2_MWCNT2 samples, insets show detailed XPS spectra in the Ag3d and Mn2p regions. XPS survey spectra of (c) MnO_2_MWCNT1 and (d) MnO_2_MWCNT2 substrate materials, insets show detailed XPS spectra in the Mn2p regions.

Figure 39 presents the XRD patterns of the substrates prior to the Ag deposition. MnO_2 crystallite sizes ranged between 5 and 15 nm. Both materials consist mainly of MnO_2 and its partially hydrated compounds, but the crystal structures differ. MnO_2_MWCNT1 contains a mixture of orthorhombic (ramsdellite, PDF 00-044-0142) and hexagonal MnO_2 as well as nsutites ($Mn(O,OH)_2$). In MnO_2_MWCNT2, MnO_2 has a tetragonal structure that matches well with α-MnO_2 (PDF 00-044-0141) and may be hydrated to some extent. From Figure 39, it is also evident that the C peak (25°2θ) of MnO_2_MWCNT1 is somewhat higher than that of MnO_2_MWCNT2, which is in accordance with the EDS results, where a lower Mn/C ratio was observed for Ag/MnO_2_MWCNT1 catalysts.

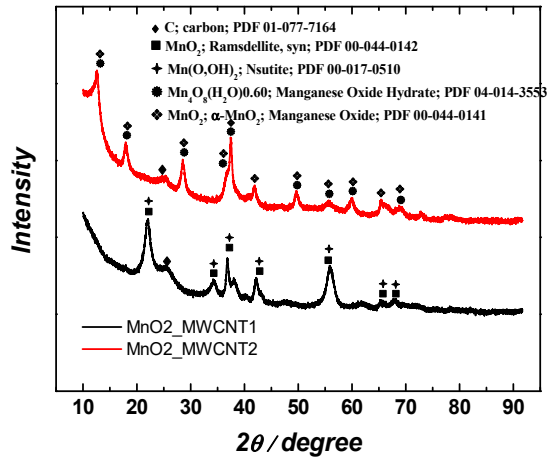

Figure 39. XRD patterns of MnO_2_MWCNT1 and MnO_2_MWCNT2 samples.

6.7.2 ORR studies on Ag/MnO_2_MWCNT composite catalysts

The comparison of the RDE polarisation curves at a single electrode rotation rate are presented in Figures 40a and 41a. The mass-activities for O_2 reduction were calculated at -0.2 V vs. SCE using the mass of silver on the electrode determined from the XRF data and kinetic current values at the given potential (see Eq. 6). It can be observed that Ag/MnO_2_MWCNT catalysts with a thickness of 20 nm had the most positive half-wave potential of -0.29 V, although Ag20/MnO_2_MWCNT1 catalyst showed a bigger MA value of 84 A g^{-1} compared to that of Ag20/MnO_2_MWCNT2 around 61 A g^{-1} (see Table 7). Ag5/MnO_2_MWCNT1 catalyst revealed the biggest MA of 126 A g^{-1}, while Ag10/MnO_2_MWCNT2 catalyst with nominal Ag layer thickness of 10 nm had MA value of 110 A g^{-1} and surpassed that of the other Ag/MnO_2_MWCNT2 catalysts. Ag/MnO_2_MWCNT catalysts in terms of the MA surpassed the results obtained with Ag-based catalysts where Ag was chemically deposited onto nitrogen-doped graphene oxide (see sub-section 6.5.2 [V], and Ag catalysts where Ag was deposited onto carbide-derived carbon (see sub-section 6.4.2) [IV]. A similar MA value of 94 A g^{-1} was obtained for Ag catalysts electrodeposited onto nitrogen-doped graphene oxide (see sub-section 6.3.2) [III]. Both Ag5/MnO_2_MWCNT catalysts had the most negative $E_{1/2}$ and Ag5/MnO_2_MWCNT2 had the smallest MA. All prepared Ag-based catalysts showed more positive half-wave potentials than the polycrystalline bulk Ag electrode. The half-wave potential of the ORR on Ag10/MnO_2_MWCNT1 and Ag5/MnO_2_MWCNT1 catalysts obtained in this part of the thesis are in a similar range to those obtained earlier on Ag sputter-deposited onto MWCNT with nominal Ag layer thickness of 15 nm [45]. The $E_{1/2}$ of bare AgNPs prepared by plasma-jet treatment was even lower than that of bulk Ag [42]. This might come from an increased number of active sites on Ag_2O layers formed on

Ag particles in the presence of Mn oxides, particle-to-particle ligand effects due to the proximity of Ag particles [75, 158]. Similar yet slightly higher $E_{1/2}$ values than for bulk Ag were obtained for electrodeposited AgNPs (see sub-sections 6.1.2, 6.2.3, 6.3.2) [I, II, III]. As compared to the commercial 20 wt% Pt/C catalyst, all Ag/MnO_2_MWCNT catalysts are less active for the ORR.

Table 7. Kinetic parameters for ORR on Ag-based catalysts in 0.1 M KOH. ω = 1900 rpm.

Catalyst	$E_{1/2}$ vs. SCE (V)	$\Delta E_{1/2}$ after AST (mV)	MA* (A g^{-1})	Tafel slope (mV)
Ag20/MnO_2_MWCNT1	-0.29	40	88	-85
Ag20/MnO_2_MWCNT2	-0.29	56	61	-82
Ag10/MnO_2_MWCNT1	-0.30	4	124	-81
Ag10/MnO_2_MWCNT2	-0.32	24	110	-93
Ag5/MnO_2_MWCNT1	-0.30	2	126	-81
Ag5/MnO_2_MWCNT2	-0.43	28	35	-94
Ag bulk	-0.37	n/a	n/a	-80
MnO_2_MWCNT1	-0.31	n/a	n/a	-86
MnO_2_MWCNT2	-0.41	n/a	n/a	-117
Pt/C	-0.16	n/a	n/a	n/a

*MA was calculated at -0.2 V vs. SCE.

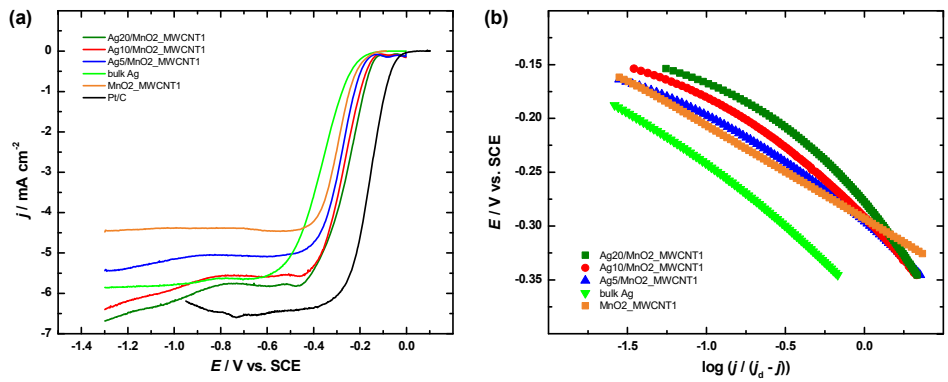

Figure 40. (a) Comparison of the ORR polarisation curves of the Ag/MnO_2_MWCNT1 catalysts and Pt/C in O_2-saturated 0.1 M KOH at 1900 rpm. v = 10 mV s^{-1}. (b) Mass-transfer corrected Tafel plots for ORR (data derived from (a)).

Electron transfer number values for the ORR on the catalyst materials were obtained using the K-L equation (Eq. 4). The n value for MnO_2_MWCNT1 and MnO_2_MWCNT2 materials was around 3, suggesting that the hydrogen peroxide formation occurs on both MnO_2_MWCNT1 and MnO_2_MWCNT2 supports and partial 2+2 electron pathway during the ORR is likely. The value of n was around four for all Ag/MnO_2_MWCNT catalysts, indicating that in the presence of Ag, either less hydrogen peroxide formed or it was more easily

reduced, or it disproportionated quicker [158]. 5 wt% of Ag-MnO_2 composite on single-walled carbon nanotubes and acetylene black are reported to catalyse the ORR via a direct 4-electron pathway, while the CNT-based composite is found to be more active overall [159]. Ag catalysts showed lower *n* values when Ag was electrodeposited on the GC electrodes and when Ag-Mn_xO_y was deposited onto the reduced graphene oxide and nitrogen-doped graphene oxide substrates (see section 6.1.2) [I] [97, 160]. Ag catalysts deposited onto electrospun lignin-derived carbon fibre mats showed the *n* values below 4 due to AgNPs at higher loadings growing in size and the diffusion effects of reacting species [161]. Guo and co-workers varied Ag loadings deposited onto conventional Vulcan carbon substrate and observed a 4-electron ORR for Ag catalysts where the loadings were 20 wt% and higher (up to 60 wt%) and a 2+2 electron pathway for 10 wt% [63]. Fazil and Chetty prepared Ag catalysts on CNTs with 20 wt% and 40 wt% and, similarly to Guo and co-workers, obtained *n* values close to four [81]. In the previous part of this thesis, where AgNPs were deposited onto two different mesoporous engineered catalyst supports with 40 wt% nominal Ag loading, the *n* values close to four were obtained (see subsection 6.6.2) [VI].

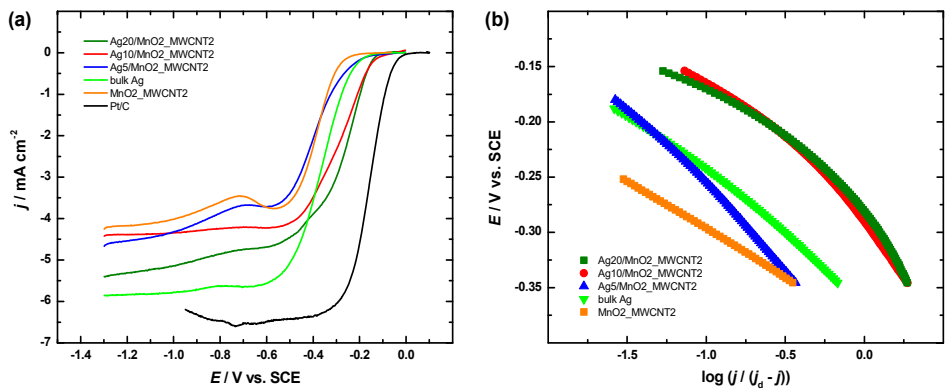

Figure 41. (a) Comparison of the ORR polarisation curves of the Ag/MnO_2_MWCNT2 and Pt/C catalysts in O_2-saturated 0.1 M KOH at 1900 rpm. v = 10 mV s^{-1}. (b) Mass-transfer corrected Tafel plots for ORR (data derived from (a)).

Figures 40b and 41b present mass-transfer corrected Tafel plots for the ORR in 0.1 M KOH derived from the RDE data in Figures 40a and 41a, respectively. The Tafel slope values for Ag/MnO_2_MWCNT catalysts (in potential range from -0.15 V to -0.25 V) were similar and were between -81 and -94 mV regardless of the nominal thickness of the sputter-deposited Ag layers (Table 7). Tafel slope values of -91 and -163 mV have been obtained for Ag-based catalysts where Ag was deposited onto MnO_2 nanorods (Ag/MnO_2) and clean MnO_2 nanorods, respectively [86]. Continuously changing Tafel slopes of -70 to -80 mV and -120 to -130 mV have been reported for Ag(hkl) single crystal facets, and their occurrence has been explained by changes in the concentration

of adsorbed oxygenated species and strong lateral competition between OH^- ions and other adsorbed species of reaction intermediates, as well as changes in the reaction steps and mechanism of the ORR that depend on variations in the electrode surface structure [22, 38, 97]. Thus the, Tafel slope values of Ag catalysts depend on the difference in catalyst structure [34]. AgNPs have shown Tafel slope values of -95 and -134 mV, and Ag nanosheet arrays values of -60 and -120 mV. Substrates might play a role in different Tafel slope values [45]. For instance, -59 and -60 mV have been obtained for Ag catalysts where Ag was deposited onto the NGO substrate (see sub-sections 6.3.2 and 6.5.2) [III, V]. It could be reasoned that since the Tafel slope values for pure substrate and Ag-covered substrate were very similar, the ORR might partially proceed on the substrate as discussed in sub-section 6.5.2 [V] and in Ref. [54]. As the Tafel slope values of MnO_2_MWCNT2 differ from that of Ag on this support, then we can assume that the ORR proceeds mainly on the Ag surface. However, the same assumption cannot be made for MnO_2_MWCNT1. The ORR on Ag catalysts might also be influenced by the Ag deposition method (see sub-sections 6.1.2 and 6.2.3) [I, II]. The Tafel slope values between -71 and -80 mV have been obtained with Ag catalysts where AgNPs were synthesised using pulse charge deposition and vacuum dried onto the GC electrodes [42]. As the Tafel slope values herein remained similar to that of bulk Ag, we expect the reaction mechanism to be the same on Ag/MnO_2_MWCNT catalysts and on bulk Ag.

Accelerated stability tests (1000 potential cycles in the range from -1.3 V to 0 V vs. SCE at a scan rate of 100 mV s^{-1}) of Ag/MnO_2_MWCNT1 and Ag/MnO_2_MWCNT2 catalysts were also conducted. Figure 42a-f shows the ORR polarisation curves for catalysts with different nominal Ag layer thickness before and after the 1000 potential cycles at ω = 960 rpm. Regardless of Ag nominal thickness, Ag/MnO_2_MWCNT1 catalysts showed higher stability than Ag/MnO_2_MWCNT2 catalysts (see Table 7). A decrease in the half-wave potential values could be caused by silver oxidation, dissolution, and Ag particles re-organisation via redeposition. Ag/MnO_2_MWCNT1 catalysts showed the highest stability when Ag layer nominal thicknesses were 5 and 10 nm, for which the $E_{1/2}$ change was only 2 and 4 mV, respectively. There could be several additional reasons for that, for example, Liu and co-workers suggest that the enhanced stability might come from a synergistic effect between Ag and Mn_3O_4 nanoparticles [75]. The synergistic effect is implied to include an ensemble effect between Ag and Mn_3O_4 nanoparticles, where on Mn_3O_4, hydroperoxide ions form and then diffuse or re-adsorb to the AgNPs, where they can disproportionate or be further reduced to OH^- ions [74, 75, 86]. Part of the synergistic effect might arise from the electron transfer from carbon substrate to Mn_3O_4, which creates a positive charge on adjacent carbon surfaces allowing for side-on O_2 adsorption, where O-O bonding is weakened, and it facilitates the 4-electron pathway [75, 158]. Hu and co-workers suggested that in case of Ag/MnO_2 catalysts, oxygen vacancies could play a role in the ORR invigorating synergistic effect [86]. In case of Ag/MnO_2_MWCNT2 catalysts,

there may be fewer available carbon sites along MnO_2, and only the ensemble effect between Ag and MnO_2 might affect the electroreduction of the formed peroxide intermediates, which in turn could induce a higher decrease in half-wave potential after AST for Ag/MnO_2_MWCNT2 catalysts.

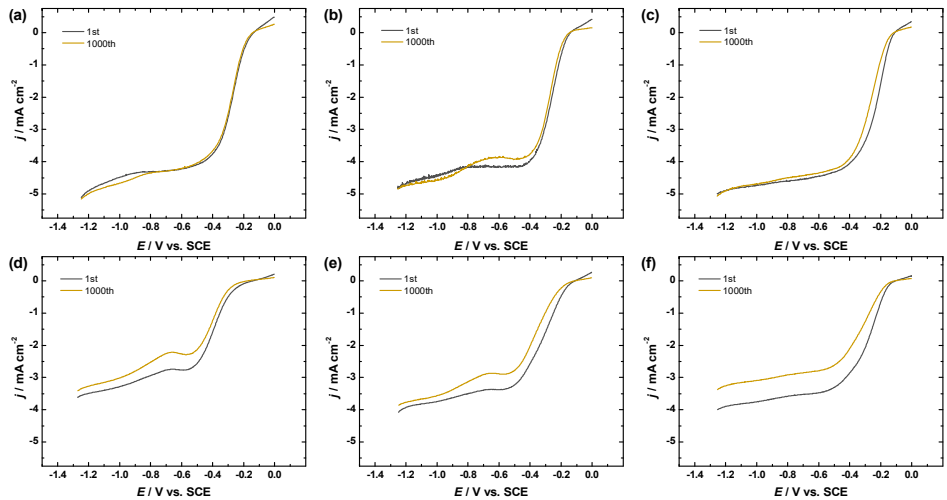

Figure 42. The RDE polarization curves of oxygen reduction on (a) Ag5/MnO_2_MWCNT1, (b) Ag10/MnO_2_MWCNT1, (c) Ag20/MnO_2_MWCNT1, (d) Ag5/MnO_2_ MWCNT2, (e) Ag10/MnO_2_MWCNT2, (f) Ag20/MnO_2_MWCNT2 catalysts in O_2-saturated 0.1 M KOH before and after the AST. ω = 960 rpm, v = 10 mV s^{-1}. Background current not subtracted.

6.8 ORR on thin-film Ag electrodes in alkaline solution

In the eighth part of the work, Ag thin films were deposited with 5 different nominal layer thicknesses 0.5, 1, 2, 5, and 10 nm [VIII]. The thin Ag films were deposited onto the clean GC electrodes using the electron beam evaporation method. This method avoids the need for potentially environmentally unfriendly chemicals. The purpose of this work was to study a nominal Ag layer thickness/loading effect on activity of ORR.

6.8.1 TEM studies of thin Ag films

Figure 43 presents TEM images of thin-film Ag samples. In general, the TEM images of thin Ag films are similar to thin-film Pt, Au and Pd samples that have been investigated previously [162-165]. It was observed that initially island-like Ag nanoparticles are formed. The particle size for 0.5 nm film was 5.5 ± 2.7 nm. When the nominal thickness of the film increased to 1 nm (Figure 43b) then the number of smaller particles decreased as they grew bigger. The average particle size was determined to be 5.9 ± 2.1 nm for 1 nm Ag film. As the film thickness

increased to 2 nm, then the particles started to merge and thus the average particle size increased to 12.8 ± 2.6 nm. However, some sub-5 nm particles can be also observed (Figure43b). With 5 nm Ag film there are only some individual nanoparticles visible as most of silver is merged together (Figure 43d) and for 10 nm film the whole surface is covered with a Ag coating.

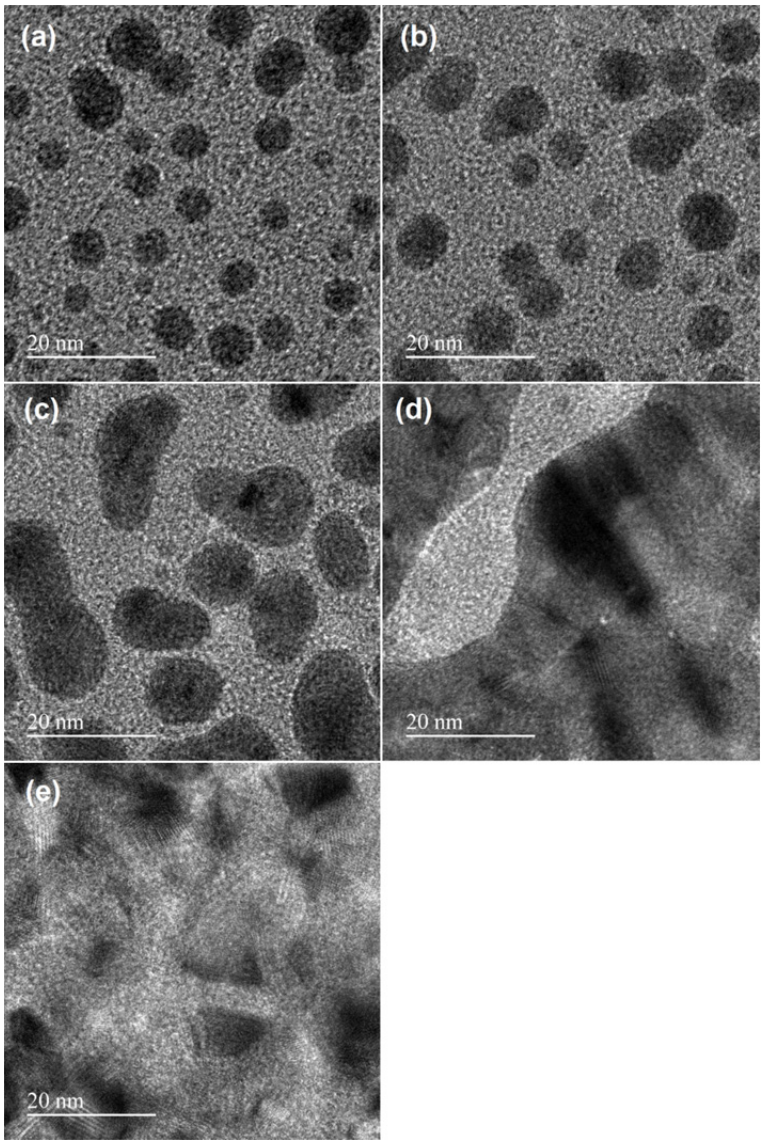

Figure 43. TEM images of 0.5 nm (a), 1 nm (b), 2 nm (c), 5 nm (d) and 10 nm (e) Ag films.

6.8.2 ORR studies on thin Ag films

The collected RDE polarisation data was analysed using the K-L equation (Eq. 4). From which the values of *n* have been calculated. The *n* value was 3.8 for the thinnest Ag film, but for 1 nm and thicker films it was 4 in the whole range of potentials studied. Compton and co-workers have shown that sparsely distributed AgNPs catalyse the ORR via a 2-electron pathway [62, 166]. They found that the interparticle distance, which is more than 30 times higher than the particle size will yield hydrogen peroxide as the final product of the ORR, as it is diffusing away from the electrode surface. When the interparticle distance is decreased then the peroxide yield also decreases as the probability for peroxide adsorption and further reduction increases. The results in this part of the thesis show that a 0.5 nm Ag film is not covering the electrode substrate completely and some formed hydrogen peroxide can still escape. However, thin Ag film with 1 nm nominal Ag layer thickness already has the number density of AgNPs that is sufficiently high and the interparticle distance which is already low enough to catalyse ORR via a $4e^-$ pathway. The ORR on thicker films follows 4 electron pathway. These results are in a good agreement with the earlier findings, where it was suggested that Ag particle size is a crucial factor for determining the ORR pathway [32]. When 174 and 4.1 nm Ag particles were compared for the ORR activity, it was concluded that bigger particles catalyse a $4e^-$ ORR pathway and on smaller particles both $4e^-$ and $2e^-$ pathways occur at the same time [33]. This means that the ORR proceeds at least partially via a 2-electron pathway on silver and the formed hydrogen peroxide is further reduced to OH^- anions.

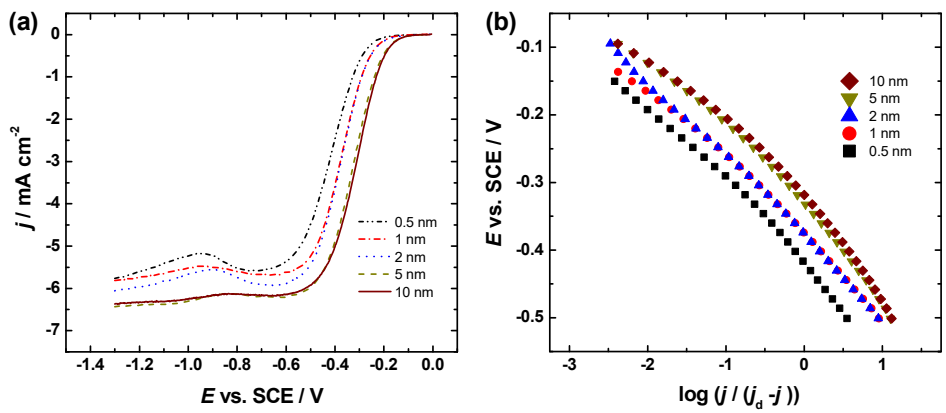

Figure 44. Comparison of the ORR polarisation curves on thin-film Ag electrodes in O_2-saturated 0.1 M KOH solution (a) and the corresponding Tafel plots (b) derived from (a). ω = 1900 rpm, v = 10 mV s^{-1}.

Figure 44a presents a comparison of the ORR results for thin-film Ag electrodes with different thicknesses. The half-wave potentials for O_2 reduction increased

with increasing nominal Ag film thickness, also a minimum in the diffusion-limited current can be observed. This minimum at about -0.9 V vs. SCE is detected for all Ag/GC electrodes, however, it decreases with increasing the nominal thickness of the Ag film. This minimum is attributed to the characteristic behaviour of Ag and could be related to potential dependent adsorption of OH, which is strongly adsorbed on the Ag surface and the desorption of which should improve the ORR activity [16].

Tafel analysis was carried out based on the RDE data on O_2 reduction and the corresponding plots are presented in Figure 44b. As can be seen, the Tafel plots are almost parallel. From these plots, the Tafel slope values were determined, and these values were between -80 and -100 mV. Similar Tafel slope values have been reported previously in several studies (see also sub-sections 6.1.2, 6.2.3, 6.5.2) [I, II, V] [42, 45]. Also different Ag catalyst structures like nanoparticles and nanosheet arrays have different Tafel slope values [28]. For example, Ag nanosheet arrays had slopes of -60 and -120 mV, while nanoparticles had corresponding slopes of -95 and -134 mV. The changes in the Tafel slope have been attributed to various aspects, e.g. changes in adsorption conditions of oxygen intermediates [34] and a small Ag quantity on the electrode surface would also give constantly changing Tafel slope value [97]. In contrast, it has also been suggested that different Tafel slope values could be obtained by incorrect solution resistance correction [96]. Based on the Tafel slope values in the studied potential range it can be stated that the transfer of the first electron to the O_2 molecule is the rate-determining step for the ORR process.

To compare thin-film Ag electrodes more thoroughly, the MA and SA values for O_2 reduction were calculated at -0.25 V vs. SCE by dividing kinetic current to mass of Ag (Eq.-s 6 and 7), or to real electroactive surface area of Ag catalysts obtained from Pb_{upd} measurements or the Ag oxide reduction peak (Eq. 5). The MA values of the thin Ag films were 82, 123, 137, 206 and 137 A g^{-1} for 10, 5, 2, 1 and 0.5 nm Ag film, respectively. This means that there is a maximum in the mass-activity at a nominal Ag film thickness of 1 nm. In previous parts of this PhD thesis, with the electrodeposited Ag coatings a maximum in the MAs was not observed nor any essential dependence on the deposition time (see also sub-sections 6.1.2 and 6.2.3) [I, II]. This could be related to the morphology of the AgNPs, similar to the case when Ag was electrodeposited from aqueous solution, as there were clearly visible bigger agglomerates (see sub-section 6.1.1) [I]. When Ag was deposited from non-aqueous solution then the large Ag agglomerates were not observed, still, the AgNP size was considerably bigger (see sub-section 6.2.1) [II] than that determined in the present part of the thesis. However, Salome and co-workers have reported a dependence of the MA on the size of Ag particles, as smaller ones exhibited higher MA [113]. While in ref. [113] there were relatively large particles, Lu and Chen reported that 0.7 nm Ag clusters possess superior electrocatalytic activity towards the ORR as compared to the 3.3 nm Ag particles [35]. Specific activity calculated by using silver oxide reduction peak

was the lowest for a 5 nm film (38 μA cm^{-2}) as compared to 10, 2, 1 and 0.5 nm Ag films, which possessed the SA values of 43, 41, 59 and 56 μA cm^{-2}, respectively. These values are rather small, which could be due to inaccurate method of determination of the real surface area of Ag catalysts. The specific activities calculated using A_r from Pb_{upd} followed similar trend, as the SA values were 1.0, 0.93, 1.3, 1.4 and 1.5 mA cm^{-2} for 10, 5, 2, 1 and 0.5 nm Ag films, respectively. These results indicate that 1 nm Ag film is the most active electrode as it has highest mass-activity and nearly the highest specific activity. However, even when comparing differently shaped AgNPs, the tendencies can be different as has been shown using Ag nanowires and nanoparticles [37]. Namely, nanoparticles displayed increasing specific activity values (A_r was determined from the oxide reduction peak) with increasing particle size (from 2.4 to 40 nm), while the mass activity decreased, and with Ag nanowires both the MA and the SA decreased when increasing the nanowire diameter. Thus, one must pay special attention to the details when comparing the Ag-based electrocatalysts for the ORR.

6.8.3 H_2O_2 reduction studies on thin Ag films

As hydrogen peroxide is a side product of the ORR, then the hydrogen peroxide reduction experiments were carried out. The potential at which the current is zero is slightly dependent on the nominal film thickness. However, the difference is very subtle being only 15 mV between the least and the most active thin-film Ag electrodes. The variations in the diffusion-limited current densities indicate about the overall coating of the electrode, the thinnest film had separate particles and thickest film entirely covered the substrate surface. When comparing the polarisation curves of the hydrogen peroxide reduction to those of oxygen reduction, it is clearly visible that the hydrogen peroxide reduction half-wave potentials are strongly shifted towards more positive values. This shows that Ag is very efficient catalyst for hydrogen peroxide reduction reaction.

The hydrogen peroxide reduction polarisation curves were also subjected to the K-L analysis, which showed that the number of electrons transferred per hydrogen peroxide anion was 2 for all Ag films. This confirms that the formed HO_2^- is further reduced to OH^-. However, the ORR results show some hydrogen peroxide is still escaping from the electrode to the solution. Various Ag-based catalysts have shown good electrocatalytic activity for hydrogen peroxide reduction in alkaline media such as AgNPs supported on carbon nanotubes, nitrogen-doped carbons, carbide-derived carbons and even unsupported AgNPs (see also sub-sections 6.1.3, 6.4.3, 6.5.3) [I, IV, V] [45]. Using the cyclic voltammetry method the structure dependence of AgNPs for hydrogen peroxide reduction has been demonstrated [167]. Namely, the Ag nanoprisms had higher activity in terms of the onset potential and currents remained higher in time compared to nanocubes and nanospheres. It was

suggested that hexagonally close-packed lamellar defects contribute to the higher activity.

6.8.4 CV and Pb_{upd} studies on thin Ag films

After the ORR measurements the electrodes were again transferred to Ar-saturated 0.1 M KOH and cyclic voltammetry measurements were carried out to study the silver oxidation behaviour (Figure 45). As expected, the oxide reduction peak increases with increasing the nominal thickness of the Ag films. This peak has been used to calculate the electroactive surface area of silver, however, the positive potential limit is crucial as silver may oxidise further and irreversible oxides may form and there has been even suggestions that this method should not be used for electroactive surface area determination [95, 96].

The oxidation peak at $E > 0$ V consists of several processes as has been described previously [63, 102]. The first two peaks correspond to the initial stages of silver oxidation, the third peak corresponds to Ag_2O formation, while increasing the potential further would result in Ag_2O_2 formation and, already in the oxygen evolution reaction region, highest Ag oxide Ag_2O_3 formation [102]. During the experiments, the upper vertex potential for the CVs was limited to 0.4 V vs. SCE, which means that Ag_2O_2 should not form yet. However, there are significant differences in the CV behaviour of Ag films that originate from the differences in surface morphology. For example, 5 nm and 10 nm thick Ag films cover the entire GC electrode and thus yield a different response as compared to the thinner Ag films.

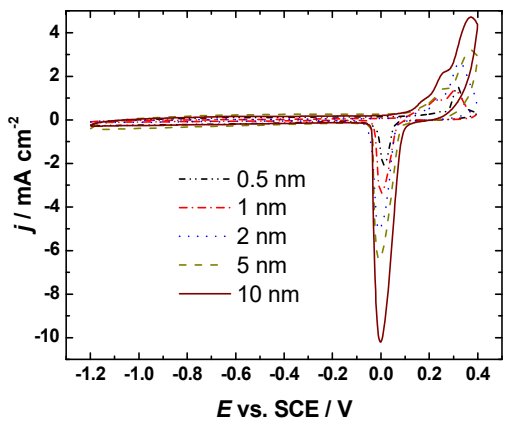

Figure 45. CVs of thin Ag films in Ar-saturated 0.1 M KOH. $v = 100$ mV s^{-1}.

As a comparative method Pb_{upd} and subsequent stripping was carried out (Figure 46) to determine the electroactive surface area of Ag catalysts. The charge corresponding to Pb stripping was used to calculate the A_r of Ag. However, this method has been criticised to not be entirely suitable for small AgNPs [99]. When comparing the values of A_r determined by oxide reduction

peak and Pb_{upd} results, then the values from oxide reduction are significantly higher. The surface areas from Ag oxide reduction are overestimated and the values obtained from Pb_{upd} are more plausible. As the amount of Ag is small, the Ag particles are also small, and it could be that the oxides are thusly more easily formed. In addition, oxide formation is then not limited by the monolayer and can lead to overestimated A_r values. Even though neither method for determination of the A_r of silver is clear from contradicting claims, both could be used to give insight to the ORR results. Similar discrepancies between the surface area determination by surface oxidation and Pb_{upd} were observed in the second part of the thesis (see sub-section 6.2.3) [II].

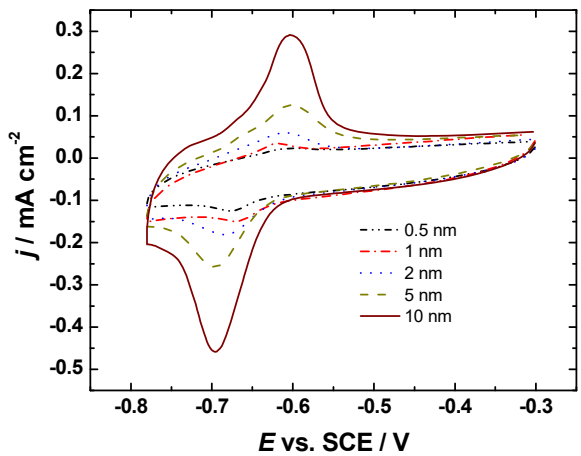

Figure 46. Comparison of Pb_{upd} on thin-film Ag electrodes in Ar-saturated 0.1 M KOH solution containing 0.5 mM $Pb(NO_3)_2$. v = 50 mV s^{-1}.

6.8.5 Ag dissolution studies on thin Ag films

After the experiments, Ag was electrochemically stripped from the GC electrode surface in 0.1 M $NaClO_4$ solution (Figure 47). As presented in Figure 47, the Ag dissolution gives a peak with only a single maximum for which the current starts to increase at about 0.3 V and the position of the maximum depends on the nominal loading of the Ag film. On the reverse scan, some amount of the dissolved Ag is re-deposited, as a small broad peak is present at potentials from 0.3 to 0.1 V. This occurs as the diffusion of Ag is slow and Ag^+ cations remain near the surface of the electrode. The mass of Ag was calculated using Eq. 7. For comparison, the theoretical mass of Ag was also calculated using the GC disk area and the nominal thickness of Ag films. Based on this calculation the mass of Ag for 10, 5, 2, 1 and 0.5 nm films were 2.10, 1.05, 0.42, 0.21 and 0.10 µg, respectively, and based on the Ag stripping experiments the masses were 2.35, 1.53, 0.88, 0.23, 0.17 µg, respectively. The electro-chemical stripping of Ag gave slightly higher silver mass values than the

theoretical value, but they were within reasonable error margin and variations originate from the differences during the deposition process.

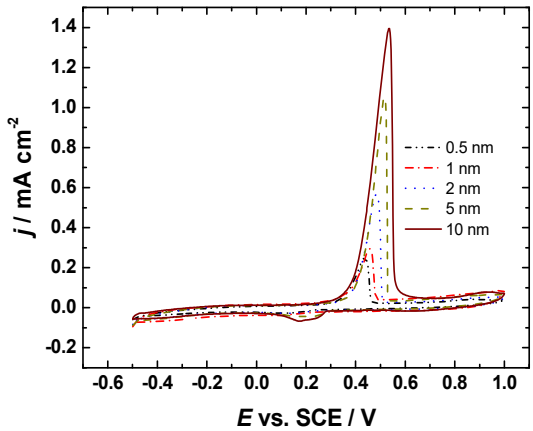

Figure 47. A comparison of dissolution curves of thin Ag films in Ar-saturated 0.1 M $NaClO_4$ solution. $v = 10$ mV s^{-1}.

6.9 AgNW-based catalysts for ORR in alkaline solution

In the ninth part of the work, commercial AgNWs with diameters of 35, 90, and 120 nm were bought and tested for the ORR [IX]. The purpose of this work was to determine the effect of Ag nanowires thickness/diameter on the ORR activity and stability of Ag catalysts.

6.9.1 SEM studies of AgNWs

To determine the surface structure of AgNWs used in this study the SEM method was used. Figure 48 presents the typical SEM micrographs of AgNWs with the diameters of 35, 90 and 120 nm. Figure 48 shows that AgNWs correspond to nominal diameters. Generally, the AgNWs are straight, and their surface is very smooth. Stacked in chaotic orientation, AgNWs are of cylindrical shape with estimated length of ca. 0.5, 1 and 2 μm for 35, 90 and 120 nm AgNWs, respectively. Moreover, the density of AgNWs is very high and the presence of various nanochannels can facilitate the transport of O_2 molecules to the catalyst surface.

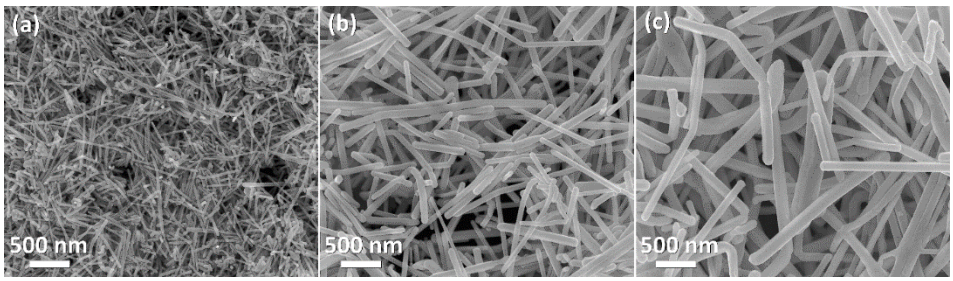

Figure 48. SEM micrographs of Ag nanowires of (a) 35, (b) 90 and (c) 120 nm in diameter.

6.9.2 ORR studies on AgNWs

The electrocatalytic behaviour of AgNWs and polycrystalline bulk Ag electrode were compared at a single electrode rotation rate (see Figure 49a). The half-wave potential values were calculated at 1900 rpm. The most active AgNWs with a diameter of 35 nm exhibited 12 mV higher $E_{1/2}$ value than that of bulk Ag electrode (0.649 vs. 0.637 V). Similar half-wave potentials were obtained in other recent works (see also sections 6.3.2and 6.4.2) [IV, III] [145, 168].

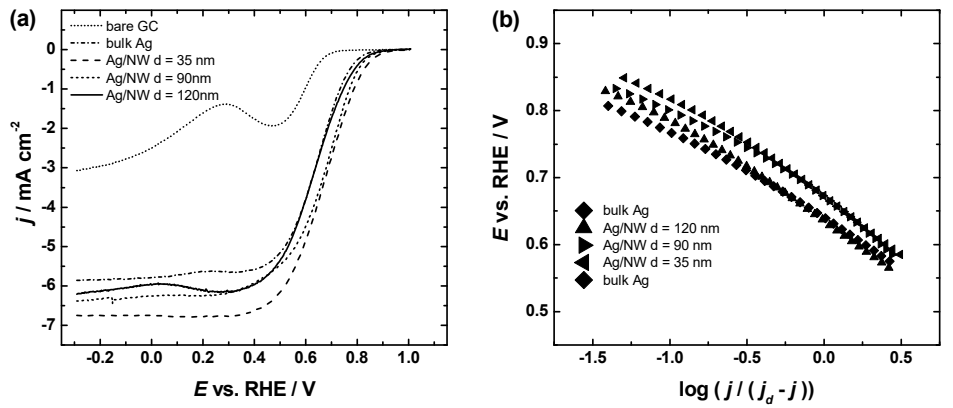

Figure 49. (a) Comparison of polarisation curves for O_2 reduction on AgNWs and bulk Ag, ω = 1900 rpm. (b) Mass-transfer corrected Tafel plots (data derived from a). Test solution: O_2-saturated 0.1 M KOH, v = 10 mV s^{-1}.

The K-L equation was used to determine the kinetic parameters. The number of electrons transferred per O_2 molecule was calculated from the RDE data using the K-L equation (Eq. 4). The calculated n value was close to four for all AgNW catalysts studied. This indicates that the ORR occurs mainly through a $4e^-$ reaction pathway on AgNW-modified electrodes. Quantum chemical studies have shown that Ag(111) facets undergo a 4-electron O_2 reduction and that a large amount of adsorbed OH^- ions on the surface facilitates the formation of a reaction intermediate, hydrogen peroxide ion (HO_2^-) [16, 17]. For AgNWs with larger diameter, the n value was slightly lower than 4, and this result is

comparable to a previous part where thin Ag films (see also section 6.8.2.1) [VIII] and Ag-AgCl core-shell nanowires decorated with AgCl (AgCl-Ag@AgCl NWs) were studied [131]. It was proposed that strongly adsorbed OH^- species on defective surfaces obstruct adsorption of O_2 to neighbouring Ag sites, thus increasing the fraction of 2-electron reaction pathway [13]. Based on the SEM results, we can propose that defects present on AgNWs with diameter of 120 nm weakens the adsorption of O_2 and the first charge-transfer has higher activation energy compared with the surface of AgNWs with smaller diameters. Blizanac and co-workers observed that the most active surface is Ag(110) and the least active is Ag(100) plane. Although not without some contradictions, namely, the Ag(110) surface has the smallest activation energy and shows the biggest affinity towards already reduced OH_{ads} species, limiting the number of sites for O_2 molecules to adsorb. To adsorb, superoxide anion (O_2^-) actually needs two sites. While the Ag(100) surface has the highest activation energy and shows more moderate affinity towards the product species. Ag(111) surface has the least affinity towards the OH_{ads} [22]. The crystal structure of AgNWs has been studied and is presented in the literature [37, 169, 170]. According to measurements conducted by Alia and co-workers it was observed that the AgNWs are round and do not have one certain facet, rather a mixture of them [37].

The RDE polarisation data was used for the Tafel analysis (Figure 49b). Almost parallel Tafel plots at low overpotentials were obtained for all the electrodes studied with slope values of -100, -100, -101 and -91 mV for 35, 90, 120 nm AgNWs and bulk Ag, respectively. The Tafel slope values for the AgNWs with different diameters did not differ amongst each other and were very close the slope value of bulk polycrystalline Ag electrode (-91 mV). These values indicate that the mechanism of the ORR on AgNWs is the same as that on the polycrystalline Ag electrode. The slope values at high overpotentials increased for all the catalyst materials studied. Similar Tafel slope values have been obtained in earlier studies [42, 45, 109-111]. Taking into account observations by Blizanac and co-workers, the Tafel slope values for the Ag(110) were constantly changing between -80 and -120 mV [22]. In addition, for the Ag(111) and Ag(100) at higher overpotentials the slope values were close to -120 and -130 mV and at lower overpotentials close to -70 and -80 mV [22]. These Tafel slope values suggest that the first electron transfer to the O_2 molecule is the rate-determining step in the overall ORR process.

6.9.3 CV studies on AgNWs

After the RDE measurements AgNW-modified electrodes were cycled in Ar-saturated 0.1 M KOH at potentials ranging from -0.2 to 1.4 V vs. RHE. The obtained CV curves with different materials are compared in Figure 50a. The CVs exhibit same behaviour as those discussed in previous parts of the thesis as well as literature [63, 102].

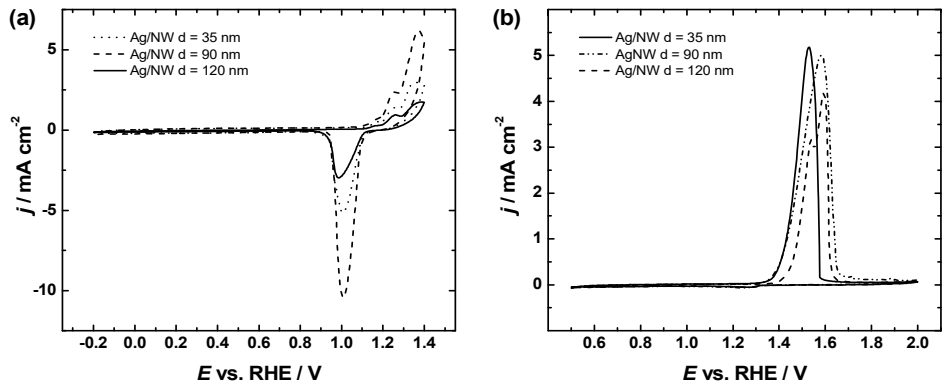

Figure 50. (a) Comparison of CVs of AgNWs with a diameter of 35, 90 and 120 nm in Ar-saturated 0.1 M KOH, v = 100 mV s^{-1}. (b) Comparison of Ag stripping profiles of AgNW-modified electrodes in Ar-saturated 0.1 M $NaClO_4$ solution, v = 10 mV s^{-1}.

To evaluate the electrocatalytic activity of different AgNW catalysts, it is typical to determine the specific activity for ORR of the modified electrodes. In the case of silver, the correct determination of the electroactive surface area of Ag is somewhat complicated, because it depends on the method chosen and thus it was not attempted in this part of the study. The determination of Ag mass was performed by electrochemical stripping of silver from GC electrode, as shown in Figure 50b. At potentials higher than 1.3 V vs. RHE, the Ag starts to dissolve from the electrode surface, and some dissolved Ag deposits back onto the GC electrode (small cathodic peak in the range of 1.4-1.2 V).

By the integration of charge under the anodic silver dissolution peak, the amount of dissolved Ag was calculated using Eq. 7. The calculated Ag masses were 11.4, 13.6 and 9.5 µg for AgNWs with diameters of 35, 90 and 120 nm, respectively. The obtained masses were used to calculate the MA values at 0.8 V and 0.85 V vs. RHE using the dissolved Ag mass and kinetic current values at the given potential (Eq. 6). The calculated MA values, along with other kinetic parameters, are summarised in Table 8. The obtained MA values are comparable to a previous part of this thesis and the literature (see also sub-section 6.3.2) [III] [133]. For example, Ag-based catalysts, where silver was electrodeposited onto four different carbon substrates, the MA values at 0.8 V were very similar (see sub-section 6.3.2) [III]. In addition, the MA values at 0.85 V compared to MA

values obtained in a study by Cai and co-workers, where the ORR was tested on Ag catalysts prepared by rapid precipitation-reduction synthesis, were also close [133].

Table 8. The ORR kinetic parameters for AgNW-modified GC and bulk Ag electrodes in 0.1 M KOH.

Catalyst	MA at 0.8 V ($A\ g^{-1}$)	MA at 0.85 V ($A\ g^{-1}$)	$E_{1/2}$ vs. RHE (V)	Tafel slope (mV)	n
35 nm AgNW	19.6	7.2	0.649	-100	4.2
90 nm AgNW	6.6	3.2	0.643	-100	4.1
120 nm AgNW	9.4	2.3	0.619	-101	4.1
Bulk Ag	-	-	0.637	-91	4.1

6.9.4 H_2O_2 reduction studies on AgNWs

It was of interest to test the AgNWs for hydrogen peroxide reduction reaction, as Ag-based catalysts can be used in hydrogen peroxide detectors [114]. Hydrogen peroxide is also a side product of the ORR; therefore, the hydrogen peroxide reduction reaction studies play an essential role when investigating the electrochemical ORR behaviour on Ag-based catalysts. Figure 51 presents a comparison of polarisation curves for hydrogen peroxide reduction obtained with the AgNW-modified GC electrodes in Ar-saturated 0.1 M KOH solution containing 1 mM HO_2^-. The K-L equation (Eq. 4) was used, and the number of electrons transferred per hydroperoxide anion was calculated to be close to 2. This confirms that if during the ORR process some hydrogen peroxide forms, it is immediately reduced further to OH^-. These results are in agreement with fundamental studies by Adanuvor and White, where pre-reduced silver electrode undergoes $4e^-$ reduction and produces minimal hydrogen peroxide as an intermediate [171]. In a strongly alkaline electrolyte (6.5 M NaOH), two-wave O_2 reduction polarisation curves were observed for Ag electrodes, where the first reduction wave corresponded to 4-electron reduction and the second wave to the $2e^- + 2e^-$ reduction process [171]. From Figure 51 it is evident that all three catalysts are electrocatalytically active for the hydrogen peroxide reduction.

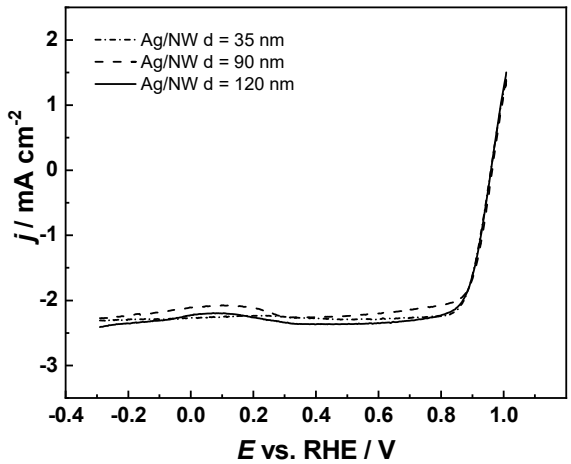

Figure 51. A comparison of polarisation curves for peroxide reduction on the GC electrodes covered with AgNWs with three different diameters, ω = 1900 rpm. Test solution: Ar-saturated 0.1 M KOH containing 1 mM HO_2^-, v = 10 mV s^{-1}.

6.9.5 Stability of AgNW catalysts

The stability of the GC electrodes modified with AgNWs was tested using continuous potential cycling (1000 cycles in the range from -0.3 to 1.0 V vs. RHE). The ORR polarisation curves of 35, 90 and 120 nm AgNW catalysts obtained after prolonged cycling in 0.1 M KOH solution are displayed in Figure 52a-c, respectively. The value of the current density in the diffusion-limited region of the polarisation curve obtained after the test is slightly higher than that obtained at the initial polarisation curve. This can be explained by the fact that a small amount of hydrogen peroxide formed during the repetitive potential cycling breaks down the organic impurities, i.e. PVP that was used to synthesise and store the AgNWs [100, 169, 172], cleans the electrode surface and increases the electrocatalytic activity of the electrode. The half-wave potentials decreased only by 16 mV for 120 nm and 12 mV for 35 nm AgNW, with a slight increase of 4 mV for 90 nm AgNW catalyst. The decrease in $E_{1/2}$ values could come from the silver oxidation and minimal dissolution. For comparison, the stability test of 2000 potential cycles was conducted with a commercial 20 wt% Pt/C catalyst (E-TEK) and the $E_{1/2}$ value for the Pt/C dropped by about 32 mV [173].

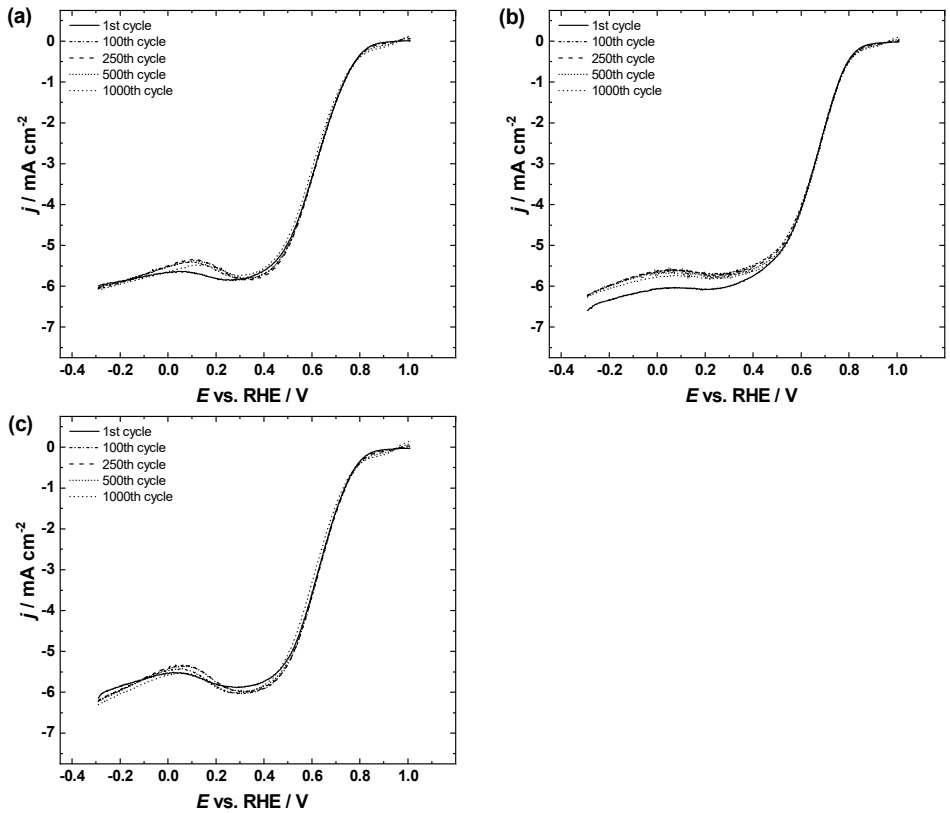

Figure 52. RDE polarisation curves for oxygen reduction on (a) 35, (b) 90, and (c) 120 nm AgNW catalysts in O_2-saturated 0.1 M KOH solution during the stability tests. ω = 1900 rpm, v = 10 mV s^{-1}.

6.10 Carbon support influence on dissolution stability of AgNPs

In the tenth part of the work, focus is on the dissolution part of the degradation of Ag-based catalysts (see sub-sections 5.1.6 and 6.6) in the ORR and the OER potential regions, and on how this dissolution affects the activity of the materials [X]. For this, both SFC (on-line) and RDE (off-line) methods were used while also employing ICP-MS. The Ag-based catalysts are prepared on mesoporous carbon (MC) support [174] and on conventional Vulcan carbon (VC). The Ag/MC catalyst showed higher stability at different electrochemical conditions than Ag/VC.

6.10.1 CV studies of Ag/MC and Ag/VC catalysts

Figure 53 shows a comparison of the first cyclic voltammograms for Ag/MC and Ag/VC obtained with the RDE tip using the same electrochemical *Protocol 2* (see sub-section 5.1.10) that was used in the SFC-ICP-MS measurements. The observed anodic peaks are labelled from A1 to A5, while the cathodic peaks are named from C1 to C3. On the one hand, the origin of the peaks A1 and A2, which correspond to the initial stages of silver oxidation, is not very clear. The peak A1 was ascribed to the dissolution of silver in the form of $Ag(OH)_2^-$ and the formation of a first monolayer of Ag_2O. Different origins of peak A2 were proposed: (i) the formation of Ag(OH), which in turn can dissolve in the form of $Ag(OH)_2^-$ or AgO^- ; (ii) the preferential oxidation of silver atoms with low coordination number; or (iii) the real completion of the Ag_2O monolayer.

In Figure 53a, the onset of anodic peak (A1) at 1.15 V vs. RHE represents formation of $Ag(OH)_2^-$ complexes for Ag/MC, and (A2) at 1.19 V vs. RHE represents AgOH formation and the beginning of Ag oxidation, during which Ag_2O film starts to form. Figure 53b shows that for Ag/VC the onset of anodic peak starts at 1.14 V vs. RHE, and at 1.2 V vs. RHE AgOH formation begins [102, 175]. A peak (A3) starting at 1.28 V vs. RHE, for Ag/MC, and at 1.27 V vs. RHE, for Ag/VC, represents the Ag_2O film growth via nucleation from supersaturated solution by a solid-state transport through the inner layers of Ag nanoparticles [102, 176, 177]. The peak (A4) at about 1.54 V vs. RHE, for Ag/MC, and 1.63 V vs. RHE, for Ag/VC, can be attributed to more oxidized Ag_2O_2, and the peak (A5) at about 1.8 V vs. RHE, for both Ag catalysts corresponds to Ag_2O_3, which is the highest silver oxide possible [102, 178-180]. Moving in the cathodic direction Ag oxides are reduced and dissolve in the form of $Ag(OH)_2^-/AgO^-$. Ag is already unstable at potentials higher than 1.2 V vs. RHE where Ag_2O starts to form. Each consecutive cycle, getting closer to 1.8 V vs. RHE, increases the amount of Ag oxidised and Ag oxidation level, and when Ag_2O_3 forms, catalyst surface passivates and Ag dissolution rate decreases. Moving back in the cathodic direction, reduction peaks of formed oxides can be observed. Peak C1 corresponds to the reduction of the highest oxides, i.e. Ag_2O_2 and Ag_2O_3. Peak C2 is related to the reduction of

Ag_2O/ AgOH and partial further reduction of previous higher Ag oxides [102]. At peak C3 slight oxygen reduction can be observed, since the CVs were recorded in static conditions and therefore there can be some O_2 remaining near the surface from the previous OER at peak A5 [63, 102, 181]. Correlations between the anodic and cathodic peaks described here with the dissolution processes will be established in the next section with the help of the on-line electrochemical ICP-MS measurements.

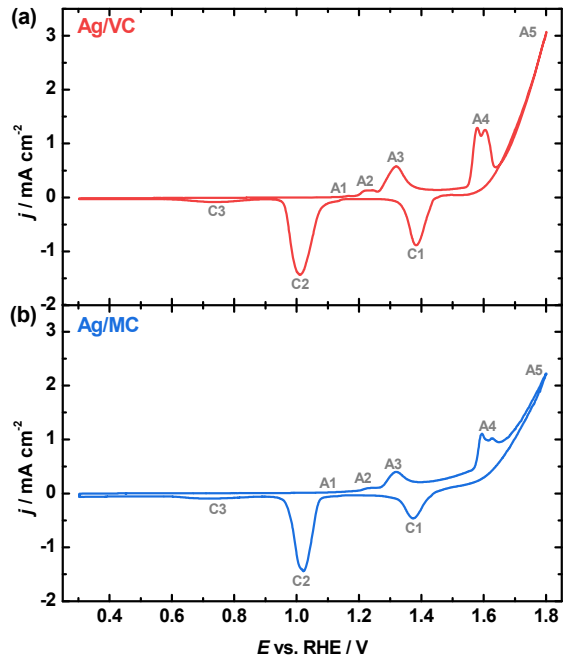

Figure 53. A comparison of the first CV of (a) Ag/VC and (b) Ag/MC for *Protocol 2*, in which the potential was cycled between 0.3 and 1.8 V vs. RHE; scan rate: 2 mV s^{-1}. The dashed and dotted lines indicate the onset potentials for the most relevant anodic and cathodic peaks, respectively (A2, A3, A5, C1 and C2).

6.10.2 Online SFC-ICP-MS studies on Ag/MC and Ag/VC

Figure 54 shows a comparison of the dissolution profiles of the Ag/MC and Ag/VC catalysts obtained by the SFC-ICP-MS technique using *Protocol 1* (see sub-section 5.1.10) to see how Ag oxidation and reduction affect Ag dissolution. The data presented in Figure 54 is normalised by the initial mass of Ag. Figure 54a represents the employed electrochemical protocol while Figure 54b displays the dissolution profiles for Ag/MC and Ag/VC catalysts. The first dissolution peak for both catalysts appears for the cycle with upper potential limit (E_{upper}) of 1.2 V, which would correspond to peak A2 in Figure 53 and therefore to the formation of $Ag(OH)_2^-$ and AgO^- dissolved species. For cycles with E_{upper} = 1.4 V or higher a second cathodic dissolution peak can be

observed, related to the reduction of the different Ag oxides, first to Ag_2O and for higher E_{upper} also Ag_2O_2 and Ag_2O_3. This points out that there is cathodic dissolution happening together with the (reduction) reactions involving the formation of $Ag(OH)_2^-$ and AgO^-. At the same time, the first anodic peak also increases as E_{upper} is increased, suggesting that also anodic dissolution occurs during the formation of the different Ag oxides. In only two double peaks, anodic and cathodic dissolution, can be clearly distinguished, which would comprise together all the anodic and cathodic processes, respectively. Therefore, to resolve the different dissolution reactions, *Protocol 2*, with a lower scan rate, was employed next. Second dissolution peak can be seen between 1.2 and 1.3 V (peak A2 in Figure 53), which corresponds to the AgOH formation. Third peak corresponds to Ag_2O formation and reduction (peak A3 in Figure 53). Fourth peak at about 1.4 V shows the beginning of Ag_2O_2 formation. Fifth dissolution peak at about 1.6 V corresponds to fully formed Ag_2O_2 (peak A4 in Figure 53). By the sixth dissolution peak at about 1.7 V Ag_2O_3 starts to form which momentarily reduces Ag dissolution rate separating the dissolution peak into the anodic and cathodic dissolution peaks. At the last peak at about 1.8 V Ag_2O_3 is fully formed, and the double peak (peak A5 in Figure 53) is even more expressed.

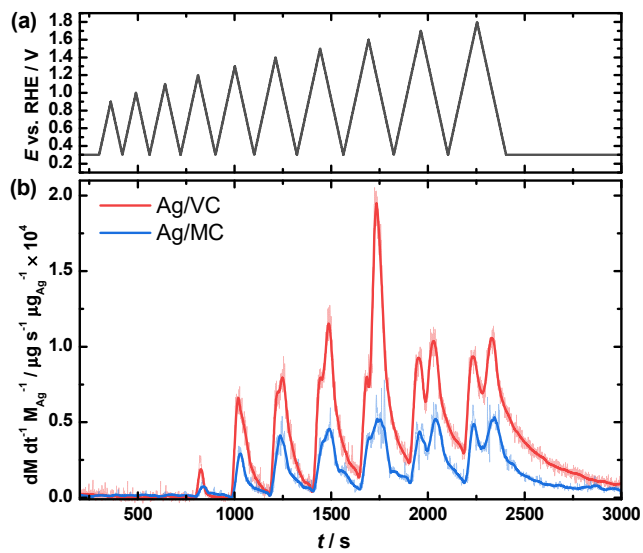

Figure 54. (a) Potential vs. time signal for *Protocol 1* and (b) dissolution profiles obtained with the SFC-ICP-MS technique for Ag/VC and Ag/MC catalyst materials.

Figure 55 shows the comparison of the dissolution profiles of the Ag/MC and Ag/VC catalysts obtained using the SFC-ICP-MS technique and *Protocol 2* (see sub-section 5.1.10) to better resolve different dissolution processes e.g. anodic (influenced by Ag oxidation) and cathodic (influenced by Ag oxides reduction) dissolution. The data presented in Figure 54 is normalised to the initial mass of

Ag. In the case of *Protocol 2* (see sub-section 5.1.10), the dissolution rate of Ag is already high during the first scanning cycle between 0.3 and 1.8 V vs. RHE for both Ag catalysts. However, Ag/MC shows slightly higher stability with an Ag dissolution rate of ca 1.02 μg Ag^{-1} s^{-1} as compared ca. 1.35 μg Ag^{-1} s^{-1} for Ag/VC. In addition, the dissolution rate during both cycles with either Ag catalyst stays the same. The onset of dissolution for both materials takes place at ca. 1.11 V and it is related to peaks A1 and A2 in the CVs (Figure 53), corresponding to the processes, in which the dissolved species $Ag(OH)_2^-$ and $AgO^-$are formed. After this first shoulder, another dissolution peak starts at ca. 1.4 V, coinciding with peak A3 for the formation of Ag_2O, during which still some anodic dissolution is occurring. This second peak reaches its maximum at ca. 1.65 V, corresponding to peak A4 for Ag_2O_2 formation. This means that once the Ag_2O_2 layer is formed the surface becomes passivated, and therefore the dissolution rate decreases while going to more positive potentials up to 1.8 V, where the highest oxide Ag_2O_3 forms, which also contributes to the passivation of the surface, although some dissolution occurs while it's formed as it can be seen by the apparition of a shoulder in the profile. During the negative going direction, cathodic dissolution starts at ca. 1.4 V, corresponding to the total reduction of the Ag_2O_3 and Ag_2O_2 layers (peak C1 in the CV curve), during which the release of AgO^- species can take place to some extent.

Finally, a further increase in the dissolution rate is observed at ca. 1.1 V, which coincides with peak C2, corresponding to the cathodic dissolution from the reduction of the Ag_2O layer. Cathodic dissolution is maximum at ca. 0.9 V, corresponding to the end of the reduction peak C2, and from this value the dissolution rate goes to zero, as the remaining surface Ag oxides are totally reduced. All the onset potentials for anodic and cathodic dissolution are marked with grey vertical lines in Figure 55. The discussion presented here is in agreement with the work by Schalenbach and co-workers, although in the latter case they only observed one anodic and one cathodic peak [181].

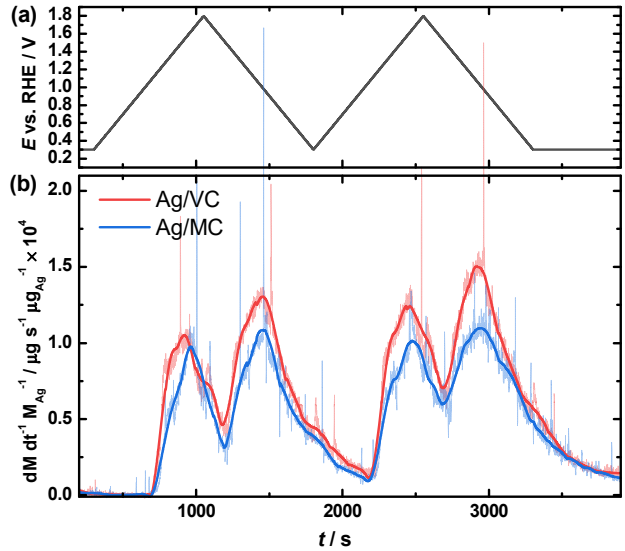

Figure 55. Potential vs. time signal for *Protocol 2* (top) and dissolution profiles obtained with the SFC-ICP-MS technique for Ag/VC and Ag/MC catalysts (bottom). The grey dashed and dotted lines denote the onset for the anodic and cathodic dissolution peaks, respectively.

Figures 56a and 56b show the integrated Ag dissolved amounts corresponding to the different upper potential limit for *Protocol 1* and the corresponding cycle for *Protocol 2*, respectively. When comparing Ag catalysts using *Protocol 1*, Ag from Ag catalyst Ag/MC dissolved 2-3 times less than from Ag/VC. Figure 55a shows that after the calculation of the integrated amounts of dissolved silver for each upper potential limit of Ag/VC catalyst, compared to Ag/MC, showed higher dissolved amounts of Ag already at 1.2 V vs. RHE. From Figure 55b, it can be clearly observed that after the calculation of the integrated amounts of dissolved silver during both cycles Ag/VC catalyst showed higher dissolution of Ag compared to Ag/MC.

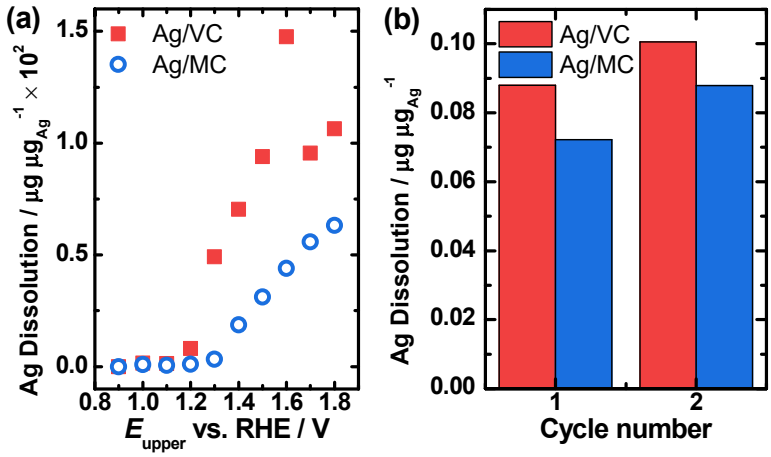

Figure 56. (a) Integrated amounts of dissolved silver vs. upper potential limit for *Protocol 1* and (b) integrated amounts of dissolved silver vs. cycle number for *Protocol 2* (right).

Figures 54, 55 and 56 show that the stability of both catalysts at 1.2 V vs. RHE is already compromised, and potential usage in, for example, unitized regenerative fuel cell (URFC) is questionable due to Ag catalyst's instability moving from the ORR potential region towards the OER potential region. Besides the OER potential window, where Ag dissolves, it was also important to investigate Ag stability in the ORR region of fuel cell mode by using RDE accelerated stress tests.

6.10.3 RDE accelerated stress tests

Accelerated stress tests with the working potentials up to 1.0 V vs. RHE were carried out with Ag/MC and Ag/VC catalysts to investigate the stability and activity changes during the ORR. A second set of experiments using an upper potential limit of 1.2 V vs. RHE was measured to test the Ag-based catalysts stability under harsher conditions, since appreciable Ag dissolution can be observed in Figure 54 at this potential. Incursions into OER potentials were discarded since dissolution rates are remarkably high at potentials higher than 1.5 V vs. RHE, as can be discerned from Figures 54 and 55. Additionally, solution samples were taken during the ASTs in order to evaluate the dissolved Ag amounts with the ICP-MS. Figures 57a and 57b represent the ORR curves within a potential range between 0.3 V and 1.0 V vs. RHE, and Figures 57c and 57d between potentials 0.3 V and 1.2 V vs. RHE, before and after a complete AST of 10,000 potential cycles in O_2-saturated 0.05 M KOH solution using a scan rate of 500 mV s^{-1}. Figures 57e and 57f depict the half-wave potentials before the AST, after the AST up to 1.0 V vs. RHE, and after the AST up to 1.2 V vs. RHE. As shown in Figure 57, for Ag/MC the half-wave potential

shifted only by about 11 mV while for Ag/VC the $E_{1/2}$ value decreased by about 51 mV. When the upper potential limit was raised to 1.2 V vs. RHE the value of $E_{1/2}$ shifted negative only by 30 mV for Ag/MC and 60 mV for Ag/VC catalyst. The negative half-wave potential shift for Ag/VC is almost double compared to that of Ag/MC. Therefore, the ORR activity results also indicate that Ag/MC is more stable than Ag/VC, and that Ag/MC resists better the more aggressive conditions.

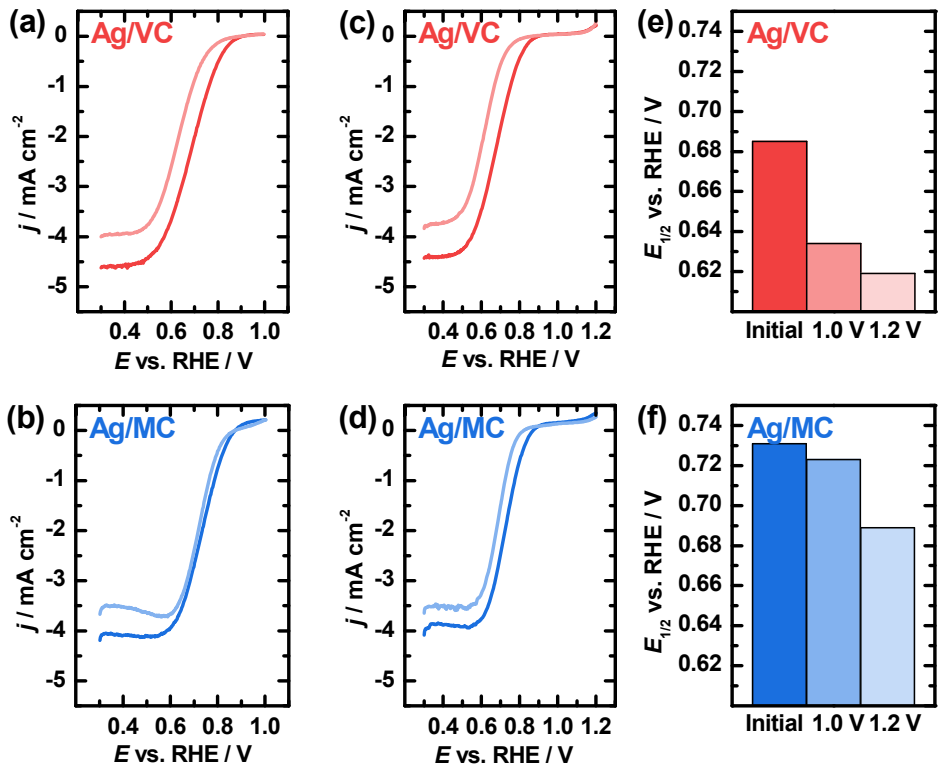

Figure 57. ORR polarization curves for (a, c) Ag/VC and (b, d) Ag/MC in O_2-saturated 0.05 M KOH before and after 10,000 potential cycles (500 mV s^{-1}) with upper potential limit of 1.0 and 1.2 V vs. RHE, ω = 960 rpm, v = 10 mV s^{-1}. $E_{1/2}$ values for (e) Ag/VC and (f) Ag/MC corresponding to the polarization curves before and after the AST up to 1.0 and 1.2 V vs. RHE.

6.10.4 RDE identical-location TEM (IL-TEM) measurements

The on-line and *ex situ* RDE dissolution measurements with ICP-MS showed that the Ag/MC material is more stable than the Ag/VC. This phenomenon was further investigated using RDE-IL-TEM measurements. These measurements can provide more information about the surface morphology changes of the electrocatalysts during the AST protocols for the ORR.

A catalyst ink was drop casted onto the TEM grid and the grid was imaged to find areas of interest (top row in Figure 58a-f). After that, the grid was placed back into the RDE holder, and was subjected to the first 500 cycles of AST. Then, the grid was removed from the holder and was remeasured with IL-TEM to observe changes in the catalyst morphology (centre row in Figure 58). The same procedure was repeated after subsequent 500 AST cycles (bottom row in Figure 58).

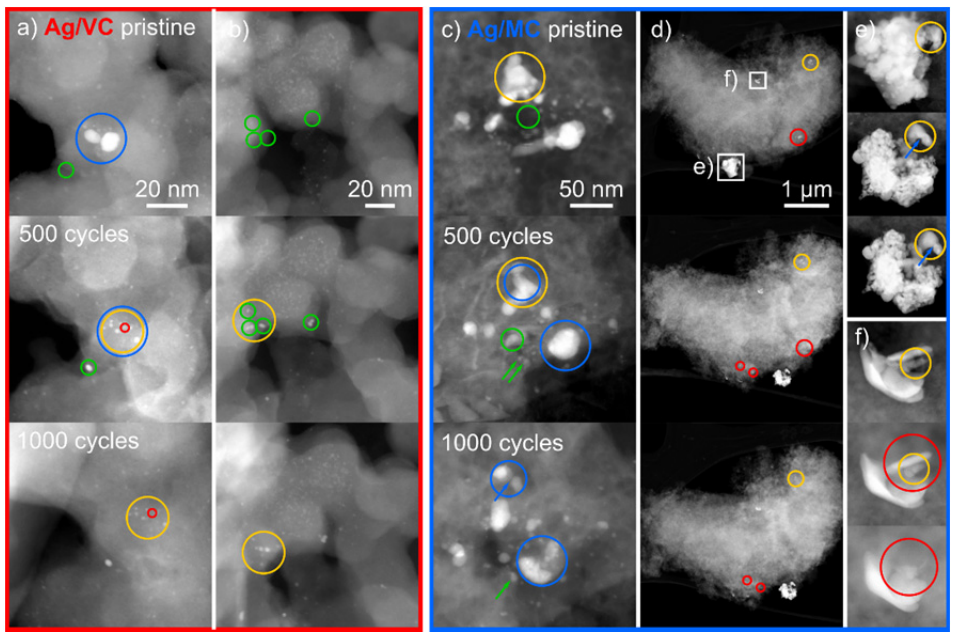

Figure 58. RDE-IL-TEM measurements for Ag/VC (a, b) and Ag/MC (c-f) for the pristine sample (top), the sample after 500 cycles of AST (centre), and after 1000 cycles of AST (bottom). Green circles: appearance of particles; yellow circles: diminution of size of particles; blue circles: splitting of particles into smaller ones; red circles: disappearance of particles.

For the Ag/VC material, some initial AgNPs continuously decreased in size (yellow circles). The green circles show the appearance of new smaller nanoparticles, which represent some redeposited AgNPs which may originate from the previously dissolved particles.

Regarding the Ag/MC material, the red circles highlight AgNPs disappearance during the AST protocol. The regions where the initial AgNPs reduce their size are shown in yellow circles and the new AgNPs appearance/growth in green circles, which is analogous to the case of the Ag/VC catalyst. Either Ostwald ripening or redeposition could be the reason to the initial AgNPs growth from the adjacent particles dissolved (green arrows). In the blue circle, a

region in which the splitting of the big nanoparticles into smaller ones occur in parallel is shown. This phenomenon seems to be more pronounced at grain boundaries (blue arrows). During the investigation of the Ag/MC material, attention has been given to the borders of the initial and the new AgNPs since it is difficult to extract clear conclusions from the regions inside the carbon support because the focus planes might be different.

The RDE-IL-TEM results clearly show that some of the dissolved AgNPs redeposit onto both carbon supports. The loss of activity for Ag/VC catalyst could come from the notable Ostwald ripening, which causes, after losing a high number of smaller particles, the remaining AgNPs to grow considerably bigger in size, and consequent reduction of the electroactive surface area of the catalyst after the AST. For the Ag/MC catalyst, the loss of AgNPs is lower due to the lower degree of Ostwald ripening and the initially higher number of very small AgNPs. Because of high redeposition, the dissolution of these small particles would affect the Ag/MC electrocatalytic activity less. It can be observed that despite the smaller size of the AgNPs for Ag/MC, a high number of very small AgNPs remain almost the same, probably due to the stabilization effect of the nitrogen sites to the small Ag atomic clusters. In a recent work by Shi and co-workers 1.7 nm Ag nanoclusters with adatoms were synthesised as highly active catalysts for the ORR and they found that after 22 hours of accelerated durability test some of the Ag nanoclusters had slightly grown and that the XPS results showed no Ag oxidation after the test [182].

7. SUMMARY

This PhD thesis evaluated Ag-based catalyst electrocatalytic activity towards the oxygen reduction reaction in an alkaline environment. For this purpose, nanostructured materials were synthesised and studied primarily as cathode catalyst materials for a low-temperature fuel cell. The main goal was to study the effect of the Ag nanoparticle synthesis method and a catalyst substrate on the ORR kinetic parameters, for example, mass and specific activities. In addition to electrochemical methods, different physical methods: TEM, SEM, XRD, XPS, and others, were applied to study the catalyst materials. Ag-based catalysts were prepared onto different carbon substrates using various electrochemical, chemical, and physical deposition methods.

In the first three parts of the thesis, Ag particles were prepared using the electrochemical deposition method, whereby in parts one and two Ag particles were prepared using the same electrochemical procedure. More specifically, Ag particles were deposited onto clean, glassy carbon electrodes, and Ag deposition times were varied. Ag was deposited in the former from an aqueous solution [I], and in the latter, from a non-aqueous acetonitrile solution [II]. Moreover, in part one, smaller up to 50 nm particles with some large agglomerates were obtained. In part two, Ag particles were somewhat bigger than 90 nm, and no agglomerates were observed. These results indicate that mass and specific activities did not depend on deposition times. In part three, Ag particles were electrodeposited onto four nanocarbon supports using two different deposition procedures. Independent of the deposition procedure, Ag nanoparticles prepared onto nitrogen-doped graphene oxide showed the highest mass activities. The higher activity might come from the interaction between Ag nanoparticles and nitrogen species on the carbon substrate [III].

In parts four, five, and six, Ag nanoparticles were deposited onto different high-surface area nanocarbon substrates using various chemical deposition methods. In part four, Ag catalysts were prepared onto two carbide-derived carbon substrates with a higher specific surface area than conventional Vulcan XC-72R carbon. Catalysts prepared onto carbide-derived carbons showed many times higher mass activities compared to the catalyst prepared onto the conventional carbon support [IV]. In part five, Ag nanoparticles were deposited onto nitrogen-doped graphene oxide using three different deposition protocols. During the synthesis of the catalysts, the employed reducing agent strongly affected the Ag nanoparticle size and distribution, changing the ORR activities of the Ag catalysts. The electrocatalytic activity of the catalysts also depended on the interaction between the nitrogen species on the carbon support and Ag nanoparticles [V]. In part six, Ag catalysts were prepared onto two commercially available nitrogen-containing mesoporous carbon supports (Pajarito Powder, LLC) using two different deposition procedures. The reducing agents in both cases yielded Ag nanoparticles with similar Ag crystallite sizes between 19 and 28 nm. The obtained mass activities depended mainly on the employed

carbon support and were considerably higher on the mesoporous carbon than conventional Vulcan carbon. Best catalyst materials were tested in an anion exchange membrane fuel cell, where a maximum power density of 310 mW cm^{-2} was obtained which was only somewhat lower than that of commercial Pt/C (347 mW cm^{-2}) [VI].

In parts seven and eight, Ag catalysts were prepared using physical deposition methods. In the former, Ag was deposited onto two differently synthesised MnO_2_MWCNT substrates using the magnetron sputtering method, whereby the main variables of this kind of nanocomposite are the type of synthesised manganese oxides and their binding to the surface of the carbon support and Ag [VII]. In the latter, thin Ag films were prepared using the electron beam evaporation method, where the nominal thickness of the Ag film was varied. The effect of the Ag film's thickness on the electrocatalytic properties of the ORR was studied. The results indicate that, approximately 1 nm Ag layers already showed high electrocatalytic activity [VIII].

In part nine, commercially available silver nanowires were tested. Nanowires possess one measure that is in nanoscale, which makes the studies of their electrocatalytic properties important. The diameters of the studied Ag nanowires were 35, 90, and 120 nm. Ag nanowires with the smallest diameter showed the highest electrocatalytic activity [IX]. In part ten, Ag dissolution effects on the Ag-based catalysts' stability were studied. According to the results, nitrogen-containing mesoporous carbons are more suitable as catalyst supports than conventional Vulcan carbon because the amount of dissolved Ag was smaller when Ag was deposited onto the mesoporous carbon [X].

In conclusion, the ORR on silver-based catalysts follow an overall four-electron pathway, producing only water and essentially no intermediate hydrogen peroxide. Based on the obtained Tafel slope values, it is reasonable to argue that the ORR rate-determining step is the sluggish transfer of the first electron to the oxygen molecule. Consequently, Ag-based nanostructured catalyst materials can be considered suitable as cathode catalysts for low-temperature anion exchange membrane fuel cells.

8. REFERENCES

[1] H. Erikson, A. Sarapuu, K. Tammeveski, Oxygen Reduction Reaction on Silver Catalysts in Alkaline Media: a Minireview, Chemelectrochem 6(1) (2019) 73–86.

[2] I. Katsounaros, S. Cherevko, A.R. Zeradjanin, K.J. Mayrhofer, Oxygen electrochemistry as a cornerstone for sustainable energy conversion, Angewandte Chemie International Edition 53(1) (2014) 102.

[3] M.H. Shao, Q.W. Chang, J.P. Dodelet, R. Chenitz, Recent Advances in Electrocatalysts for Oxygen Reduction Reaction, Chemical Reviews 116(6) (2016) 3594–3657.

[4] X. Ge, A. Sumboja, D. Wuu, T. An, B. Li, F.W.T. Goh, T.S.A. Hor, Y. Zong, Z. Liu, Oxygen Reduction in Alkaline Media: From Mechanisms to Recent Advances of Catalysts, ACS Catalysis 5(8) (2015) 4643–4667.

[5] J.S. Spendelow, A. Wieckowski, Electrocatalysis of oxygen reduction and small alcohol oxidation in alkaline media, Physical Chemistry Chemical Physics 9(21) (2007) 2654–2675.

[6] N.A. Shumilova, G.V. Zhutaeva, M. Tarasevich, Oxygen ionization on silver in alkaline solutions, Electrochimica Acta 11(8) (1966) 967–974.

[7] L. Genies, Y. Bultel, R. Faure, R. Durand, Impedance study of the oxygen reduction reaction on platinum nanoparticles in alkaline media, Electrochimica Acta 48(25) (2003) 3879–3890.

[8] R. Cao, J.-S. Lee, M. Liu, J. Cho, Recent Progress in Non-Precious Catalysts for Metal-Air Batteries, Advanced Energy Materials 2(7) (2012) 816–829.

[9] F.D. Sanij, P. Balakrishnan, P. Leung, A. Shah, H. Su, Q. Xu, Advanced Pd-based nanomaterials for electro-catalytic oxygen reduction in fuel cells: A review, International Journal of Hydrogen Energy 46(27) (2021) 14596–14627.

[10] N.M. Markovic, T.J. Schmidt, V. Stamenkovic, P.N. Ross, Oxygen Reduction Reaction on Pt and Pt Bimetallic Surfaces: A Selective Review, Fuel Cells 1(2) (2001) 105–116.

[11] S. Sui, X. Wang, X. Zhou, Y. Su, S. Riffat, C.-j. Liu, A comprehensive review of Pt electrocatalysts for the oxygen reduction reaction: Nanostructure, activity, mechanism and carbon support in PEM fuel cells, Journal of Materials Chemistry A 5(5) (2017) 1808–1825.

[12] B.B. Blizanac, P.N. Ross, N.M. Markovic, Oxygen electroreduction on Ag(111): The pH effect, Electrochimica Acta 52(6) (2007) 2264–2271.

[13] P. Singh, D.A. Buttry, Comparison of Oxygen Reduction Reaction at Silver Nanoparticles and Polycrystalline Silver Electrodes in Alkaline Solution, Journal of Physical Chemistry C 116(19) (2012) 10656–10663.

[14] X. Cheng, Z. Shi, N. Glass, L. Zhang, J. Zhang, D. Song, Z.-S. Liu, H. Wang, J. Shen, A review of PEM hydrogen fuel cell contamination: Impacts, mechanisms, and mitigation, Journal of Power Sources 165(2) (2007) 739–756.

[15] M. Chatenet, L. Genies-Bultel, M. Aurousseau, R. Durand, F. Andolfatto, Oxygen reduction on silver catalysts in solutions containing various concentrations of sodium hydroxide – comparison with platinum, Journal of Applied Electrochemistry 32(10) (2002) 1131–1140.

[16] S.Z. Liu, M.G. White, P. Liu, Oxygen Reduction Reaction on Ag(111) in Alkaline Solution: A Combined Density Functional Theory and Kinetic Monte Carlo Study, Chemcatchem 10(3) (2018) 540–549.

[17] H.A. Hansen, J. Rossmeisl, J.K. Norskov, Surface Pourbaix diagrams and oxygen reduction activity of Pt, Ag and Ni(111) surfaces studied by DFT, Physical Chemistry Chemical Physics 10(25) (2008) 3722–3730.
[18] J. Greeley, I.E.L. Stephens, A.S. Bondarenko, T.P. Johansson, H.A. Hansen, T.F. Jaramillo, J. Rossmeisl, I. Chorkendorff, J.K. Nørskov, Alloys of platinum and early transition metals as oxygen reduction electrocatalysts, Nature Chemistry 1(7) (2009) 552–556.
[19] Y. Li, H. Dai, Recent advances in zinc–air batteries, Chemical Society Reviews 43(15) (2014) 5257–5275.
[20] Y. Zhou, Q. Lu, Z. Zhuang, G.S. Hutchings, S. Kattel, Y. Yan, J.G. Chen, J.Q. Xiao, F. Jiao, Oxygen Reduction at Very Low Overpotential on Nanoporous Ag Catalysts, Advanced Energy Materials 5(13) (2015) 1500149.
[21] A.E.S. Sleightholme, J.R. Varcoe, A.R. Kucernak, Oxygen reduction at the silver/ hydroxide-exchange membrane interface, Electrochemistry Communications 10(1) (2008) 151–155.
[22] B.B. Blizanac, P.N. Ross, N.M. Markovic, Oxygen reduction on silver low-index single-crystal surfaces in alkaline solution: Rotating ring Disk(Ag(hkl)) studies, Journal of Physical Chemistry B 110(10) (2006) 4735–4741.
[23] K. Nubla, N. Sandhyarani, Ag nanoparticles anchored Ag2WO4 nanorods: An efficient methanol tolerant and durable Pt free electro-catalyst toward oxygen reduction reaction, Electrochimica Acta 340 (2020) 135942.
[24] N. Zhang, F. Chen, D. Liu, Z. Xia, Electrochemical Oxygen Reduction Reaction in Alkaline Solution at a Low Overpotential on (220)-Textured Ag Surface, ACS Applied Energy Materials 1(8) (2018) 4385–4394.
[25] J.J. Hinsch, J. Liu, J.J. White, Y. Wang, The Role of Steps on Silver Nanoparticles in Electrocatalytic Oxygen Reduction, Catalysts 12(6) (2022) 576.
[26] Y.Y. Deng, H.D. Liu, X.J. Wei, L.L. Ding, F.H. Jiang, X.Q. Cao, Q.F. Zhou, M. Xiang, J.R. Bai, H.W. Gu, One-dimensional nitrogen-doped carbon frameworks embedded with zinc-cobalt nanoparticles for efficient overall water splitting, Journal of Colloid and Interface Science 585 (2021) 800–807.
[27] Q.Y. Wang, X.Q. Cui, W.M. Guan, L. Zhang, X.F. Fan, Z. Shi, W.T. Zheng, Shape-dependent catalytic activity of oxygen reduction reaction (ORR) on silver nanodecahedra and nanocubes, Journal of Power Sources 269 (2014) 152–157.
[28] C.L. Lee, C.C. Syu, Electrochemical growth and oxygen reduction property of Ag nanosheet arrays on a Ti/TiO2 electrode, International Journal of Hydrogen Energy 36(23) (2011) 15068–15074.
[29] C.L. Lee, H.P. Chiou, C.M. Syu, C.C. Wu, Silver triangular nanoplates as electrocatalyst for oxygen reduction reaction, Electrochemistry Communications 12(11) (2010) 1609–1613.
[30] Q. Wu, P. Diao, J. Sun, T. Jin, D. Xu, M. Xiang, Electrodeposition of Vertically Aligned Silver Nanoplate Arrays on Indium Tin Oxide Substrates, The Journal of Physical Chemistry C 119(35) (2015) 20709–20720.
[31] V.V. Novikova, S.P. Starodubova, M.Y. Chaika, T.A. Kravchenko, Electroreduction of molecular oxygen on carbon electrode modified by dispersed silver, Russian Journal of Electrochemistry 49(3) (2013) 278–284.
[32] Y.F. Yang, Y.H. Zhou, Particle-size effects for oxygen reduction on dispersed silver plus carbon electrodes in alkaline-solution, Journal of Electroanalytical Chemistry 397(1–2) (1995) 271–278.

[33] J.J. Han, N. Li, T.Y. Zhang, Ag/C nanoparticles as an cathode catalyst for a zinc-air battery with a flowing alkaline electrolyte, Journal of Power Sources 193(2) (2009) 885–889.
[34] Y.J. Chao, Y.P. Lyu, Z.W. Wu, C.L. Lee, Seed-mediated growth of Ag nanocubes and their size-dependent activities toward oxygen reduction reaction, International Journal of Hydrogen Energy 41(6) (2016) 3896–3903.
[35] Y.Z. Lu, W. Chen, Size effect of silver nanoclusters on their catalytic activity for oxygen electro-reduction, Journal of Power Sources 197 (2012) 107–110.
[36] T. Wang, M. Kaempgen, P. Nopphawan, G. Wee, S. Mhaisalkar, M. Srinivasan, Silver nanoparticle-decorated carbon nanotubes as bifunctional gas-diffusion electrodes for zinc-air batteries, Journal of Power Sources 195(13) (2010) 4350–4355.
[37] S.M. Alia, K. Duong, T. Liu, K. Jensen, Y.S. Yan, Supportless Silver Nanowires as Oxygen Reduction Reaction Catalysts for Hydroxide-Exchange Membrane Fuel Cells, Chemsuschem 5(8) (2012) 1619–1624.
[38] D. Šepa, M. Vojnovíc, A. Damjanovic, Oxygen reduction at silver electrodes in alkaline solutions, Electrochimica Acta 15(8) (1970) 1355–1366.
[39] J. Ohyama, Y. Okata, N. Watabe, M. Katagiri, A. Nakamura, H. Arikawa, K. Shimizu, T. Takeguchi, W. Ueda, A. Satsuma, Oxygen reduction reaction over silver particles with various morphologies and surface chemical states, Journal of Power Sources 245 (2014) 998–1004.
[40] F. Bidault, A. Kucernak, A novel cathode for alkaline fuel cells based on a porous silver membrane, Journal of Power Sources 195(9) (2010) 2549–2556.
[41] F. Bidault, A. Kucernak, Cathode development for alkaline fuel cells based on a porous silver membrane, Journal of Power Sources 196(11) (2011) 4950–4956.
[42] A. Treshchalov, H. Erikson, L. Puust, S. Tsarenko, R. Saar, A. Vanetsev, K. Tammeveski, I. Sildos, Stabilizer-free silver nanoparticles as efficient catalysts for electrochemical reduction of oxygen, Journal of Colloid and Interface Science 491 (2017) 358–366.
[43] L.W. Zhang, Q.Q. Guo, R. Pitcheri, Y. Fu, J.S. Li, Y.J. Qiu, Silver nanofibers with controllable microstructure and crystal facet as highly efficient and methanol-tolerant oxygen reduction electrocatalyst, Journal of Power Sources 413 (2019) 233–240.
[44] Y. Yang, D. Pan, J. Li, M. Jonsson, P. Jannasch, I.L. Soroka, Using an ionomer as a size regulator in γ-radiation induced synthesis of Ag nanocatalysts for oxygen reduction reaction in alkaline solution, Journal of Colloid and Interface Science 646 (2023) 381–390.
[45] L. Tammeveski, H. Erikson, A. Sarapuu, J. Kozlova, P. Ritslaid, V. Sammelselg, K. Tammeveski, Electrocatalytic oxygen reduction on silver nanoparticle/multi-walled carbon nanotube modified glassy carbon electrodes in alkaline solution, Electrochemistry Communications 20 (2012) 15–18.
[46] I. Kruusenberg, J. Leis, M. Arulepp, K. Tammeveski, Oxygen reduction on carbon nanomaterial-modified glassy carbon electrodes in alkaline solution, Journal of Solid State Electrochemistry 14(7) (2010) 1269–1277.
[47] K. Tammeveski, K. Kontturi, R.J. Nichols, R.J. Potter, D.J. Schiffrin, Surface redox catalysis for O-2 reduction on quinone-modified glassy carbon electrodes, Journal of Electroanalytical Chemistry 515(1–2) (2001) 101–112.
[48] J. Lilloja, E. Kibena-Põldsepp, M. Merisalu, P. Rauwel, L. Matisen, A. Niilisk, E.S.F. Cardoso, G. Maia, V. Sammelselg, K. Tammeveski, An Oxygen Reduction

Study of Graphene-Based Nanomaterials of Different Origin, Catalysts 6(7) (2016) 108.
[49] L.Z. Yuan, L.H. Jiang, J. Liu, Z.X. Xia, S.L. Wang, G.Q. Sun, Facile synthesis of silver nanoparticles supported on three dimensional graphene oxide/carbon black composite and its application for oxygen reduction reaction, Electrochimica Acta 135 (2014) 168–174.
[50] M. Vikkisk, I. Kruusenberg, U. Joost, E. Shulga, I. Kink, K. Tammeveski, Electrocatalytic oxygen reduction on nitrogen-doped graphene in alkaline media, Applied Catalysis B-Environmental 147 (2014) 369–376.
[51] Z.S. Hou, Y.Q. Jin, X. Xi, T. Huang, D.Q. Wu, P.M. Xu, R.L. Liu, Hierarchically porous nitrogen-doped graphene aerogels as efficient metal-free oxygen reduction catalysts, Journal of Colloid and Interface Science 488 (2017) 317–321.
[52] C. Cao, L.L. Wei, M. Su, G. Wang, J.Q. Shen, Template-free and one-pot synthesis of N-doped hollow carbon tube @ hierarchically porous carbon supporting homogeneous AgNPs for robust oxygen reduction catalyst, Carbon 112 (2017) 27–36.
[53] D.B. Yu, J.F. Yao, L. Qiu, Y.Z. Wu, L.X. Li, Y. Feng, Q. Liu, D. Li, H.T. Wang, The synergetic effect of N-doped graphene and silver nanowires for high electrocatalytic performance in the oxygen reduction reaction, Rsc Advances 3(29) (2013) 11552–11555.
[54] R.F. Zhou, S.Z. Qiao, Silver/Nitrogen-Doped Graphene Interaction and Its Effect on Electrocatalytic Oxygen Reduction, Chemistry of Materials 26(20) (2014) 5868–5873.
[55] S. Jin, M. Chen, H. Dong, B. He, H. Lu, L. Su, W. Dai, Q. Zhang, X. Zhang, Stable silver nanoclusters electrochemically deposited on nitrogen-doped graphene as efficient electrocatalyst for oxygen reduction reaction, Journal of Power Sources 274 (2015) 1173–1179.
[56] X.H. Xu, C. Tan, H.J. Liu, F. Wang, Z.L. Li, J.J. Liu, J. Ji, Carbon black supported ultra-high loading silver nanoparticle catalyst and its enhanced electrocatalytic activity towards oxygen reduction reaction in alkaline medium, Journal of Electroanalytical Chemistry 696 (2013) 9–14.
[57] E.J. Lim, S.M. Choi, M.H. Seo, Y. Kim, S. Lee, W.B. Kim, Highly dispersed Ag nanoparticles on nanosheets of reduced graphene oxide for oxygen reduction reaction in alkaline media, Electrochemistry Communications 28 (2013) 100–103.
[58] R.Z. Jiang, E. Moton, J.P. McClure, Z. Bowers, A Highly Active and Alcohol-Tolerant Cathode Electrocatalyst Containing Ag Nanoparticles Supported on Graphene, Electrochimica Acta 127 (2014) 146–152.
[59] M. Vega-Cartagena, A. Rojas-Pérez, G.S. Colón-Quintana, D.A. Blasini Pérez, A. Peña-Duarte, E. Larios-Rodríguez, M.A. De Jesús, C.R. Cabrera, Potential dependent Ag nanoparticle electrodeposition on Vulcan XC-72R carbon support for alkaline oxygen reduction reaction, Journal of Electroanalytical Chemistry 891 (2021) 115242.
[60] X.A. Yang, L.F. Gan, C.Z. Zhu, B.H. Lou, L. Han, J. Wang, E.K. Wang, A dramatic platform for oxygen reduction reaction based on silver nanoclusters, Chemical Communications 50(2) (2014) 234–236.
[61] F.W. Campbell, S.R. Belding, R. Baron, L. Xiao, R.G. Compton, Hydrogen Peroxide Electroreduction at a Silver-Nanoparticle Array: Investigating Nanoparticle Size and Coverage Effects, The Journal of Physical Chemistry C 113(21) (2009) 9053–9062.

[62] C.C.M. Neumann, E. Laborda, K. Tschulik, K.R. Ward, R.G. Compton, Performance of silver nanoparticles in the catalysis of the oxygen reduction reaction in neutral media: Efficiency limitation due to hydrogen peroxide escape, Nano Research 6(7) (2013) 511–524.
[63] J.S. Guo, A. Hsu, D. Chu, R.R. Chen, Improving Oxygen Reduction Reaction Activities on Carbon-Supported Ag Nanoparticles in Alkaline Solutions, Journal of Physical Chemistry C 114(10) (2010) 4324–4330.
[64] A.C. Garcia, L.H.S. Gasparotto, J.F. Gomes, G. Tremiliosi-Filho, Straightforward Synthesis of Carbon-Supported Ag Nanoparticles and Their Application for the Oxygen Reduction Reaction, Electrocatalysis 3(2) (2012) 147–152.
[65] L. Demarconnay, C. Coutanceau, J.M. Leger, Electroreduction of dioxygen (ORR) in alkaline medium on Ag/C and Pt/C nanostructured catalysts - effect of the presence of methanol, Electrochimica Acta 49(25) (2004) 4513–4521.
[66] S. Maheswari, P. Sridhar, S. Pitchumani, Carbon-Supported Silver as Cathode Electrocatalyst for Alkaline Polymer Electrolyte Membrane Fuel Cells, Electrocatalysis 3(1) (2012) 13–21.
[67] B. Liu, M. Wang, Preparation and characterization of size-controlled silver nanoparticles decorated multi-walled carbon nanotubes and their electrocatalytic reduction properties for hydrogen peroxide, Russian Journal of Electrochemistry 50(5) (2014) 476–481.
[68] Y.-S. Wu, Z.-T. Liu, T.-P. Wang, S.-Y. Hsu, C.-L. Lee, A comparison of nitrogen-doped sonoelectrochemical and chemical graphene nanosheets as hydrogen peroxide sensors, Ultrasonics Sonochemistry 42 (2018) 659–664.
[69] Z.-T. Liu, J.-S. Ye, S.-Y. Hsu, C.-L. Lee, A sonoelectrochemical preparation of graphene nanosheets with graphene quantum dots for their use as a hydrogen peroxide sensor, Electrochimica Acta 261 (2018) 530–536.
[70] S. Ni, H. Zhang, Y. Zhao, X. Li, Y. Sun, J. Qian, Q. Xu, P. Gao, D. Wu, K. Kato, M. Yamauchi, Y. Sun, Single atomic Ag enhances the bifunctional activity and cycling stability of MnO2, Chemical Engineering Journal 366 (2019) 631–638.
[71] L. Wang, D. Kong, F. Chen, L. Cui, Y. Cai, H. Wang, X. Zhong, Y. Huang, Q. Li, Z. Ma, S. Hu, Strongly Coupled MnO2 Nanosheets/Silver Nanoparticles Hierarchical Spheres for Efficient Oxygen Reduction Reaction Electrocatalysis, Energy & Fuels 35(20) (2021) 16829–16836.
[72] H. Sun, Z. Hu, C. Yao, J. Yu, Z. Du, Silver Doped Amorphous MnO2 as Electrocatalysts for Oxygen Reduction Reaction in Al-Air Battery, Journal of The Electrochemical Society 167(8) (2020) 080539.
[73] J.A. Zamora Zeledón, G.T.K.K. Gunasooriya, G.A. Kamat, M.E. Kreider, M. Ben-Naim, M.A. Hubert, J.E. Avilés Acosta, J.K. Nørskov, M.B. Stevens, T.F. Jaramillo, Engineering metal–metal oxide surfaces for high-performance oxygen reduction on Ag–Mn electrocatalysts, Energy & Environmental Science 15(4) (2022) 1611–1629.
[74] D.A. Slanac, A. Lie, J.A. Paulson, K.J. Stevenson, K.P. Johnston, Bifunctional Catalysts for Alkaline Oxygen Reduction Reaction via Promotion of Ligand and Ensemble Effects at Ag/MnOx Nanodomains, Journal of Physical Chemistry C 116(20) (2012) 11032–11039.
[75] J. Liu, J. Liu, W. Song, F. Wang, Y. Song, The role of electronic interaction in the use of Ag and Mn3O4 hybrid nanocrystals covalently coupled with carbon as advanced oxygen reduction electrocatalysts, Journal of Materials Chemistry A 2(41) (2014) 17477–17488.

[76] P. Akbarian, M. Kheirmand, M. Faraji, Facile electrochemical fabrication of high-performance graphene quantum dots-supported Mn3O4/Ag hybrid catalyst for oxygen reduction reaction in alkaline media, International Journal of Energy Research 46(15) (2022) 23004–23019.
[77] W.S. Hummers, Jr., R.E. Offeman, Preparation of Graphitic Oxide, Journal of the American Chemical Society 80(6) (1958) 1339–1339.
[78] N. Alexeyeva, K. Tammeveski, Electrochemical reduction of oxygen on multi-walled carbon nanotube modified glassy carbon electrodes in acid media, Electrochemical and Solid State Letters 10(5) (2007) F18-F21.
[79] M. Käärik, M. Arulepp, M. Kook, U. Maeorg, J. Kozlova, V. Sammelselg, A. Perkson, J. Leis, Characterisation of steam-treated nanoporous carbide-derived carbon of TiC origin: structure and enhanced electrochemical performance, Journal of Porous Materials 25(4) (2018) 1057–1070.
[80] J.H. Zeng, J. Yang, J.Y. Lee, W.J. Zhou, Preparation of carbon-supported core-shell Au-Pt nanoparticles for methanol oxidation reaction: The promotional effect of the Au core, Journal of Physical Chemistry B 110(48) (2006) 24606–24611.
[81] A. Fazil, R. Chetty, Synthesis and Evaluation of Carbon Nanotubes Supported Silver Catalyst for Alkaline Fuel Cell, Electroanalysis 26(11) (2014) 2380–2387.
[82] Y. Tian, F.L. Wang, Y.X. Liu, F. Pang, X. Zhang, Green synthesis of silver nanoparticles on nitrogen-doped graphene for hydrogen peroxide detection, Electrochimica Acta 146 (2014) 646–653.
[83] Q.S. Fu, W.G. Qu, H.X. Gao, L.B. Xiao, S.Y. Niu, F.Q. Zhao, Y.Q. Xue, Investigation of the size- and morphology-dependence of surface thermodynamic properties of nano-silver, Journal of Physics and Chemistry of Solids 146 (2020) 109617.
[84] A. Roy, A. Ray, S. Saha, M. Ghosh, T. Das, M. Nandi, G. Lal, S. Das, Influence of electrochemical active surface area on the oxygen evolution reaction and energy storage performance of MnO2-multiwalled carbon nanotube composite, International Journal of Energy Research 45(11) (2021) 16908–16921.
[85] Y. Chen, Y. Zhang, D. Geng, R. Li, H. Hong, J. Chen, X. Sun, One-pot synthesis of MnO2/graphene/carbon nanotube hybrid by chemical method, Carbon 49(13) (2011) 4434–4442.
[86] M. He, Z. Turup, X. Jin, F. Chen, Ag nanoparticle-loaded to MnO2 with rich oxygen vacancies and Mn3+ for the synergistically enhanced oxygen reduction reaction, International Journal of Hydrogen Energy (2023) 283.
[87] K. Jukk, J. Kozlova, P. Ritslaid, V. Sammelselg, N. Alexeyeva, K. Tammeveski, Sputter-deposited Pt nanoparticle/multi-walled carbon nanotube composite catalyst for oxygen reduction reaction, Journal of Electroanalytical Chemistry 708 (2013) 31–38.
[88] S. Hussain, H. Erikson, N. Kongi, A. Tarre, P. Ritslaid, M. Rähn, L. Matisen, M. Merisalu, V. Sammelselg, K. Tammeveski, Pt nanoparticles sputter-deposited on TiO2/MWCNT composites prepared by atomic layer deposition: Improved electrocatalytic activity towards the oxygen reduction reaction and durability in acid media, International Journal of Hydrogen Energy 43(10) (2018) 4967–4977.
[89] S. Brunauer, P.H. Emmett, E. Teller, Adsorption of Gases in Multimolecular Layers, Journal of the American Chemical Society 60(2) (1938) 309–319.
[90] R.E. Davis, G.L. Horvath, C.W. Tobias, The solubility and diffusion coefficient of oxygen in potassium hydroxide solutions, Electrochimica Acta 12(3) (1967) 287–297.

[91] D.R. Lide, CRC Handbook of Chemistry and Physics, 82nd ed., CRC Press, Boca Raton, 2001.
[92] M. Mooste, E. Kibena-Põldsepp, V. Vassiljeva, A. Kikas, M. Käärik, J. Kozlova, V. Kisand, M. Külaviir, S. Cavaliere, J. Leis, A. Krumme, V. Sammelselg, S. Holdcroft, K. Tammeveski, Electrospun Polyacrylonitrile-Derived Co or Fe Containing Nanofibre Catalysts for Oxygen Reduction Reaction at the Alkaline Membrane Fuel Cell Cathode, ChemCatChem 12(18) (2020) 4568–4581.
[93] L.T. Pu, K.X. Li, Z.H. Chen, P. Zhang, X. Zhang, Z. Fu, Silver electrodeposition on the activated carbon air cathode for performance improvement in microbial fuel cells, Journal of Power Sources 268 (2014) 476–481.
[94] I. Boskovic, S.V. Mentus, M. Pjescic, Electrochemical behavior of an Ag/TiO2 composite surfaces, Electrochimica Acta 51(14) (2006) 2793–2799.
[95] G.K.H. Wiberg, K.J.J. Mayhofer, M. Arenz, Investigation of the Oxygen Reduction Activity of non-Platinum Catalysts – a RDE Methodology, ECS Transactions 19(31) (2009) 37–46.
[96] G.K.H. Wiberg, K.J.J. Mayrhofer, M. Arenz, Investigation of the Oxygen Reduction Activity on Silver - A Rotating Disc Electrode Study, Fuel Cells 10(4) (2010) 575–581.
[97] M. Innocenti, C. Zafferoni, A. Lavacchi, L. Becucci, F. Di Benedetto, E. Carretti, F. Vizza, M.L. Foresti, Electroactivation of Microparticles of Silver on Glassy Carbon for Oxygen Reduction and Oxidation Reactions, Journal of the Electrochemical Society 161(7) (2014) D3018-D3024.
[98] E. Kirowa-Eisner, Y. Bonfil, D. Tzur, E. Gileadi, Thermodynamics and kinetics of upd of lead on polycrystalline silver and gold, Journal of Electroanalytical Chemistry 552 (2003) 171–183.
[99] F.W. Campbell, R.G. Compton, Contrasting Underpotential Depositions of Lead and Cadmium on Silver Macroelectrodes and Silver Nanoparticle Electrode Arrays, International Journal of Electrochemical Science 5(3) (2010) 407–413.
[100] Y.Z. Lu, Y.C. Wang, W. Chen, Silver nanorods for oxygen reduction: Strong effects of protecting ligand on the electrocatalytic activity, Journal of Power Sources 196(6) (2011) 3033–3038.
[101] I. Katsounaros, K.J.J. Mayrhofer, The influence of non-covalent interactions on the hydrogen peroxide electrochemistry on platinum in alkaline electrolytes, Chemical Communications 48(53) (2012) 6660–6662.
[102] M. Hepel, M. Tomkiewicz, Study of the Initial Stages of Anodic Oxidation of Polycrystalline Silver in KOH Solutions, Journal of The Electrochemical Society 131(6) (1984) 1288–1294.
[103] M.A. Hernandez-Rodriguez, M.C. Goya, M.C. Arevalo, J.L. Rodriguez, E. Pastor, Carbon supported Ag and Ag-Co catalysts tolerant to methanol and ethanol for the oxygen reduction reaction in alkaline media, International Journal of Hydrogen Energy 41(43) (2016) 19789–19798.
[104] L.T. Soo, K.S. Loh, A. Mohamad, W.R.W. Daud, W.Y. Wong, Synthesis of silver/nitrogen-doped reduced graphene oxide through a one-step thermal solid-state reaction for oxygen reduction in an alkaline medium, Journal of Power Sources 324 (2016) 412–420.
[105] Y. Wang, Y. Qiao, Y. Chen, T. Hu, L. Zhang, One step pyrolysis synthesis of silver/nitrogen-doped carbon sheet for oxygen reduction in alkaline media, International Journal of Hydrogen Energy 42(36) (2017) 22903–22908.

[106] J. Hu, Z.W. Shi, X.Q. Wang, H.C. Qiao, H. Huang, Silver-modified porous 3D nitrogen-doped graphene aerogel: Highly efficient oxygen reduction electrocatalyst for Zn-Air battery, Electrochimica Acta 302 (2019) 216–224.
[107] W.M. Haynes, CRC Handbook of Chemistry and Physics, 93rd Edition, Taylor & Francis 2012.
[108] G. Panomsuwan, J. Chantaramethakul, C. Chokradjaroen, T. Ishizaki, In situ solution plasma synthesis of silver nanoparticles supported on nitrogen-doped carbons with enhanced oxygen reduction activity, Materials Letters 251 (2019) 135–139.
[109] W. Zhao, K. Huang, Q.H. Zhang, H. Wu, L. Gu, K.F. Yao, Y. Shen, Y. Shao, In-situ synthesis, operation and regeneration of nanoporous silver with high performance toward oxygen reduction reaction, Nano Energy 58 (2019) 69–77.
[110] S. Jin, M. Chen, H.F. Dong, B.Y. He, H.T. Lu, L. Su, W.H. Dai, Q.C. Zhang, X.J. Zhang, Stable silver nanoclusters electrochemically deposited on nitrogen-doped graphene as efficient electrocatalyst for oxygen reduction reaction, Journal of Power Sources 274 (2015) 1173–1179.
[111] S. Zoladek, M. Blicharska-Sobolewska, A.A. Krata, I.A. Rutkowska, A. Wadas, K. Miecznikowski, E. Negro, K. Vezzu, V. Di Noto, P.J. Kulesza, Heteropolytungstate-assisted fabrication and deposition of catalytic silver nanoparticles on different reduced graphene oxide supports: Electroreduction of oxygen in alkaline electrolyte, Journal of Electroanalytical Chemistry 875 (2020) 114694.
[112] C.L. Lee, Y.L. Tsai, C.H. Huang, K.L. Huang, Performance of silver nanocubes based on electrochemical surface area for catalyzing oxygen reduction reaction, Electrochemistry Communications 29 (2013) 37–40.
[113] S. Salome, R. Rego, M.C. Oliveira, Development of silver-gas diffusion electrodes for the oxygen reduction reaction by electrodeposition, Materials Chemistry and Physics 143(1) (2013) 109–115.
[114] X.L. Zhao, Z.Y. Deng, W. Zhao, B. Feng, M. Wang, M.R. Huang, L. Liu, G.S. Zou, Y. Shao, H.W. Zhu, Nanoporous silver using pulsed laser deposition for high-performance oxygen reduction reaction and hydrogen peroxide sensing, Nanoscale 12(37) (2020) 19413–19419.
[115] N.L. Pacioni, C.D. Borsarelli, V. Rey, A.V. Veglia, Synthetic Routes for the Preparation of Silver Nanoparticles, in: E.I. Alarcon, M. Griffith, K.I. Udekwu (Eds.), Silver Nanoparticle Applications: In the Fabrication and Design of Medical and Biosensing Devices, Springer International Publishing, Cham, 2015, pp. 13–46.
[116] Z.Q. Guo, H.Z. Zhang, X.C. Ma, X.M. Zhou, D. Liang, J.F. Mao, H.Y. Fang, J.M. Yu, Y. Sun, T.Z. Huang, Synergistic Catalytic Effect of Hollow Carbon Nanosphere and Silver Nanoparticles for Oxygen Reduction Reaction, Chemistryselect 5(27) (2020) 8099–8105.
[117] Z.W. Zhang, H.N. Li, J. Hu, B.Z. Liu, Q.R. Zhang, C. Fernandez, Q.M. Peng, High oxygen reduction reaction activity of C-N/Ag hybrid composites for Zn-air battery, Journal of Alloys and Compounds 694 (2017) 419–428.
[118] E. Härk, R. Jäger, E. Lust, Effect of Platinum Nanoparticle Loading on Oxygen Reduction at a Pt Nanocluster-Activated Microporous-Mesoporous Carbon Support, Electrocatalysis 6(3) (2015) 242–254.
[119] A.J. Bard, L.R. Faulkner, Electrochemical Methods: Fundamentals and Applications, 2nd ed., John Wiley & Sons, New York, 2001.

[120] R. Vinodh, D. Sangeetha, Carbon supported silver (Ag/C) electrocatalysts for alkaline membrane fuel cells, Journal of Materials Science 47(2) (2012) 852–859.
[121] B.D. Briggs, Y. Li, M.T. Swihart, M.R. Knecht, Reductant and Sequence Effects on the Morphology and Catalytic Activity of Peptide-Capped Au Nanoparticles, Acs Applied Materials & Interfaces 7(16) (2015) 8843–8851.
[122] G. Wu, A. Santandreu, W. Kellogg, S. Gupta, O. Ogoke, H.G. Zhang, H.L. Wang, L.M. Dai, Carbon nanocomposite catalysts for oxygen reduction and evolution reactions: From nitrogen doping to transition-metal addition, Nano Energy 29 (2016) 83–110.
[123] M.A. Kostowskyj, D.W. Kirk, S.J. Thorpe, Ag and Ag-Mn nanowire catalysts for alkaline fuel cells, International Journal of Hydrogen Energy 35(11) (2010) 5666–5672.
[124] T. Sharifi, G. Hu, X.E. Jia, T. Wagberg, Formation of Active Sites for Oxygen Reduction Reactions by Transformation of Nitrogen Functionalities in Nitrogen-Doped Carbon Nanotubes, Acs Nano 6(10) (2012) 8904–8912.
[125] S. Jalili, E.M. Goliaei, J. Schofield, Silver cluster supported on nitrogen-doped graphene as an electrocatalyst with high activity and stability for oxygen reduction reaction, International Journal of Hydrogen Energy 42(21) (2017) 14522–14533.
[126] L.F. Lai, J.R. Potts, D. Zhan, L. Wang, C.K. Poh, C.H. Tang, H. Gong, Z.X. Shen, L.Y. Jianyi, R.S. Ruoff, Exploration of the active center structure of nitrogen-doped graphene-based catalysts for oxygen reduction reaction, Energy & Environmental Science 5(7) (2012) 7936–7942.
[127] D. Ji, Y. Wang, S.G. Chen, Y.L. Zhang, L. Li, W. Ding, Z.D. Wei, Nitrogen-doped graphene wrapped around silver nanowires for enhanced catalysis in oxygen reduction reaction, Journal of Solid State Electrochemistry 22(7) (2018) 2287–2296.
[128] J. Lilloja, M. Mooste, E. Kibena-Põldsepp, A. Sarapuu, B. Zulevi, A. Kikas, H.-M. Piirsoo, A. Tamm, V. Kisand, S. Holdcroft, A. Serov, K. Tammeveski, Mesoporous iron-nitrogen co-doped carbon material as cathode catalyst for the anion exchange membrane fuel cell, Journal of Power Sources Advances 8 (2021) 100052.
[129] J.Y. Park, W.J. Dong, S.-M. Jung, Y.-T. Kim, J.-L. Lee, Oxygen reduction reaction of vertically-aligned nanoporous Ag nanowires, Applied Catalysis B: Environmental 298 (2021) 120586.
[130] Z. Wang, X. Cao, D.D. Peng, Y. Lu, B.W. Zhang, K. Huang, T.Y. Zhang, J.S. Wu, Y.Z. Huang, Strained Ultralong Silver Nanowires for Enhanced Electrocatalytic Oxygen Reduction Reaction in Alkaline Medium, Journal of Physical Chemistry Letters 12(8) (2021) 2029–2035.
[131] S. Choi, Y. Park, J. Choi, C. Lee, H.-S. Cho, C.-H. Kim, J. Koo, H.M. Lee, Structural Effectiveness of AgCl-decorated Ag Nanowires Enhancing Oxygen Reduction, ACS Sustainable Chemistry & Engineering 9(22) (2021) 7519–7528.
[132] S.H. Li, H. Miao, Q. Xu, Y.J. Xue, S.S. Sun, Q. Wang, Z.P. Liu, Silver nanoparticles supported on a nitrogen-doped graphene aerogel composite catalyst for an oxygen reduction reaction in aluminum air batteries, Rsc Advances 6(101) (2016) 99179–99183.
[133] S.J. Cai, J.T. Jin, X.C. Qiao, W.L. Wang, P. Jiang, J.W. Guo, H.B. Fan, Rapid precipitation-reduction synthesis of carbon-supported silver for efficient oxygen

reduction reaction in alkaline solution, Journal of Solid State Electrochemistry 23(8) (2019) 2601–2607.
[134] N. Wagner, M. Schulze, E. Gülzow, Long term investigations of silver cathodes for alkaline fuel cells, Journal of Power Sources 127(1) (2004) 264–272.
[135] T.J. Omasta, A.M. Park, J.M. Lamanna, Y. Zhang, X. Peng, L. Wang, D.L. Jacobson, J.R. Varcoe, D.S. Hussey, B.S. Pivovar, W.E. Mustain, Beyond catalysis and membranes: Visualizing and solving the challenge of electrode water accumulation and flooding in AEMFCs, Energy and Environmental Science 11(3) (2018) 551–558.
[136] V.M. Truong, N.B. Duong, H. Yang, Comparison of Carbon Supports in Anion Exchange Membrane Fuel Cells, Materials 13(23) (2020) 5370.
[137] J. Huang, Z. Yu, J. Tang, P. Wang, Q. Tan, J. Wang, X. Lei, A review on anion exchange membranes for fuel cells: Anion-exchange polyelectrolytes and synthesis strategies, International Journal of Hydrogen Energy 47(65) (2022) 27800–27820.
[138] T.B. Ferriday, P.H. Middleton, Alkaline fuel cell technology – A review, International Journal of Hydrogen Energy 46(35) (2021) 18489–18510.
[139] W.E. Mustain, Understanding how high-performance anion exchange membrane fuel cells were achieved: Component, interfacial, and cell-level factors, Current Opinion in Electrochemistry 12 (2018) 233–239.
[140] P. Teppor, R. Jäger, M. Paalo, A. Adamson, M. Härmas, O. Volobujeva, J. Aruväli, R. Palm, E. Lust, Peat as a carbon source for non-platinum group metal oxygen electrocatalysts and AEMFC cathodes, International Journal of Hydrogen Energy 47(38) (2022) 16908–16920.
[141] A. Sokka, M. Mooste, M. Käärik, V. Gudkova, J. Kozlova, A. Kikas, V. Kisand, A. Treshchalov, A. Tamm, P. Paiste, J. Aruväli, J. Leis, A. Krumme, S. Holdcroft, S. Cavaliere, F. Jaouen, K. Tammeveski, Iron and cobalt containing electrospun carbon nanofibre-based cathode catalysts for anion exchange membrane fuel cell, International Journal of Hydrogen Energy 46(61) (2021) 31275–31287.
[142] Y. Zhou, H. Yu, F. Xie, Y. Zhao, X. Sun, D. Yao, G. Jiang, J. Geng, Z. Shao, Improving cell performance for anion exchange membrane fuel cells with FeNC cathode by optimizing ionomer content, International Journal of Hydrogen Energy 48(13) (2023) 5266–5275.
[143] R. Gutru, Z. Turtayeva, F. Xu, G. Maranzana, B. Vigolo, A. Desforges, A comprehensive review on water management strategies and developments in anion exchange membrane fuel cells, International Journal of Hydrogen Energy 45(38) (2020) 19642–19663.
[144] R. Gutru, Z. Turtayeva, F. Xu, G. Maranzana, R. Thimmappa, M. Mamlouk, A. Desforges, B. Vigolo, Recent progress in heteroatom doped carbon based electrocatalysts for oxygen reduction reaction in anion exchange membrane fuel cells, International Journal of Hydrogen Energy 48(9) (2023) 3593-3631.
[145] L. Zeng, T.S. Zhao, L. An, A high-performance supportless silver nanowire catalyst for anion exchange membrane fuel cells, Journal of Materials Chemistry A 3(4) (2015) 1410–1416.
[146] P.A. Ganesh, A.N. Prakrthi, S.S. Chandrasekaran, D. Jeyakumar, Shape-tuned, surface-active and support-free silver oxygen reduction electrocatalyst enabled high performance fully non-PGM alkaline fuel cell, Rsc Advances 11(40) (2021) 24872–24882.

[147] L. Xin, Z.Y. Zhang, Z.C. Wang, J. Qi, W.Z. Li, Carbon supported Ag nanoparticles as high performance cathode catalyst for H-2/O-2 anion exchange membrane fuel cell, Frontiers in Chemistry 1 (2013) 16.
[148] J.R. Varcoe, R.C.T. Slade, G.L. Wright, Y.L. Chen, Steady-state dc and impedance investigations of H-2/O-2 alkaline membrane fuel cells with commercial Pt/C, Ag/C, and Au/C cathodes, Journal of Physical Chemistry B 110(42) (2006) 21041–21049.
[149] Y.P. Yang, X.C. Xu, P.P. Sun, H.X. Xu, L. Yang, X.F. Zeng, Y. Huang, S.T. Wang, D.P. Cao, AgNPs@Fe-N-C oxygen reduction catalysts for anion exchange membrane fuel cells, Nano Energy 100 (2022) 107466.
[150] S. Hussain, H. Erikson, N. Kongi, M. Merisalu, P. Ritslaid, V. Sammelselg, K. Tammeveski, Heat-treatment effects on the ORR activity of Pt nanoparticles deposited on multi-walled carbon nanotubes using magnetron sputtering technique, International Journal of Hydrogen Energy 42(9) (2017) 5958–5970.
[151] K. Jukk, N. Alexeyeva, P. Ritslaid, J. Kozlova, V. Sammelselg, K. Tammeveski, Electrochemical Reduction of Oxygen on Heat-Treated Pd Nanoparticle/Multi-Walled Carbon Nanotube Composites in Alkaline Solution, Electrocatalysis 4(1) (2013) 42–48.
[152] N. Alexeyeva, J. Kozlova, V. Sammelselg, P. Ritslaid, H. Mandar, K. Tammeveski, Electrochemical and surface characterisation of gold nanoparticle decorated multi-walled carbon nanotubes, Applied Surface Science 256(10) (2010) 3040–3046.
[153] S. Hussain, H. Erikson, N. Kongi, A. Tarre, P. Ritslaid, M. Kook, M. Rähn, M. Merisalu, V. Sammelselg, K. Tammeveski, Improved ORR Activity and Long-Term Durability of Pt Nanoparticles Deposited on TiO2-Decorated Multiwall Carbon Nanotubes, Journal of the Electrochemical Society 166(16) (2019) F1284-F1291.
[154] K. Jukk, N. Kongi, A. Tarre, A. Rosental, A.B. Treshchalov, J. Kozlova, P. Ritslaid, L. Matisen, V. Sammelselg, K. Tammeveski, Electrochemical oxygen reduction behaviour of platinum nanoparticles supported on multi-walled carbon nanotube/titanium dioxide composites, Journal of Electroanalytical Chemistry 735 (2014) 68–76.
[155] J.-G. Wang, Y. Yang, Z.-H. Huang, F. Kang, Rational synthesis of MnO2/conducting polypyrrole@carbon nanofiber triaxial nano-cables for high-performance supercapacitors, Journal of Materials Chemistry 22(33) (2012) 16943–16949.
[156] S.W. Lee, J. Kim, S. Chen, P.T. Hammond, Y. Shao-Horn, Carbon Nanotube/Manganese Oxide Ultrathin Film Electrodes for Electrochemical Capacitors, ACS Nano 4(7) (2010) 3889–3896.
[157] Q. Li, J. Liu, J. Zou, A. Chunder, Y. Chen, L. Zhai, Synthesis and electrochemical performance of multi-walled carbon nanotube/polyaniline/MnO2 ternary coaxial nanostructures for supercapacitors, Journal of Power Sources 196(1) (2011) 565–572.
[158] Z. Yang, X.M. Zhou, H.G. Nie, Z. Yao, S.M. Huang, Facile Construction of Manganese Oxide Doped Carbon Nanotube Catalysts with High Activity for Oxygen Reduction Reaction and Investigations into the Origin of their Activity Enhancement, Acs Applied Materials & Interfaces 3(7) (2011) 2601–2606.
[159] F.-P. Hu, X.-G. Zhang, F. Xiao, J.-L. Zhang, Oxygen reduction on Ag–MnO2/SWNT and Ag–MnO2/AB electrodes, Carbon 43(14) (2005) 2931–2936.

[160] S. Wolf, M. Roschger, B. Genorio, M. Kolar, D. Garstenauer, B. Bitschnau, V. Hacker, Ag-MnxOy on Graphene Oxide Derivatives as Oxygen Reduction Reaction Catalyst in Alkaline Direct Ethanol Fuel Cells, Catalysts 12(7) (2022) 780.
[161] C. Lai, P. Kolla, Y. Zhao, H. Fong, A.L. Smirnova, Lignin-derived electrospun carbon nanofiber mats with supercritically deposited Ag nanoparticles for oxygen reduction reaction in alkaline fuel cells, Electrochimica Acta 130 (2014) 431–438.
[162] K. Tammeveski, T. Tenno, J. Claret, C. Ferrater, Electrochemical reduction of oxygen on thin-film Pt electrodes in 0.1 M KOH, Electrochimica Acta 42(5) (1997) 893–897.
[163] A. Sarapuu, A. Kasikov, T. Laaksonen, K. Kontturi, K. Tammeveski, Electrochemical reduction of oxygen on thin-film Pt electrodes in acid solutions, Electrochimica Acta 53(20) (2008) 5873–5880.
[164] A. Sarapuu, M. Nurmik, H. Maendar, A. Rosental, T. Laaksonen, K. Kontturi, D.J. Schiffrin, K. Tammeveski, Electrochemical reduction of oxygen on nanostructured gold electrodes, Journal of Electroanalytical Chemistry 612(1) (2008) 78–86.
[165] H. Erikson, A. Kasikov, C. Johans, K. Kontturi, K. Tammeveski, A. Sarapuu, Oxygen reduction on Nafion-coated thin-film palladium electrodes, Journal of Electroanalytical Chemistry 652(1–2) (2011) 1–7.
[166] F.W. Campbell, S.R. Belding, R. Baron, L. Xiao, R.G. Compton, Hydrogen Peroxide Electroreduction at a Silver-Nanoparticle Array: Investigating Nanoparticle Size and Coverage Effects, Journal of Physical Chemistry C 113(21) (2009) 9053–9062.
[167] V. Bansal, V. Li, A.P. O'Mullane, S.K. Bhargava, Shape dependent electrocatalytic behaviour of silver nanoparticles, Crystengcomm 12(12) (2010) 4280–4286.
[168] J. Dong, T.T. Sun, S.Y. Li, N.N. Shan, J.F. Chen, Y.S. Yan, L.B. Xu, 3D ordered macro-/mesoporous carbon supported Ag nanoparticles for efficient electrocatalytic oxygen reduction reaction, Journal of Colloid and Interface Science 554 (2019) 177–182.
[169] A.K. Nair, V.T. Veettil, N. Kalarikkal, S. Thomas, M.S. Kala, V. Sahajwalla, R.K. Joshi, S. Alwarappan, Boron doped graphene wrapped silver nanowires as an efficient electrocatalyst for molecular oxygen reduction, Scientific Reports 6 (2016) 37731.
[170] A. Abedini, A.A.A. Bakar, F. Larki, P.S. Menon, M.S. Islam, S. Shaari, Recent Advances in Shape-Controlled Synthesis of Noble Metal Nanoparticles by Radiolysis Route, Nanoscale Research Letters 11 (2016) 1–13.
[171] P.K. Adanuvor, R.E. White, Oxygen reduction on silver in 6.5M caustic soda solution, Journal of the Electrochemical Society 135(10) (1988) 2509–2517.
[172] D.X. Zhu, S. Chen, J.L. Mi, C.X. Xu, P.F. Luo, J.G. Cheng, H.H. Zhong, Y.W. Lu, Coupling Enhanced Oxygen Reduction Reaction Activity from Ag Nanorods-rGO Hybrids, Journal of the Electrochemical Society 166(13) (2019) H587–H591.
[173] S. Hussain, N. Kongi, L. Matisen, J. Kozlova, V. Sammelselg, K. Tammeveski, Platinum nanoparticles supported on nitrobenzene-functionalised graphene nanosheets as electrocatalysts for oxygen reduction reaction in alkaline media, Electrochemistry Communications 81 (2017) 79–83.

[174] M. Lüsi, H. Erikson, K. Tammeveski, A. Treshchalov, A. Kikas, H.M. Piirsoo, V. Kisand, A. Tamm, J. Aruväli, J. Solla-Gullon, J.M. Feliu, Oxygen reduction reaction on Pd nanoparticles supported on novel mesoporous carbon materials, Electrochimica Acta 394 (2021) 139132.
[175] R.D. Giles, J.A. Harrison, Potentiodynamic sweep measurements of the anodic oxidation of silver in alkaline solutions, Journal of Electroanalytical Chemistry and Interfacial Electrochemistry 27(1) (1970) 161–163.
[176] J. Ambrose, R.G. Barradas, The electrochemical formation of Ag2O in KOH electrolyte, Electrochimica Acta 19(11) (1974) 781–786.
[177] M. Fleischmann, D.J. Lax, H.R. Thirsk, Kinetic studies of electrochemical formation of argentous oxide, Transactions of the Faraday Society 64(0) (1968) 3128–3136.
[178] B.G. Pound, D.D. Macdonald, J.W. Tomlinson, The electrochemistry of silver in KOH at elevated temperatures—II. Cyclic voltammetry and galvanostatic charging studies, Electrochimica Acta 25(5) (1980) 563–573.
[179] B.G. Pound, D.D. Macdonald, J.W. Tomlinson, The electrochemistry of silver in KOH solutions at elevated temperatures—I. thermodynamics, Electrochimica Acta 24(9) (1979) 929–937.
[180] J.A. McMillan, Higher Oxidation States of Silver, Chemical Reviews 62(1) (1962) 65–80.
[181] M. Schalenbach, O. Kasian, M. Ledendecker, F.D. Speck, A.M. Mingers, K.J.J. Mayrhofer, S. Cherevko, The Electrochemical Dissolution of Noble Metals in Alkaline Media, Electrocatalysis 9(2) (2018) 153–161.
[182] Z-Z. Shi, W-P Li, W-J Kang, Y. Feng, Z. Li, X-Y. Zhong, J. Yang, H. Liu, C-K. Dong, P-F. Yin, F-R. Chen, X-W Du, Silver Clusters with Adatoms as a Catalyst for the Oxygen Reduction Reaction, ACS Catalysis 13 (2023) 9181–9189.

9. SUMMARY IN ESTONIAN

Hapniku elektrokeemiline redutseerumine hõbedal põhinevatel katalüsaatoritel

Doktoritöös hinnati hõbedal põhinevate katalüsaatorite elektrokatalüütilist aktiivsust hapniku redutseerumisel aluselises keskkonnas. Sel eesmärgil valmistati ja uuriti nanostruktuurseid materjale, mis võiksid leida rakendust madalatemperatuurse kütuseelemendi katoodmaterjalina. Põhifookuses oli Ag nanoosakeste sünteesimeetodite ja katalüsaatorikandja mõju uurimine O_2 redutseerumise kineetilistele parameetritele, nagu näiteks massaktiivsus ja eriaktiivsus. Hõbedal põhinevad katalüsaatorid valmistati erinevatele süsinikkandjatele, kasutades elektrokeemilisi, keemilisi ja füüsikalisi sadestusmeetodeid. Valmistatud materjale uuriti peale elektrokeemiliste meetodite ka füüsikaliste meetoditega, nagu näiteks SEM, TEM, XRD ja XPS.

Doktoritöö kolmes esimeses osas rakendati Ag-osakeste valmistamiseks elektrosadestamise meetodit. Nendest kahes kasutati samu elektrokeemilisi protseduure, kus Ag-osakesed sadestati puhtale klaassüsinikalusele, kusjuures esimeses osas sadestati osakesed vesikeskkonnast [I] ja teises osas mittevesikeskkonnast (atsetonitriilist) [II]. Mõlemas nimetatud osas varieeriti sadestamisaegu. Esimeses osas saadi suur kogus väiksemaid, kuni 50 nm hõbedaosakesi ja mõningaid suuri aglomeraate. Teises osas olid osakesed üldiselt mõnevõrra suuremad, kuni 90 nm, kuid suuri aglomeraate ei täheldatud. Mõlemal puhul selgus, et katalüsaatorite eriaktiivsus ja massaktiivsus ei sõltu sadestamise ajast. Kolmandas osas elektrosadestati Ag-osakesed neljale suurepinnalisele süsinikkandjale ja selleks kasutati kahte erinevat sadestamise protseduuri. Sadestusprotseduurist sõltumata selgus, et suurim massaktiivsus oli Ag nanoosakestel, mis olid sadestatud lämmastikuga dopeeritud grafeenoksiidile. Suurem elektrokatalüütiline aktiivsus võis tuleneda Ag-osakeste ja süsinikkandjal olevate lämmastikurühmade koostoimest [III].

Neljandas, viiendas ja kuuendas osas valmistati Ag nanoosakesed erinevatele suurepinnalistele süsinikkandjatele, kasutades keemilisi sadestusmeetodeid. Neljandas osas valmistati Ag-katalüsaatorid kahele suure eripinnaga karbiidset päritolu süsinikule ja võrdluseks ka suurepinnalisele Vulcan XC-72R süsinikkandjale. Karbiidset päritolu süsinikule valmistatud katalüsaatorid näitasid kordades kõrgemat massaktiivsust kui Vulcan XC-72R süsinikkandjale valmistatud katalüsaatorid [IV]. Viiendas osas sadestati Ag nanoosakesed lämmastikuga dopeeritud grafeenoksiidile, kasutades kolme erinevat sünteesieeskirja. Sünteesil kasutatud redutseerija mõjutas tugevalt Ag nanoosakeste suurust ja jaotust, mis omakorda muutis O_2 redutseerumise aktiivsust. Katalüsaatorite elektrokatalüütilise aktiivsuse puhul mängis suurt rolli ka Ag nanoosakeste ja grafeenoksiidil olevate lämmastikurühmade vaheline interaktsioon [V]. Kuuendas osas valmistati Ag nanoosakesed kahele kommertsiaalsele mesopoorsele lämmastikku sisaldavale süsinikkandjale (Pajarito Powder, LLC), kasutades kahte erinevat sadestamisprotseduuri. Mõlemal sadestamisprotseduuril kasutatud redut-

seerija puhul jäi Ag nanoosakeste kristalliidi suurus sarnasesse vahemikku, olles 19 kuni 28 nm. Katalüsaatorite massaktiivsus sõltus suurel määral süsinikkandjast ning mesopoorsetel materjalidel olid need kordades suuremad kui võrdluseks kasutatud tavapärasel süsinikkandjal. Parimaid katalüsaatormaterjale testiti ka anioonvahetusmembraaniga kütuseelemendis, kus saavutati maksimaalne võimsustihedus 310 mW cm^{-2}, mis jäi ainult mõnevõrra alla võrdluseks kasutatud kommertsiaalsele Pt/C katalüsaatorile (347 mW cm^{-2}) [VI].

Seitsmendas ja kaheksandas osas valmistati Ag-katalüsaatorid füüsikalistel meetoditel. Seitsmendas osas kanti hõbe kahele eri viisil sünteesitud MnO_2_MWCNT kandjale, milleks kasutati magnetrontolmustamise meetodit. Selliste nanokomposiitide puhul on olulisteks muutujateks sünteesitud mangaanoksiidi vorm ning selle seondumine süsinikkandja ja hõbedaga [VII]. Kaheksandas osas valmistati õhukesed Ag kiled elektronkiirtega aurustamise meetodil, kus varieeriti Ag kilede nominaalseid paksusi. Tehti kindlaks, kuidas mõjutab saadud kilede paksus hapniku redutseerumise elektrokatalüütilisi omadusi. Selgus, et juba 1 nm paksune kiht näitab suurt elektrokatalüütilist aktiivsust [VIII].

Üheksandas osas uuriti kommertsiaalset päritolu hõbenanotraate diameetriga 35, 90 ja 120 nm. Vähima paksusega Ag nanotraadid näitasid hapniku redutseerumisel parimat elektrokatalüütilist aktiivsust [IX].

Kümnendas osas uuriti põhjalikult Ag elektrokeemilise lahustumise mõju Ag-põhiste katalüsaatorite stabiilsusele. Selgus, et mesopoorsed lämmastikuga dopeeritud süsinikmaterjalid olid Ag-katalüsaatorite valmistamiseks tavapärasest süsinikkandjast parem valik, kuna mesopoorselt süsinikkandjalt lahustunud hõbeda kogus oli väiksem [X].

Kokkuvõtteks võib öelda, et hapniku redutseerumine hõbedal põhinevatel katalüsaatoritel toimus peamiselt 4-elektronilist reaktsiooniteed pidi ehk saaduseks oli ainult vesi, vältides seega vahesaaduse vesinikperoksiidi teket. Tafeli tõusu väärtused näitasid, et hapniku redutseerumisreaktsiooni kiirust limiteerib esimese elektroni aeglane ülekanne hapniku molekulile. Seetõttu sobivad Ag-põhised nanostruktuursed katalüsaatormaterjalid madalatemperatuurse kütuseelemendi katoodmaterjaliks.

10. ACKNOWLEDGEMENT

I would like to express my deepest appreciation to supervisors Dr Heiki Erikson and Prof. Kaido Tammeveski for their time and effort in helping me complete my studies and publish the articles this PhD thesis includes.

In addition, I would like to acknowledge Dr. Aarne Kasikov, who prepared thin Ag films; Dr. Peeter Ritslaid, who magnetron-sputtered Ag onto MnO2_MWCNT substrates; Assoc. Prof. Aile Tamm and Prof. Väino Sammelselg and their co-workers, who performed SEM, TEM, EDS, XPS measurements; Jaan Aruväli, who performed XRD measurements, and many others, who helped me with physical characterisations and catalyst preparation. I would like to mention Dr Tiit Kaljuvee from the Tallinn University of Technology, who performed the TGA measurements, and Prof. A. M. Kannan from Arizona State University, USA, who contributed to the AEMFC studies. Special thanks go to Dr Valentín Briega-Martos and Dr Serhiy Cherevko for their valuable guidance during my Erlangen (HI-ERN) stay.

The work in this thesis was financially supported by the Estonian Research Council (grant PRG723), by the EU through the European Regional Development Fund (TK141, “Advanced materials and high-technology devices for energy recuperation systems”, Graduate School of Functional Materials and Technologies) and by institutional research funding (IUT20-16, IUT2-24, IUT2-54, IUT34-14) of the Estonian Ministry of Education and Research. The study exchange (in HI-ERN, Germany) was supported by Dora+ programme.

I would like to thank my family for their patience and support.

11. PUBLICATIONS

CURRICULUM VITAE

Name: Jonas Mart Linge
Date of birth: May 19, 1993
Citizenship: Estonian
Address: Ravila 14a, 50411 Tartu, Estonia
E-mail: jonasmartlinge@gmail.com

Education:

2019–…	University of Tartu, Faculty of Science and Technology, PhD studies, Chemistry
2017–2019	University of Tartu, Faculty of Science and Technology, MSc studies, Materials Science
2012–2017	University of Tartu, Faculty of Science and Technology, BSc studies, Chemistry
2009–2012	Nõo Reaalgümnaasium, secondary education

Professional experience:

2021–…	University of Tartu, Institute of Chemistry, chemist

Major scientific publications:

1. **J.M. Linge**, H. Erikson, A. Sarapuu, M. Merisalu, M. Rähn, L. Matisen, V. Sammelselg, K. Tammeveski, Electroreduction of oxygen on nitrogen-doped graphene oxide supported silver nanoparticles, Journal of Electroanalytical Chemistry 794 (2017) 197–203.
2. **J.M. Linge**, H. Erikson, M. Merisalu, L. Matisen, M. Käärik, J. Leis, V. Sammelselg, J. Aruväli, T. Kaljuvee, K. Tammeveski, Oxygen Reduction on Silver Nanoparticles Supported on Carbide-Derived Carbons, Journal of the Electrochemical Society 165 (2018) F1199–F1205.
3. **J.M. Linge**, H. Erikson, J. Kozlova, V. Sammelselg, K. Tammeveski, Oxygen reduction reaction on electrochemically deposited silver nanoparticles from non-aqueous solution, Journal of Electroanalytical Chemistry 810 (2018) 129–134.
4. **J.M. Linge**, H. Erikson, J. Kozlova, J. Aruväli, V. Sammelselg, K. Tammeveski, Oxygen reduction on electrodeposited silver catalysts in alkaline solution, Journal of Solid State Electrochemistry 22 (2018) 81–89.
5. **J.M. Linge**, H. Erikson, A. Kasikov, M. Rähn, V. Sammelselg, K. Tammeveski, Oxygen reduction reaction on thin-film Ag electrodes in alkaline solution, Electrochimica Acta 325 (2019) 134922.
6. **J.M. Linge**, D. Kozhemyakin, H. Erikson, S. Vlassov, N. Kongi, K. Tammeveski, Silver Nanowire-Based Catalysts for Oxygen Reduction Reaction in Alkaline Solution, Chemcatchem 13 (2021) 4364–4371.
7. **J.M. Linge**, H. Erikson, M. Merisalu, V. Sammelselg, K. Tammeveski, Oxygen reduction on silver catalysts electrodeposited on various nanocarbon supports, SN Applied Sciences 3 (2021) 263.

8. **J.M. Linge**, H. Erikson, M. Mooste, H.-M. Piirsoo, T. Kaljuvee, A. Kikas, J. Aruväli, V. Kisand, A. Tamm, A.M. Kannan, K. Tammeveski, Ag nanoparticles on mesoporous carbon support as cathode catalyst for anion exchange membrane fuel cell, International Journal of Hydrogen Energy 48 (2023) 11058–11070.
9. **J.M. Linge**, H. Erikson, P. Ritslaid, A. Kikas, V. Kisand, J. Aruväli, J. Kozlova, A. Tamm, A. Sarapuu, K. Tammeveski, Ag Sputter-Deposited on MnO_2-Carbon Nanotube Nanocomposites as Electrocatalysts for Oxygen Reduction Reaction in Alkaline Media, Catalysts 13 (2023) 976.

ELULOOKIRJELDUS

Nimi: Jonas Mart Linge
Sünniaeg: 19. mai 1993
Kodakondsus: Eesti
Aadress: Ravila 14a, 50411 Tartu, Eesti
E-mail: jonasmartlinge@gmail.com

Hariduskäik:

2019–…	Tartu Ülikool, Loodus- ja täppisteaduste valdkond, doktoriõpingud, keemia
2017–2019	Tartu Ülikool, Loodus- ja täppisteaduste valdkond, magistriõpingud, materjaliteadus
2012–2017	Tartu Ülikool, Loodus- ja täppisteaduste valdkond, bakalaureuseõpingud, keemia
2009–2012	Nõo Reaalgümnaasium, keskharidus

Töökogemus:

2021–…	Tartu Ülikool, Keemia instituut, keemik

Publikatsioonide loetelu:

1. **J.M. Linge**, H. Erikson, A. Sarapuu, M. Merisalu, M. Rähn, L. Matisen, V. Sammelselg, K. Tammeveski, Electroreduction of oxygen on nitrogen-doped graphene oxide supported silver nanoparticles, Journal of Electroanalytical Chemistry 794 (2017) 197–203.
2. **J.M. Linge**, H. Erikson, M. Merisalu, L. Matisen, M. Käärik, J. Leis, V. Sammelselg, J. Aruväli, T. Kaljuvee, K. Tammeveski, Oxygen Reduction on Silver Nanoparticles Supported on Carbide-Derived Carbons, Journal of the Electrochemical Society 165 (2018) F1199-F1205.
3. **J.M. Linge**, H. Erikson, J. Kozlova, V. Sammelselg, K. Tammeveski, Oxygen reduction reaction on electrochemically deposited silver nanoparticles from non-aqueous solution, Journal of Electroanalytical Chemistry 810 (2018) 129–134.
4. **J.M. Linge**, H. Erikson, J. Kozlova, J. Aruväli, V. Sammelselg, K. Tammeveski, Oxygen reduction on electrodeposited silver catalysts in alkaline solution, Journal of Solid State Electrochemistry 22 (2018) 81–89.
5. **J.M. Linge**, H. Erikson, A. Kasikov, M. Rähn, V. Sammelselg, K. Tammeveski, Oxygen reduction reaction on thin-film Ag electrodes in alkaline solution, Electrochimica Acta 325 (2019) 134922.
6. **J.M. Linge**, D. Kozhemyakin, H. Erikson, S. Vlassov, N. Kongi, K. Tammeveski, Silver Nanowire-Based Catalysts for Oxygen Reduction Reaction in Alkaline Solution, Chemcatchem 13 (2021) 4364–4371.
7. **J.M. Linge**, H. Erikson, M. Merisalu, V. Sammelselg, K. Tammeveski, Oxygen reduction on silver catalysts electrodeposited on various nanocarbon supports, SN Applied Sciences 3 (2021) 263.

8. **J.M. Linge**, H. Erikson, M. Mooste, H.-M. Piirsoo, T. Kaljuvee, A. Kikas, J. Aruväli, V. Kisand, A. Tamm, A.M. Kannan, K. Tammeveski, Ag nanoparticles on mesoporous carbon support as cathode catalyst for anion exchange membrane fuel cell, International Journal of Hydrogen Energy 48 (2023) 11058–11070.
9. **J.M. Linge**, H. Erikson, P. Ritslaid, A. Kikas, V. Kisand, J. Aruväli, J. Kozlova, A. Tamm, A. Sarapuu, K. Tammeveski, Ag Sputter-Deposited on MnO_2-Carbon Nanotube Nanocomposites as Electrocatalysts for Oxygen Reduction Reaction in Alkaline Media, Catalysts 13 (2023) 976.

DISSERTATIONES CHIMICAE UNIVERSITATIS TARTUENSIS

1. **Toomas Tamm.** Quantum-chemical simulation of solvent effects. Tartu, 1993, 110 p.
2. **Peeter Burk.** Theoretical study of gas-phase acid-base equilibria. Tartu, 1994, 96 p.
3. **Victor Lobanov.** Quantitative structure-property relationships in large descriptor spaces. Tartu, 1995, 135 p.
4. **Vahur Mäemets.** The ^{17}O and ^{1}H nuclear magnetic resonance study of H_2O in individual solvents and its charged clusters in aqueous solutions of electrolytes. Tartu, 1997, 140 p.
5. **Andrus Metsala.** Microcanonical rate constant in nonequilibrium distribution of vibrational energy and in restricted intramolecular vibrational energy redistribution on the basis of slater's theory of unimolecular reactions. Tartu, 1997, 150 p.
6. **Uko Maran.** Quantum-mechanical study of potential energy surfaces in different environments. Tartu, 1997, 137 p.
7. **Alar Jänes.** Adsorption of organic compounds on antimony, bismuth and cadmium electrodes. Tartu, 1998, 219 p.
8. **Kaido Tammeveski.** Oxygen electroreduction on thin platinum films and the electrochemical detection of superoxide anion. Tartu, 1998, 139 p.
9. **Ivo Leito.** Studies of Brønsted acid-base equilibria in water and non-aqueous media. Tartu, 1998, 101 p.
10. **Jaan Leis.** Conformational dynamics and equilibria in amides. Tartu, 1998, 131 p.
11. **Toonika Rinken.** The modelling of amperometric biosensors based on oxidoreductases. Tartu, 2000, 108 p.
12. **Dmitri Panov.** Partially solvated Grignard reagents. Tartu, 2000, 64 p.
13. **Kaja Orupõld.** Treatment and analysis of phenolic wastewater with microorganisms. Tartu, 2000, 123 p.
14. **Jüri Ivask.** Ion Chromatographic determination of major anions and cations in polar ice core. Tartu, 2000, 85 p.
15. **Lauri Vares.** Stereoselective Synthesis of Tetrahydrofuran and Tetrahydropyran Derivatives by Use of Asymmetric Horner-Wadsworth-Emmons and Ring Closure Reactions. Tartu, 2000, 184 p.
16. **Martin Lepiku.** Kinetic aspects of dopamine D_2 receptor interactions with specific ligands. Tartu, 2000, 81 p.
17. **Katrin Sak.** Some aspects of ligand specificity of P2Y receptors. Tartu, 2000, 106 p.
18. **Vello Pällin.** The role of solvation in the formation of iotsitch complexes. Tartu, 2001, 95 p.
19. **Katrin Kollist.** Interactions between polycyclic aromatic compounds and humic substances. Tartu, 2001, 93 p.

20. **Ivar Koppel.** Quantum chemical study of acidity of strong and superstrong Brønsted acids. Tartu, 2001, 104 p.
21. **Viljar Pihl.** The study of the substituent and solvent effects on the acidity of OH and CH acids. Tartu, 2001, 132 p.
22. **Natalia Palm.** Specification of the minimum, sufficient and significant set of descriptors for general description of solvent effects. Tartu, 2001, 134 p.
23. **Sulev Sild.** QSPR/QSAR approaches for complex molecular systems. Tartu, 2001, 134 p.
24. **Ruslan Petrukhin.** Industrial applications of the quantitative structure-property relationships. Tartu, 2001, 162 p.
25. **Boris V. Rogovoy.** Synthesis of (benzotriazolyl)carboximidamides and their application in relations with *N*- and *S*-nucleophyles. Tartu, 2002, 84 p.
26. **Koit Herodes.** Solvent effects on UV-vis absorption spectra of some solvatochromic substances in binary solvent mixtures: the preferential solvation model. Tartu, 2002, 102 p.
27. **Anti Perkson.** Synthesis and characterisation of nanostructured carbon. Tartu, 2002, 152 p.
28. **Ivari Kaljurand.** Self-consistent acidity scales of neutral and cationic Brønsted acids in acetonitrile and tetrahydrofuran. Tartu, 2003, 108 p.
29. **Karmen Lust.** Adsorption of anions on bismuth single crystal electrodes. Tartu, 2003, 128 p.
30. **Mare Piirsalu.** Substituent, temperature and solvent effects on the alkaline hydrolysis of substituted phenyl and alkyl esters of benzoic acid. Tartu, 2003, 156 p.
31. **Meeri Sassian.** Reactions of partially solvated Grignard reagents. Tartu, 2003, 78 p.
32. **Tarmo Tamm.** Quantum chemical modelling of polypyrrole. Tartu, 2003. 100 p.
33. **Erik Teinemaa.** The environmental fate of the particulate matter and organic pollutants from an oil shale power plant. Tartu, 2003. 102 p.
34. **Jaana Tammiku-Taul.** Quantum chemical study of the properties of Grignard reagents. Tartu, 2003. 120 p.
35. **Andre Lomaka.** Biomedical applications of predictive computational chemistry. Tartu, 2003. 132 p.
36. **Kostyantyn Kirichenko.** Benzotriazole – Mediated Carbon–Carbon Bond Formation. Tartu, 2003. 132 p.
37. **Gunnar Nurk.** Adsorption kinetics of some organic compounds on bismuth single crystal electrodes. Tartu, 2003, 170 p.
38. **Mati Arulepp.** Electrochemical characteristics of porous carbon materials and electrical double layer capacitors. Tartu, 2003, 196 p.
39. **Dan Cornel Fara.** QSPR modeling of complexation and distribution of organic compounds. Tartu, 2004, 126 p.
40. **Riina Mahlapuu.** Signalling of galanin and amyloid precursor protein through adenylate cyclase. Tartu, 2004, 124 p.

41. **Mihkel Kerikmäe.** Some luminescent materials for dosimetric applications and physical research. Tartu, 2004, 143 p.
42. **Jaanus Kruusma.** Determination of some important trace metal ions in human blood. Tartu, 2004, 115 p.
43. **Urmas Johanson.** Investigations of the electrochemical properties of polypyrrole modified electrodes. Tartu, 2004, 91 p.
44. **Kaido Sillar.** Computational study of the acid sites in zeolite ZSM-5. Tartu, 2004, 80 p.
45. **Aldo Oras.** Kinetic aspects of dATPαS interaction with $P2Y_1$ receptor. Tartu, 2004, 75 p.
46. **Erik Mölder.** Measurement of the oxygen mass transfer through the air-water interface. Tartu, 2005, 73 p.
47. **Thomas Thomberg.** The kinetics of electroreduction of peroxodisulfate anion on cadmium (0001) single crystal electrode. Tartu, 2005, 95 p.
48. **Olavi Loog.** Aspects of condensations of carbonyl compounds and their imine analogues. Tartu, 2005, 83 p.
49. **Siim Salmar.** Effect of ultrasound on ester hydrolysis in aqueous ethanol. Tartu, 2006, 73 p.
50. **Ain Uustare.** Modulation of signal transduction of heptahelical receptors by other receptors and G proteins. Tartu, 2006, 121 p.
51. **Sergei Yurchenko.** Determination of some carcinogenic contaminants in food. Tartu, 2006, 143 p.
52. **Kaido Tämm.** QSPR modeling of some properties of organic compounds. Tartu, 2006, 67 p.
53. **Olga Tšubrik.** New methods in the synthesis of multisubstituted hydrazines. Tartu. 2006, 183 p.
54. **Lilli Sooväli.** Spectrophotometric measurements and their uncertainty in chemical analysis and dissociation constant measurements. Tartu, 2006, 125 p.
55. **Eve Koort.** Uncertainty estimation of potentiometrically measured ph and pK_a values. Tartu, 2006, 139 p.
56. **Sergei Kopanchuk.** Regulation of ligand binding to melanocortin receptor subtypes. Tartu, 2006, 119 p.
57. **Silvar Kallip.** Surface structure of some bismuth and antimony single crystal electrodes. Tartu, 2006, 107 p.
58. **Kristjan Saal.** Surface silanization and its application in biomolecule coupling. Tartu, 2006, 77 p.
59. **Tanel Tätte.** High viscosity $Sn(OBu)_4$ oligomeric concentrates and their applications in technology. Tartu, 2006, 91 p.
60. **Dimitar Atanasov Dobchev**. Robust QSAR methods for the prediction of properties from molecular structure. Tartu, 2006, 118 p.
61. **Hannes Hagu**. Impact of ultrasound on hydrophobic interactions in solutions. Tartu, 2007, 81 p.
62. **Rutha Jäger.** Electroreduction of peroxodisulfate anion on bismuth electrodes. Tartu, 2007, 142 p.

63. **Kaido Viht.** Immobilizable bisubstrate-analogue inhibitors of basophilic protein kinases: development and application in biosensors. Tartu, 2007, 88 p.
64. **Eva-Ingrid Rõõm.** Acid-base equilibria in nonpolar media. Tartu, 2007, 156 p.
65. **Sven Tamp.** DFT study of the cesium cation containing complexes relevant to the cesium cation binding by the humic acids. Tartu, 2007, 102 p.
66. **Jaak Nerut.** Electroreduction of hexacyanoferrate(III) anion on Cadmium (0001) single crystal electrode. Tartu, 2007, 180 p.
67. **Lauri Jalukse.** Measurement uncertainty estimation in amperometric dissolved oxygen concentration measurement. Tartu, 2007, 112 p.
68. **Aime Lust.** Charge state of dopants and ordered clusters formation in CaF_2:Mn and CaF_2:Eu luminophors. Tartu, 2007, 100 p.
69. **Iiris Kahn**. Quantitative Structure-Activity Relationships of environmentally relevant properties. Tartu, 2007, 98 p.
70. **Mari Reinik.** Nitrates, nitrites, N-nitrosamines and polycyclic aromatic hydrocarbons in food: analytical methods, occurrence and dietary intake. Tartu, 2007, 172 p.
71. **Heili Kasuk.** Thermodynamic parameters and adsorption kinetics of organic compounds forming the compact adsorption layer at Bi single crystal electrodes. Tartu, 2007, 212 p.
72. **Erki Enkvist.** Synthesis of adenosine-peptide conjugates for biological applications. Tartu, 2007, 114 p.
73. **Svetoslav Hristov Slavov**. Biomedical applications of the QSAR approach. Tartu, 2007, 146 p.
74. **Eneli Härk.** Electroreduction of complex cations on electrochemically polished Bi(*hkl*) single crystal electrodes. Tartu, 2008, 158 p.
75. **Priit Möller.** Electrochemical characteristics of some cathodes for medium temperature solid oxide fuel cells, synthesized by solid state reaction technique. Tartu, 2008, 90 p.
76. **Signe Viggor.** Impact of biochemical parameters of genetically different pseudomonads at the degradation of phenolic compounds. Tartu, 2008, 122 p.
77. **Ave Sarapuu.** Electrochemical reduction of oxygen on quinone-modified carbon electrodes and on thin films of platinum and gold. Tartu, 2008, 134 p.
78. **Agnes Kütt.** Studies of acid-base equilibria in non-aqueous media. Tartu, 2008, 198 p.
79. **Rouvim Kadis.** Evaluation of measurement uncertainty in analytical chemistry: related concepts and some points of misinterpretation. Tartu, 2008, 118 p.
80. **Valter Reedo.** Elaboration of IVB group metal oxide structures and their possible applications. Tartu, 2008, 98 p.
81. **Aleksei Kuznetsov.** Allosteric effects in reactions catalyzed by the cAMP-dependent protein kinase catalytic subunit. Tartu, 2009, 133 p.

82. **Aleksei Bredihhin.** Use of mono- and polyanions in the synthesis of multisubstituted hydrazine derivatives. Tartu, 2009, 105 p.
83. **Anu Ploom.** Quantitative structure-reactivity analysis in organosilicon chemistry. Tartu, 2009, 99 p.
84. **Argo Vonk.** Determination of adenosine A_{2A}- and dopamine D_1 receptor-specific modulation of adenylate cyclase activity in rat striatum. Tartu, 2009, 129 p.
85. **Indrek Kivi.** Synthesis and electrochemical characterization of porous cathode materials for intermediate temperature solid oxide fuel cells. Tartu, 2009, 177 p.
86. **Jaanus Eskusson.** Synthesis and characterisation of diamond-like carbon thin films prepared by pulsed laser deposition method. Tartu, 2009, 117 p.
87. **Marko Lätt.** Carbide derived microporous carbon and electrical double layer capacitors. Tartu, 2009, 107 p.
88. **Vladimir Stepanov.** Slow conformational changes in dopamine transporter interaction with its ligands. Tartu, 2009, 103 p.
89. **Aleksander Trummal.** Computational Study of Structural and Solvent Effects on Acidities of Some Brønsted Acids. Tartu, 2009, 103 p.
90. **Eerold Vellemäe.** Applications of mischmetal in organic synthesis. Tartu, 2009, 93 p.
91. **Sven Parkel.** Ligand binding to 5-HT_{1A} receptors and its regulation by Mg^{2+} and Mn^{2+}. Tartu, 2010, 99 p.
92. **Signe Vahur.** Expanding the possibilities of ATR-FT-IR spectroscopy in determination of inorganic pigments. Tartu, 2010, 184 p.
93. **Tavo Romann**. Preparation and surface modification of bismuth thin film, porous, and microelectrodes. Tartu, 2010, 155 p.
94. **Nadežda Aleksejeva.** Electrocatalytic reduction of oxygen on carbon nanotube-based nanocomposite materials. Tartu, 2010, 147 p.
95. **Marko Kullapere.** Electrochemical properties of glassy carbon, nickel and gold electrodes modified with aryl groups. Tartu, 2010, 233 p.
96. **Liis Siinor.** Adsorption kinetics of ions at Bi single crystal planes from aqueous electrolyte solutions and room-temperature ionic liquids. Tartu, 2010, 101 p.
97. **Angela Vaasa.** Development of fluorescence-based kinetic and binding assays for characterization of protein kinases and their inhibitors. Tartu 2010, 101 p.
98. **Indrek Tulp.** Multivariate analysis of chemical and biological properties. Tartu 2010, 105 p.
99. **Aare Selberg.** Evaluation of environmental quality in Northern Estonia by the analysis of leachate. Tartu 2010, 117 p.
100. **Darja Lavõgina.** Development of protein kinase inhibitors based on adenosine analogue-oligoarginine conjugates. Tartu 2010, 248 p.
101. **Laura Herm.** Biochemistry of dopamine D_2 receptors and its association with motivated behaviour. Tartu 2010, 156 p.

102. **Terje Raudsepp.** Influence of dopant anions on the electrochemical properties of polypyrrole films. Tartu 2010, 112 p.
103. **Margus Marandi.** Electroformation of Polypyrrole Films: *In-situ* AFM and STM Study. Tartu 2011, 116 p.
104. **Kairi Kivirand.** Diamine oxidase-based biosensors: construction and working principles. Tartu, 2011, 140 p.
105. **Anneli Kruve.** Matrix effects in liquid-chromatography electrospray mass-spectrometry. Tartu, 2011, 156 p.
106. **Gary Urb.** Assessment of environmental impact of oil shale fly ash from PF and CFB combustion. Tartu, 2011, 108 p.
107. **Nikita Oskolkov.** A novel strategy for peptide-mediated cellular delivery and induction of endosomal escape. Tartu, 2011, 106 p.
108. **Dana Martin.** The QSPR/QSAR approach for the prediction of properties of fullerene derivatives. Tartu, 2011, 98 p.
109. **Säde Viirlaid.** Novel glutathione analogues and their antioxidant activity. Tartu, 2011, 106 p.
110. **Ülis Sõukand.** Simultaneous adsorption of Cd^{2+}, Ni^{2+}, and Pb^{2+} on peat. Tartu, 2011, 124 p.
111. **Lauri Lipping.** The acidity of strong and superstrong Brønsted acids, an outreach for the "limits of growth": a quantum chemical study. Tartu, 2011, 124 p.
112. **Heisi Kurig.** Electrical double-layer capacitors based on ionic liquids as electrolytes. Tartu, 2011, 146 p.
113. **Marje Kasari.** Bisubstrate luminescent probes, optical sensors and affinity adsorbents for measurement of active protein kinases in biological samples. Tartu, 2012, 126 p.
114. **Kalev Takkis.** Virtual screening of chemical databases for bioactive molecules. Tartu, 2012, 122 p.
115. **Ksenija Kisseljova**. Synthesis of aza-β^3-amino acid containing peptides and kinetic study of their phosphorylation by protein kinase A. Tartu, 2012, 104 p.
116. **Riin Rebane.** Advanced method development strategy for derivatization LC/ESI/MS. Tartu, 2012, 184 p.
117. **Vladislav Ivaništšev.** Double layer structure and adsorption kinetics of ions at metal electrodes in room temperature ionic liquids. Tartu, 2012, 128 p.
118. **Irja Helm.** High accuracy gravimetric Winkler method for determination of dissolved oxygen. Tartu, 2012, 139 p.
119. **Karin Kipper.** Fluoroalcohols as Components of LC-ESI-MS Eluents: Usage and Applications. Tartu, 2012, 164 p.
120. **Arno Ratas.** Energy storage and transfer in dosimetric luminescent materials. Tartu, 2012, 163 p.
121. **Reet Reinart-Okugbeni**. Assay systems for characterisation of subtype-selective binding and functional activity of ligands on dopamine receptors. Tartu, 2012, 159 p.

122. **Lauri Sikk.** Computational study of the Sonogashira cross-coupling reaction. Tartu, 2012, 81 p.
123. **Karita Raudkivi.** Neurochemical studies on inter-individual differences in affect-related behaviour of the laboratory rat. Tartu, 2012, 161 p.
124. **Indrek Saar.** Design of GalR2 subtype specific ligands: their role in depression-like behavior and feeding regulation. Tartu, 2013, 126 p.
125. **Ann Laheäär.** Electrochemical characterization of alkali metal salt based non-aqueous electrolytes for supercapacitors. Tartu, 2013, 127 p.
126. **Kerli Tõnurist.** Influence of electrospun separator materials properties on electrochemical performance of electrical double-layer capacitors. Tartu, 2013, 147 p.
127. **Kaija Põhako-Esko.** Novel organic and inorganic ionogels: preparation and characterization. Tartu, 2013, 124 p.
128. **Ivar Kruusenberg.** Electroreduction of oxygen on carbon nanomaterial-based catalysts. Tartu, 2013, 191 p.
129. **Sander Piiskop.** Kinetic effects of ultrasound in aqueous acetonitrile solutions. Tartu, 2013, 95 p.
130. **Ilona Faustova**. Regulatory role of L-type pyruvate kinase N-terminal domain. Tartu, 2013, 109 p.
131. **Kadi Tamm.** Synthesis and characterization of the micro-mesoporous anode materials and testing of the medium temperature solid oxide fuel cell single cells. Tartu, 2013, 138 p.
132. **Iva Bozhidarova Stoyanova-Slavova.** Validation of QSAR/QSPR for regulatory purposes. Tartu, 2013, 109 p.
133. **Vitali Grozovski**. Adsorption of organic molecules at single crystal electrodes studied by *in situ* STM method. Tartu, 2014, 146 p.
134. **Santa Veikšina**. Development of assay systems for characterisation of ligand binding properties to melanocortin 4 receptors. Tartu, 2014, 151 p.
135. **Jüri Liiv.** PVDF (polyvinylidene difluoride) as material for active element of twisting-ball displays. Tartu, 2014, 111 p.
136. **Kersti Vaarmets.** Electrochemical and physical characterization of pristine and activated molybdenum carbide-derived carbon electrodes for the oxygen electroreduction reaction. Tartu, 2014, 131 p.
137. **Lauri Tõntson**. Regulation of G-protein subtypes by receptors, guanine nucleotides and Mn^{2+}. Tartu, 2014, 105 p.
138. **Aiko Adamson.** Properties of amine-boranes and phosphorus analogues in the gas phase. Tartu, 2014, 78 p.
139. **Elo Kibena**. Electrochemical grafting of glassy carbon, gold, highly oriented pyrolytic graphite and chemical vapour deposition-grown graphene electrodes by diazonium reduction method. Tartu, 2014, 184 p.
140. **Teemu Näykki.** Novel Tools for Water Quality Monitoring – From Field to Laboratory. Tartu, 2014, 202 p.
141. **Karl Kaupmees.** Acidity and basicity in non-aqueous media: importance of solvent properties and purity. Tartu, 2014, 128 p.

142. **Oleg Lebedev**. Hydrazine polyanions: different strategies in the synthesis of heterocycles. Tartu, 2015, 118 p.
143. **Geven Piir.** Environmental risk assessment of chemicals using QSAR methods. Tartu, 2015, 123 p.
144. **Olga Mazina.** Development and application of the biosensor assay for measurements of cyclic adenosine monophosphate in studies of G protein-coupled receptor signalinga. Tartu, 2015, 116 p.
145. **Sandip Ashokrao Kadam.** Anion receptors: synthesis and accurate binding measurements. Tartu, 2015, 116 p.
146. **Indrek Tallo.** Synthesis and characterization of new micro-mesoporous carbide derived carbon materials for high energy and power density electrical double layer capacitors. Tartu, 2015, 148 p.
147. **Heiki Erikson.** Electrochemical reduction of oxygen on nanostructured palladium and gold catalysts. Tartu, 2015, 204 p.
148. **Erik Anderson.** *In situ* Scanning Tunnelling Microscopy studies of the interfacial structure between Bi(111) electrode and a room temperature ionic liquid. Tartu, 2015, 118 p.
149. **Girinath G. Pillai.** Computational Modelling of Diverse Chemical, Biochemical and Biomedical Properties. Tartu, 2015, 140 p.
150. **Piret Pikma.** Interfacial structure and adsorption of organic compounds at Cd(0001) and Sb(111) electrodes from ionic liquid and aqueous electrolytes: an *in situ* STM study. Tartu, 2015, 126 p.
151. **Ganesh babu Manoharan.** Combining chemical and genetic approaches for photoluminescence assays of protein kinases. Tartu, 2016, 126 p.
152. **Carolin Siimenson**. Electrochemical characterization of halide ion adsorption from liquid mixtures at Bi(111) and pyrolytic graphite electrode surface. Tartu, 2016, 110 p.
153. **Asko Laaniste.** Comparison and optimisation of novel mass spectrometry ionisation sources. Tartu, 2016, 156 p.
154. **Hanno Evard.** Estimating limit of detection for mass spectrometric analysis methods. Tartu, 2016, 224 p.
155. **Kadri Ligi.** Characterization and application of protein kinase-responsive organic probes with triplet-singlet energy transfer. Tartu, 2016, 122 p.
156. **Margarita Kagan.** Biosensing penicillins' residues in milk flows. Tartu, 2016, 130 p.
157. **Marie Kriisa.** Development of protein kinase-responsive photoluminescent probes and cellular regulators of protein phosphorylation. Tartu, 2016, 106 p.
158. **Mihkel Vestli.** Ultrasonic spray pyrolysis deposited electrolyte layers for intermediate temperature solid oxide fuel cells. Tartu, 2016, 156 p.
159. **Silver Sepp**. Influence of porosity of the carbide-derived carbon on the properties of the composite electrocatalysts and characteristics of polymer electrolyte fuel cells. Tartu, 2016, 137 p.
160. **Kristjan Haav**. Quantitative relative equilibrium constant measurements in supramolecular chemistry. Tartu, 2017, 158 p.

161. **Anu Teearu**. Development of MALDI-FT-ICR-MS methodology for the analysis of resinous materials. Tartu, 2017, 205 p.
162. **Taavi Ivan**. Bifunctional inhibitors and photoluminescent probes for studies on protein complexes. Tartu, 2017, 140 p.
163. **Maarja-Liisa Oldekop**. Characterization of amino acid derivatization reagents for LC-MS analysis. Tartu, 2017, 147 p.
164. **Kristel Jukk**. Electrochemical reduction of oxygen on platinum- and palladium-based nanocatalysts. Tartu, 2017, 250 p.
165. **Siim Kukk**. Kinetic aspects of interaction between dopamine transporter and *N*-substituted nortropane derivatives. Tartu, 2017, 107 p.
166. **Birgit Viira**. Design and modelling in early drug development in targeting HIV-1 reverse transcriptase and Malaria. Tartu, 2017, 172 p.
167. **Rait Kivi**. Allostery in cAMP dependent protein kinase catalytic subunit. Tartu, 2017, 115 p.
168. **Agnes Heering**. Experimental realization and applications of the unified acidity scale. Tartu, 2017, 123 p.
169. **Delia Juronen**. Biosensing system for the rapid multiplex detection of mastitis-causing pathogens in milk. Tartu, 2018, 85 p.
170. **Hedi Rahnel.** ARC-inhibitors: from reliable biochemical assays to regulators of physiology of cells. Tartu, 2018, 176 p.
171. **Anton Ruzanov.** Computational investigation of the electrical double layer at metal–aqueous solution and metal–ionic liquid interfaces. Tartu, 2018, 129 p.
172. **Katrin Kestav.** Crystal Structure-Guided Development of Bisubstrate-Analogue Inhibitors of Mitotic Protein Kinase Haspin. Tartu, 2018, 166 p.
173. **Mihkel Ilisson.** Synthesis of novel heterocyclic hydrazine derivatives and their conjugates. Tartu, 2018, 101 p.
174. **Anni Allikalt.** Development of assay systems for studying ligand binding to dopamine receptors. Tartu, 2018, 160 p.
175. **Ove Oll.** Electrical double layer structure and energy storage characteristics of ionic liquid based capacitors. Tartu, 2018, 187 p.
176. **Rasmus Palm.** Carbon materials for energy storage applications. Tartu, 2018, 114 p.
177. **Jörgen Metsik.** Preparation and stability of poly(3,4-ethylenedioxythiophene) thin films for transparent electrode applications. Tartu, 2018, 111 p.
178. **Sofja Tšepelevitš.** Experimental studies and modeling of solute-solvent interactions. Tartu, 2018, 109 p.
179. **Märt Lõkov.** Basicity of some nitrogen, phosphorus and carbon bases in acetonitrile. Tartu, 2018, 104 p.
180. **Anton Mastitski**. Preparation of α-aza-amino acid precursors and related compounds by novel methods of reductive one-pot alkylation and direct alkylation. Tartu, 2018, 155 p.
181. **Jürgen Vahter**. Development of bisubstrate inhibitors for protein kinase CK2. Tartu, 2019, 186 p.

182. **Piia Liigand.** Expanding and improving methodology and applications of ionization efficiency measurements. Tartu, 2019, 189 p.
183. **Sigrid Selberg.** Synthesis and properties of lipophilic phosphazene-based indicator molecules. Tartu, 2019, 74 p.
184. **Jaanus Liigand.** Standard substance free quantification for LC/ESI/MS analysis based on the predicted ionization efficiencies. Tartu, 2019, 254 p.
185. **Marek Mooste.** Surface and electrochemical characterisation of aryl film and nanocomposite material modified carbon and metal-based electrodes. Tartu, 2019, 304 p.
186. **Mare Oja.** Experimental investigation and modelling of pH profiles for effective membrane permeability of drug substances. Tartu, 2019, 306 p.
187. **Sajid Hussain.** Electrochemical reduction of oxygen on supported Pt catalysts. Tartu, 2019, 220 p.
188. **Ronald Väli.** Glucose-derived hard carbon electrode materials for sodium-ion batteries. Tartu, 2019, 180 p.
189. **Ester Tee.** Analysis and development of selective synthesis methods of hierarchical micro- and mesoporous carbons. Tartu, 2019, 210 p.
190. **Martin Maide.** Influence of the microstructure and chemical composition of the fuel electrode on the electrochemical performance of reversible solid oxide fuel cell. Tartu, 2020, 144 p.
191. **Edith Viirlaid.** Biosensing Pesticides in Water Samples. Tartu, 2020, 102 p.
192. **Maike Käärik.** Nanoporous carbon: the controlled nanostructure, and structure-property relationships. Tartu, 2020, 162 p.
193. **Artur Gornischeff.** Study of ionization efficiencies for derivatized compounds in LC/ESI/MS and their application for targeted analysis. Tartu, 2020, 124 p.
194. **Reet Link.** Ligand binding, allosteric modulation and constitutive activity of melanocortin-4 receptors. Tartu, 2020, 108 p.
195. **Pilleriin Peets.** Development of instrumental methods for the analysis of textile fibres and dyes. Tartu, 2020, 150 p.
196. **Larisa Ivanova.** Design of active compounds against neurodegenerative diseases. Tartu, 2020, 152 p.
197. **Meelis Härmas.** Impact of activated carbon microstructure and porosity on electrochemical performance of electrical double-layer capacitors. Tartu, 2020, 122 p.
198. **Ruta Hecht.** Novel Eluent Additives for LC-MS Based Bioanalytical Methods. Tartu, 2020, 202 p.
199. **Max Hecht.** Advances in the Development of a Point-of-Care Mass Spectrometer Test. Tartu, 2020, 168 p.
200. **Ida Rahu.** Bromine formation in inorganic bromide/nitrate mixtures and its application for oxidative aromatic bromination. Tartu, 2020, 116 p.
201. **Sander Ratso**. Electrocatalysis of oxygen reduction on non-precious metal catalysts. Tartu, 2020, 371 p.
202. **Astrid Darnell.** Computational design of anion receptors and evaluation of host-guest binding. Tartu, 2021, 150 p.

203. **Ove Korjus.** The development of ceramic fuel electrode for solid oxide cells. Tartu, 2021, 150 p.
204. **Merit Oss.** Ionization efficiency in electrospray ionization source and its relations to compounds' physico-chemical properties. Tartu, 2021, 124 p.
205. **Madis Lüsi**. Electroreduction of oxygen on nanostructured palladium catalysts. Tartu, 2021, 180 p.
206. **Eliise Tammekivi.** Derivatization and quantitative gas-chromatographic analysis of oils. Tartu, 2021, 122 p.
207. **Simona Selberg.** Development of Small-Molecule Regulators of Epi-transcriptomic Processes. Tartu, 2021, 122 p.
208. **Olivier Etebe Nonga.** Inhibitors and photoluminescent probes for in vitro studies on protein kinases PKA and PIM. Tartu, 2021, 189 p.
209. **Riinu Härmas.** The structure and H2 diffusion in porous carbide-derived carbon particles. Tartu, 2022, 123 p.
210. **Maarja Paalo.** Synthesis and characterization of novel carbon electrodes for high power density electrochemical capacitors. Tartu, 2022, 144 p.
211. **Jinfeng Zhao.** Electrochemical characteristics of Bi(hkl) and micro-meso-porous carbon electrodes in ionic liquid based electrolytes. Tartu, 2022, 134 p.
212. **Alar Heinsaar.** Investigation of oxygen electrode materials for high-temperature solid oxide cells in natural conditions. Tartu, 2022, 120 p.
213. **Jaana Lilloja.** Transition metal and nitrogen doped nanocarbon cathode catalysts for anion exchange membrane fuel cells. Tartu, 2022, 202 p.
214. **Maris-Johanna Tahk.** Novel fluorescence-based methods for illuminating transmembrane signal transduction by G-protein coupled receptors. Tartu, 2022, 200 p.
215. **Eerik Jõgi.** Development and Applications of E. coli Immunosensor. Tartu, 2022, 103 p.
216. **Alo Rüütel.** Design principles of synthetic molecular receptors for anion-selective electrodes. Tartu, 2022, 109 p.
217. **Tanel Sõrmus.** Development of stimuli-responsive and covalent bisubstrate inhibitors of protein kinases. Tartu, 2022, 148 p.
218. **Oleg Artemchuk.** Autotrophic nitrogen removal processes for nutrient removal from sidestream and mainstream wastewater. Tartu, 2022, 115 p.
219. **Andre Leesment.** Quantitative studies of Brønsted acidity in biphasic systems and gas-phase. Tartu, 2023, 83 p.
220. **Meeli Arujõe-Sado.** Structural effects in aza-peptide bond formation reaction. Tartu, 2023, 83 p.